Mechanics and Gas Transport of Ultrathin Membranes

by

Luda Wang

B. E. / B. S., Beihang University, Beijing, China 2006

M. S., Beihang University, Beijing, China 2009

A thesis submitted to the
Faculty of the Graduate School of the
University of Colorado in partial fulfillment
of the requirement for the degree of
Doctor of Philosophy
Department of Mechanical Engineering

2014

This Thesis entitled:

Mechanics and Gas Transport of Ultrathin Membranes

Written by Luda Wang

has been approved for the Department of Mechanical Engineering

_____

J. Scott Bunch

Committee Chairman, Dept. of Mechanical Engineering

_____

John Pellegrino

Dept. of Mechanical Engineering

*Date*_____

The final copy of this thesis has been examined by the signatories, and we

Find that both the content and the form meet acceptable presentation standards

Of scholarly work in the above mentioned discipline.

Wang, Luda (Ph. D. Department of Mechanical Engineering)

Mechanics and Gas Transport of Ultrathin Membranes

Thesis directed by Professor J. Scott Bunch

ABSTRACT

This thesis focuses on the gas transport of porous graphene membranes. Moreover, it includes the mechanical properties of ultrathin films of atomic layer deposition (ALD) Al_2O_3.

The ability to control the quantity and location of a single file molecular flux to a precise location in space has important applications to nanoscale 3D printing, catalysis, and sensor design. Barrier materials containing pores with molecular dimensions have been used to control molecular compositions in the gas phase, but unlike their aqueous counterparts, none has enabled an ability to observe or control single pore transport. Herein, we demonstrate gas transport through atomically thin, monolayer graphene opened with a single molecularly-sized, sub-nm pore demonstrating the ability to detect and control the gas flux. This is accomplished using ~nm sized gold clusters formed on the surface of the graphene. Such clusters migrate and partially block the pore. We also observe stochastic switching of small magnitude in the gas flux indicative of modulation by a single pore even without gold clusters. The stochastic switching is fit to discrete and repeatable states. These nanopore molecular valves open possibilities for unique sensors, catalytic processes, and approaches to molecular synthesis based on the controllable switching of a molecular gas flux reminiscent of ion channels in biological cell membranes and solid state nanopores.

In this thesis, a method is also presented to create and characterize mechanically robust, free standing, ultrathin, oxide films with controlled, nanometer-scale thickness using ALD on graphene. Aluminum oxide films were deposited onto suspended graphene membranes using ALD. Subsequent etching of the graphene left pure aluminum oxide films only a few atoms in thickness. A pressurized blister test was used to determine that these ultrathin films have a Young's modulus of 154 ± 13 GPa. This Young's modulus is comparable to much thicker alumina ALD films. This behavior indicates that these ultrathin two-dimensional films have excellent mechanical integrity. The films are also impermeable to standard gases suggesting they are pinhole-free. These defect-free, micron-dimensioned, 2-D ultrathin films are expected to enable new applications in fields such as thin film coatings, membranes and flexible electronics.

This dissertation is dedicated to my family and friends.

ACKNOWLEDGEMENTS

I need to thank lots of people during my Ph.D.. The most important person for my career so far is my advisor, Scott Bunch. As a kid, I already knew my passion for science and technology. But the problem was that I was still not sure whether I wanted to be an engineer or a researcher. Prof. Scott Bunch has influenced me gradually by his working philosophy. He showed his enthusiasm for science naturally, which has inspired my own love for research. To his students, Scott Bunch presents his kindness, courage, and imagination. He always gives students enough freedom, which excites my self-motivation for study. It has become gradually clear to me that I want to follow my advisor, and become a researcher focusing on scientific problems.

Secondly, I want to thank Steven Koenig and Xinghui Liu. Both of them are one year senior to me, so they helped me start with my projects. Steven is a talented researcher. After I talked with him, I can always learn something. I have really enjoyed collaborating with him. Xinghui is an expert on exfoliating graphene and other 2D materials. He would always come out with tricks which helped with exfoliation. He also did a lot of fabrication, so when I had some problems in fabrication, he is the first guy I asked help from.

Thirdly, I want to thank my lab mates, Narasimha “Nara” Boddeti, and Lauren Cantley. Nara has a strong solid mechanics background. When I was stuck with some theoretical problems, he usually knows where to find the answer. Lauren is a self-disciplined girl who can learn quickly and execute efficiently. She is always willing to help with experiments. I also have very nice time with other lab mates Peter Musso, Guillermo Acosta, Michael Tanksalvala,

Thomas Waters, Lauren Cosgriff, Phi Pham, Miguel Rodriguez, Mariah Szpunar, and Tony Xu. All of them are really nice persons.

Fourthly, I want to give special thanks to my collaborators out of the lab. Prof. Steven George knows a lot about the ALD field which helped significantly with my first project. Jon Travis has always finished the ALD coating for me on time. Andrew Cavanagh helped start the ALD project. Pinshane Huang did the cross-section TEM image in Chapter 5. For the second project, Prof. Michael Strano from MIT showed his thorough vision of the direction for the paper and has given tons of wonderful suggestions to analyze the data. Lee Drahushuk is talented at coding and theoretical work. He pushed the paper to another level. Prof. John Pellegrino has asked me some 'harsh' questions which make me think deeply on the project.

Fifthly, I want to thank some other professors in my departments. Prof. Y. C. Lee has mentored me how to balance my life and research. Prof. Todd Murray helped me with setting up the optics. Prof. Jianliang Xiao gave me suggestions on what's important for a postdoc. Prof. Xiaobo Yin is always willing to talk about research. Prof. Yifu Ding gave me confidence to compete with any researchers in the world. Prof. Wei Tan is willing to answer all kinds of questions about confusions in my life.

Sixthly, I would like to thank my friends: Hengyi Ju, Ge Qi, Feng Miao, Miao Tian, Qian Li, Xin Wang, Yunda Wang, Liang Wang, Zheng Zhang, Zhen Wang, Lewis Cox, Janet Tsai, Zhaojie Zhang, Qinghua Zhou, Tao Gong, Xiaoxi Wang, Han Luo, Fu Xiong, Min Zhan, Phil Day, Xinghua Liang, and Chenhui Zhu. Wonderful time with you guys! I also want to thank my friends in the same basketball team. Though I did not go to play with you guys for almost one year, I can still feel the pleasure of playing with you.

Last but not least, I want to thank my family. My wife, Huan Wang, is the closest person to me, and she knows me better than anybody else. Once I have some problems or difficulties, she is the right person to talk with. Her perseverance, hardworking nature, self-discipline, and humility are always the model for me. Great thanks to her to add two cute members into our family. Every time I see my kids Leo and Alina, all my unhappiness will go away. Moreover, I want to thank my parents and parents-in-law. Without your help, there is no way for me and my wife to focus on our study. You make our life much easier and more joyful.

The words and ideas only show a small part of what happened during my Ph.D.. I know, it is inevitable that I am leaving someone deserving in the ever growing list. Nonetheless, I thank all of those, who have inspired and helped me along my way to the end of the Ph.D..

Content

List of Tables

List of Figures

Chapter 1 Introduction

1.1 Introduction

Two dimensional materials were forecast to be unstable, due to the rapid drop of melting temperature of thin films.[1-5] Though people have sought two dimensional materials for decades, there was a lack of success until Geim and Noveselov first isolated graphene (purely two dimensional crystal) from graphite at 2004.[6] For graphite, there are strong covalent bonds in the plane, and weak van der Waals forces, holding these sheets together. This makes graphite easy to be shaved to form single atomic sheets of graphite or graphene. Graphene has superior properties, including electrical, mechanical, and thermal properties. Our group is more interested in the mechanical properties. Following are some of the mechanical properties, which are related to my research. James Hone's group used AFM nanoindentation to measure graphene's breaking stress of 130GPa, which is 100 times stronger than structural steel, and its Young's modulus is ~1 TPa.[7] Scott Bunch used a bulge test to detect that graphene is impermeable to standard gases.[8] This tells us that we may introduce customized nanopores into pristine graphene for separating gases/ions or DNA sequencing.

For our research, graphene with pores is an ideal membrane material for gas separation. It is atomically thin which means that flux is maximized. Its high breaking strength makes it possible to bear high pressure difference for a long time, and pristine graphene is impermeable to standard gases, which gives us the chance to create customized pores to separate our target gases. From simulation results at Oak Ridge National Lab, the selectivity for H_2/CH_4 was predicted to be extremely high for porous graphene.[9]

1.2 Outline

This thesis presents some of the first experiments on the gas separation properties of porous graphene, the gas transport through single sub-nm pores in graphene, and the mechanical properties of ultrathin Al_2O_3 ALD films. Chapter 1-3 give an overview of the basic concepts, which are related to the experimental results presented later in this thesis. Chapter 4 contains the experimental results for molecular sieving from porous graphene. Chapter 5 shows the first experimental results of testing the interaction of gas molecules with single pores in graphene. Chapter 6 is the first step to realizing gas separation from ultrathin Al_2O_3 ALD films. We studied the production methods, as well as the mechanical properties for the films to pave the way for ultrathin ALD films for gas separation.

1.3 Primary Accomplishments

By now, the research has been published in three journal articles and two conference presentations.

Selected Peer Reviewed Journal Articles:

- **L. Wang**, L. W. Drahushuk, S. P. Koenig, X. Liu, J. Pellegrino, M. S. Strano, J. S. Bunch. "Single Nanopore Molecular Valves in Graphene for Controlling Gas Phase Transport". (*Submitted*)
- S. P. Koenig, **L. Wang**, J. Pellegrino, J. S. Bunch. "Selective Molecular Sieving through Porous Graphene". ***Nature Nanotechnology***, 7, 728-732, 2012
- **L. Wang**, J. J. Travis, A. S. Cavanagh, X. Liu, S. P. Koenig, P. Y. Huang, S. M. George, J. S. Bunch. "Ultrathin Oxide Films by Atomic Layer Deposition on Graphene" ***Nano Letters***,

12(7), 3706-3710, 2012

Selected Conference Presentations:

- American Physics Society(APS), March 2014, Presentation
- Material Research Society(MRS), Fall 2012, Poster

Technical Contributions:

- Built and set up the optics for Nano-Electrical-Mechanical-Systems (NEMS) mechanical resonators drive and detection with the help of Steven Koenig and following Harold Craighead group's design. Aligned the optics and updated the components, which achieved and optimized the resonance signal. Was in charge of the resonance measurements for the lab.
- Maintained and repaired the atomic force microscope.
- Assembled several pressure chambers for bulge test measurements.

1.4 Graphene and Other Two-Dimensional Materials

A wonderful material with many advantages, graphene is a rising star in science. It is a single atomic layer of sp^2-bonded carbon atoms arranged in a close-packed honeycomb lattice. Many of graphene's unique properties can be derived from its chemical structure[10,11], which is presented in Fig. 1.1.

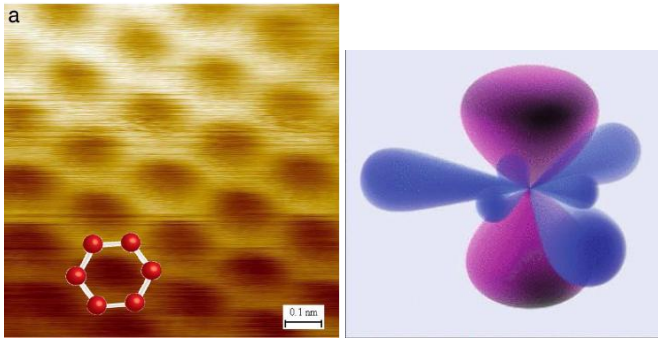

(a) (b)

Fig. 1.1 (a) STM image for graphene; (b) chemical structure for carbon atom in graphene.[10,11]

Graphene is the thinnest material in the world, and extremely robust (the Young's modulus is around 1.0 TPa[7]). As a single layer of atoms, the mass/unit surface area of graphene is quite negligible[12]. Recently, Bunch's group found that the graphene membranes have ultrastrong adhesion energy to a silicon oxide substrate. For monolayer, the energy is 0.45 J/m^2; and for two to five layers, the energy is 0.31 J/m^2.[13] In addition to its mechanical properties, graphene exhibits unique thermal properties as well.[14] Due to its high thermal conductivity and in conjunction with its mechanical strength, graphene looks to be a promising material for heat control in high density, high speed integrated electronic devices. In addition, graphene is known to have a negative coefficient of thermal expansion, meaning the material expands upon cooling.[15] One of the most well-known electrical properties of graphene is that graphene displays the quantum Hall effect (QHE). The QHE is a quantum-mechanical version of the Hall Effect, which normally requires a strong magnetic field and extremely low temperature (around 3K), observable only in very clean silicon or other semiconductor solids. In graphene, however, the QHE can be observed at room temperature, which can be attributed to the high mobility of charge carriers in graphene.[16-18] Nair measured the optical absorption of graphene.[19] It can absorb light from visible to infrared with 2.3% absorption for monolayer.[19]

There are three primary ways to make graphene. Firstly, the easiest and traditional way is mechanical exfoliation. Graphene sheets can be stacked to form graphite, however each layer is only held to another by weak van der Waals forces. Because of the strong bonding within a sheet of graphene and weak bonding between sheets, one is able to produce graphene by cleaving apart sheets of graphene from graphite using scotch tape.[6] Secondly, graphene can be created from epitaxial growth.[20,21] After heating up SiC in argon, Si will sublimate. The residue carbon atoms will assemble into graphene layers. But one drawback of SiC is the expensive price of the material. Thirdly, the most common used method growth method is chemical vapor deposition (CVD). They are two widely used catalysts, nickel[22] and copper.[23] Since the layers and qualities of graphene are hard to be controlled for nickel foil, most of the labs use copper for growth. The graphene growth on copper is a surface-catalyzed process, wherein surface decomposition of the precursor leaves carbon atoms that assemble into the 2-D graphene without carbon intercalation into the metal.[23] So the graphene growth on Cu is self-limited monolayer growth. As shown in Fig. 1.2, Ruoff's group reported graphene flakes as big as millimeters in diameter.[24]

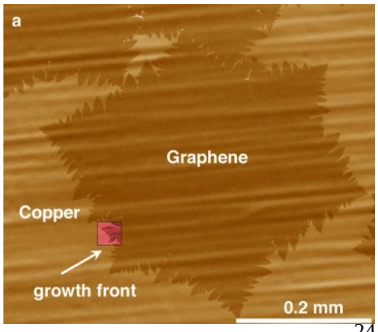

Fig. 1.2 large graphene domain.[24]

After graphene was discovered, other layered materials were also studied.[25] Transition metal oxides and transition metal dichalcogenides have layered structures,[26] which makes them major 2D materials beyond graphene for study. For the electrical properties, NbS_2, $NbSe_2$, and

$TaSe_2$ are superconductors;[26] $NiTe_2$ and VSe_2 are semi-metals,[26] WS_2, WSe_2, MoS_2, $MoSe_2$, $MoTe_2$, TaS_2, $RhTe_2$, $PdTe_2$ are semiconductors,[26] h-BN, and HfS_2 are insulators.[26] For instance, bulk MoS_2 has an indirect band gap, while the monolayer one has a direct band gap.[27,28] Decreasing the layer number N in MoS_2 leads to the gain in the indirect gap, with the direct gap almost unchanged. The indirect-direct-gap crossover is achieved with monolayer thickness.[28] Several methods can lead you to a single layer from layered materials, i.e. mechanical exfoliation,[29] laser ablation,[30] liquid phase exfoliation,[31] and synthesis by thin film techniques.[32] One application for the layered materials is atomically thin heterostructures.[25] One can stack conductive, semi-conductive, insulating materials with atomic precision, fine-tuning the performance of the resulting material.[33] One superstructure in Fig. 1.3 can be used in tunnel devices, such as field effect transistors (FETs), diodes and light emitting devices.[34]

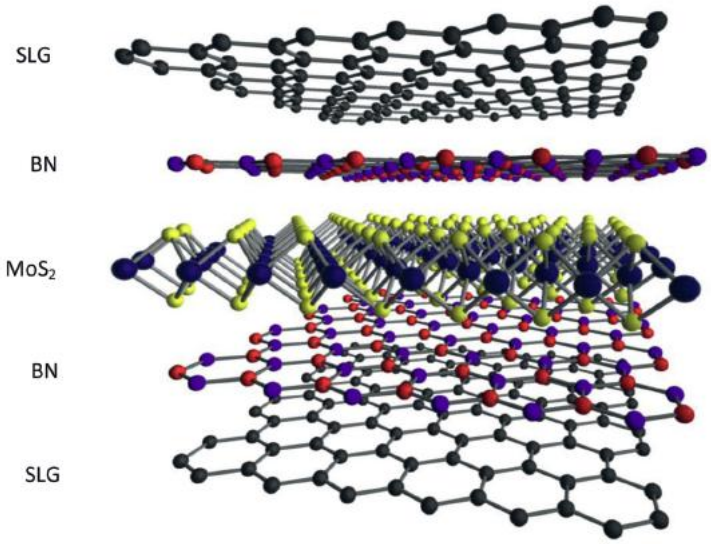

Fig. 1.3 Schematic hybrid superstructure.[34]

1.5 Nanopores

Pristine graphene is impermeable[8] to any standard gases or other molecules, which makes graphene an ideal starting material for nanopore applications. By tuning the size of nanopores, one can achieve DNA sequencing (few nanometers), ion separation (few angstroms), or gas separation (few angstroms).

To get a thorough understanding of nanopores through graphene, we may need to review the history of nanopores. DNA sequencing is one of the biggest and most important applications for nanopores since it is a label-free, amplification-free, single-molecule approach which involves low reagent volumes and low cost.[35] The mainstream method is ion-current blockade: Since the DNA is a charged molecule, the electric field across the nanopore will drive DNA through it. Once DNA goes through the pore, it will partially block the path of ions, which leads to a drop in the ionic current (as shown in Fig. 1.4).[36] In the case of a cylindrical solid-state nanopore in a high ionic strength KCl solution (>100mM), the current can be estimated as:[37]

$$i_0 \approx (\mu_K + \mu_{Cl}) n_{KCl} \cdot e \cdot \left(\frac{4l}{\pi d^2} + \frac{1}{d}\right)^{-1} V_{bias} \qquad (1\text{-}1)$$

where μ_K and μ_{Cl} are the electrophoretic mobilities, n_{KCl} is the number density of KCl, e is the quantity of electricity for one electron, d is the pore diameter, l is the pore length, which is equal to the membrane thickness.

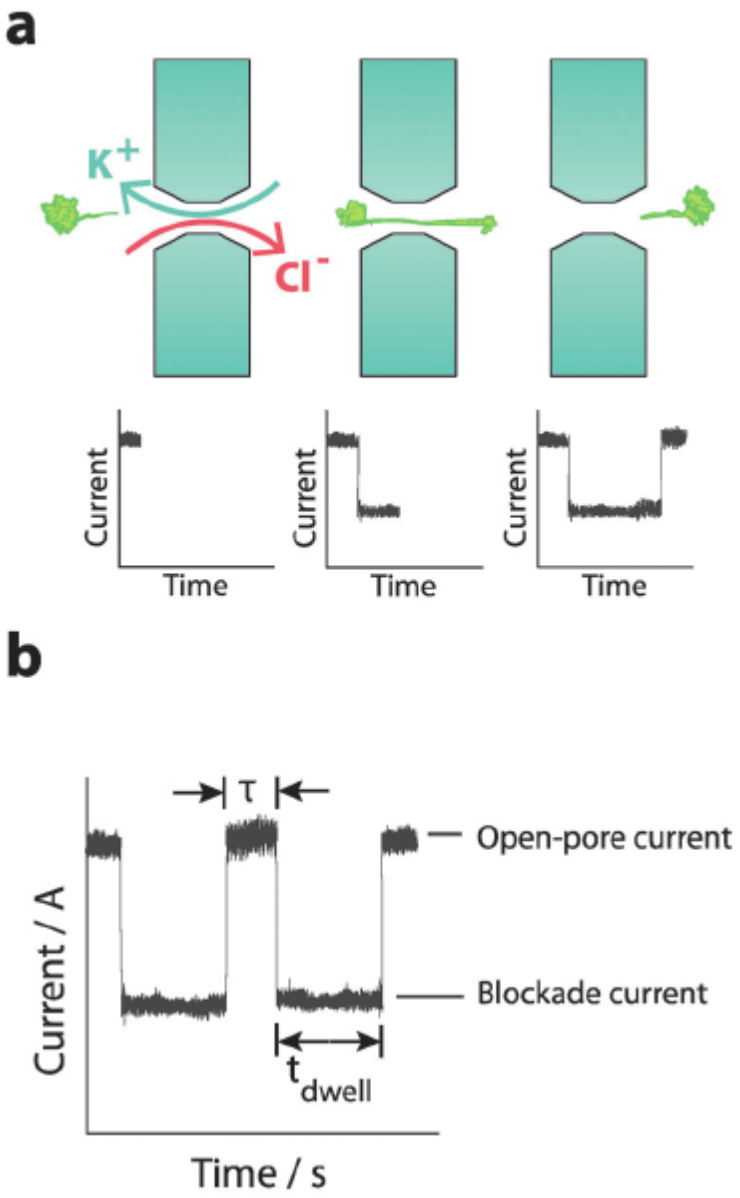

Fig. 1.4 (a) Schematic of DNA passing the nanopore, with corresponded ionic current; (b) Four parameters in translocation process: the blockade duration t_{dwell}, the time between translocation events τ, the amplitude of blockade current, the capture rate.[36]

In the 1990s, biological pore α-haemolysin was accomplished for DNA sensing/sequencing.[38] Though α-haemolysin is dominant as a biological nanopore, other more efficient biological nanopores are emerging, i. e. octameric protein channel MspA.[39] Biological pores have proved to be useful for translocation experiments, but they also have some limitations: fixed sizes, lack of stability, and are ultra-sensitive to experimental conditions (pH, temperature,

mechanical stress, and salt concentration).[35,38] Interest in solid-state nanopores has been increasing rapidly these years, due to their high stability, controllability of pore size, versatile-design ability.[35,38] The fabrication of solid-state nanopores includes thin membrane fabrication, and nanopore probing. SiN_x has traditionally been the nanopore membrane material, due to its high chemical stability and low mechanical stress.[35] From Fig. 1.5, thin SiN_x layer is deposited to both sides of bare Si. Using photolithography, followed by reactive ion etching to etch away designated pattern for the bottom SiN_x. Then the anisotropic wet etching is present to etch through the Si to form the suspended SiN_x membrane on top. The last step is poking hole on the membrane, through ion beam sculpting or other methods.[36] The nanopore probing is the key process for solid-state nanopores. Different methods can be chosen for different membrane materials, i.e. SiN, SiO_2, SiC, Al_2O_3, or graphene (Fig. 1.6).

Compared with other materials, graphene has huge advantages for nanopore applications. From the ionic current equation, we can see that the thinner the membrane, the larger the current. But the fabrication of robust, ultrathin membranes from traditional materials is a challenge. Golovchenko's group successfully made nanopores on graphene for DNA sensing.[40] As shown in Fig. 1.7, individual double-stranded DNA (dsDNA) molecules were detected using 8nm nanopores in suspended chemical vapor deposition (CVD) graphene by a focused electron beam. They found that the ionic conductance of the nanopore was proportional to the pore diameter instead of pore area.[40] This agrees with theory for an effective membrane thickness of almost zero, whose dominant resistance is the access resistance, which is inversely proportional to the pore diameter.[41]

Nanopores are widely used as biosensors. Besides the potential for DNA sensing/sequencing, nanopores have some immediate applications, including medical diagnostics, MicroRNA expression profiling, epigenetic analysis, genetic analysis, and genomic profiling.[35]

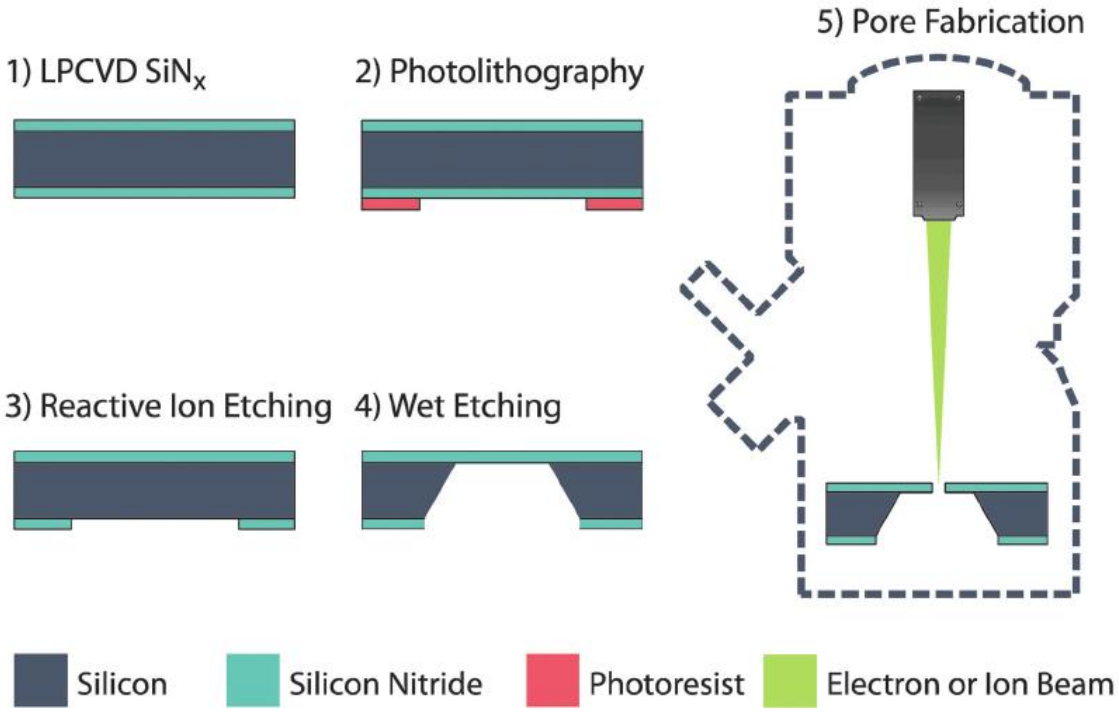

Fig. 1.5 Schematic of the fabrication for a membrane and nanopores.[36]

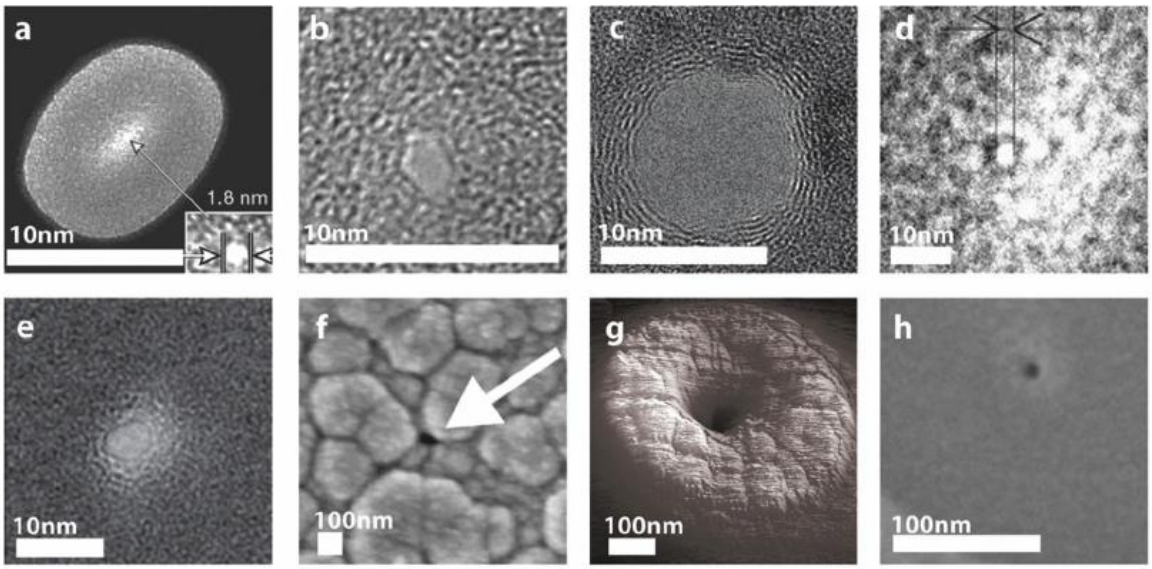

Fig. 1.6 Various images of solid-state nanopores. (a) 1.8nm nanopore in SiNx from Ar-ion beam sculption.[42] (b) 2nm nanopore in SiO2, using tightly focused electron beam followed by high-intensity wide-field TEM illumination.[43] (c) TEM image of sub-10 nm nanopore on graphene fabricated by transmission electron beam ablation lithography.[44] (d) 3 nm pore poked with a Ga focused ion beam in SiC membrane.[45] (e) 4nm nanopore fabricated from He ion microscope in a SiNx membrane.[46] (f) 18nm nanopore from electrochemically deposition with Pt.[47] (g) 30nm nanopore from local oxide deposition with ion-beam deposition.[48] (h) 2nm nanopore from local oxide deposition with electron-beam induced deposition.[49]

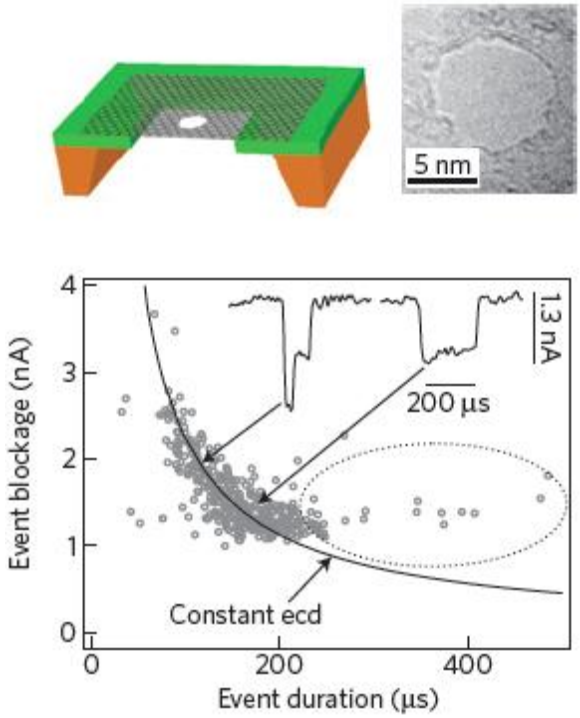

Fig. 1.7 Top left: Schematic of the nanopore on the suspended graphene film; Top right: TEM image of the 8nm nanopore; Bottom: graph of event blockage vs. event duration showing the ability to distinguish the folded DNA(inset left) and unfolded one (inset right).[40]

1.5 Gas Transport Mechanisms through Permselective Membranes

In the previous section, we introduced the concept of nanopores, especially the few nanometer diameter nanopores in graphene for DNA sensing. This chapter, we will focus on membranes, which contain pores (or free volume) for gas separation. Especially, we will highlight nanopores with few angstrom diameters on graphene, which can be used for molecular sieving/effusion gas separation. To the best to our knowledge, no group has experimentally achieved angstrom-sized nanopores for gas separation in graphene prior to our work.[50] But theoretical and simulation work previously done guided our research.

To understand gas separation it is necessary to understand the fundamentals of gas transport. Gas kinetic theory makes a bridge between the macroscopic properties and their microscopic constituents. Though the size of a gas molecule is in the angstrom range, they still obey the classical mechanical laws of matter in most situations. The kinetic theory is based on dynamics and statistics. Due to the dilute density of gases compared with liquids or solids, the gas molecules move about freely and are separated by large distance compared with their dimensions. Like classical particles, they move in straight lines until a collision occurs. After they separate, they will move off with different velocities. Velocity and position are two important parameters for the molecules' movement. Phase space is a two dimensional space which specifies the location and velocity of the particle.

The Maxwell-Boltzmann distribution is the distribution of molecular velocities under equilibrium conditions.

$$f(\vec{v}) = Ae^{-\beta v^2} \tag{1-2}$$

where $A = (\frac{\beta}{\pi})^{3/2}$, $\beta = \frac{m}{2kT}$. m, K, and T are the molecular mass, Boltzmann's constant and the temperature, respectively.

The parameter β is directly related to the average kinetic energy of molecules.

$$\langle E_{kinetic} \rangle = \frac{3m}{4\beta} \tag{1-3}$$

After putting in all the values for the parameters, the speed distribution of molecules under equilibrium conditions is (Fig. 1.8):

$$f^*(v) = 4\pi v^2 (\frac{m}{2\pi kT})^{3/2} e^{-\frac{mv^2}{2kT}} \tag{1-4}$$

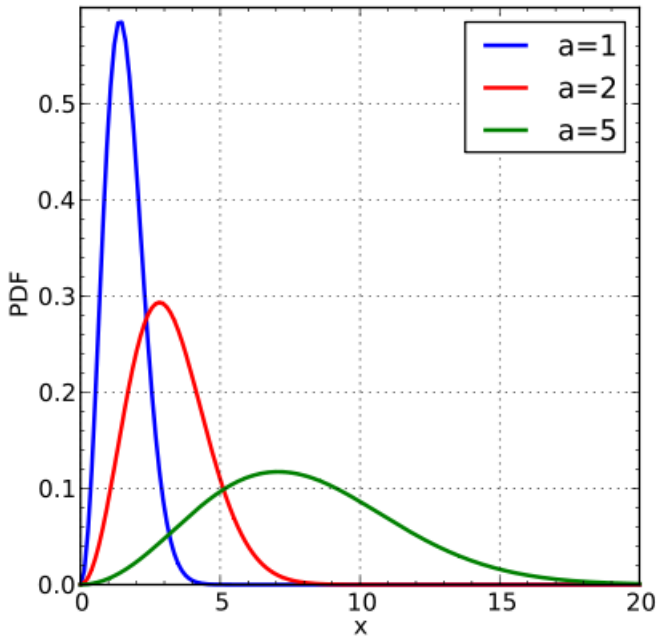

Fig. 1.8 Maxwell-Boltzmann distribution.[51]

where the scale parameter $a = \sqrt{\frac{kT}{m}}$.

The mean value of the velocity is:[52]

$$\bar{v} = \frac{1}{n}\iiint f(v) v d^3v = \frac{1}{n}\int_0^\infty f(v) v \cdot 4\pi v^2 dv = \sqrt{\frac{8kT}{\pi m}} \quad (1\text{-}5)$$

Gas molecules which strike the wall of the container is(as shown in Fig. 1.9), the flux Φ_0 is defined as the rate of flow of gas molecules per unit area:[52]

$$\Phi_0 = \int_{v_z>0} d^3v\, f(v) v \cos\theta = \pi \int_0^\infty f(v) v^3 dv = \frac{1}{4} n\bar{v} = \frac{\bar{p}}{\sqrt{2\pi m k T}} \quad (1\text{-}6)$$

where $\bar{p}$ is the pressure in the container.

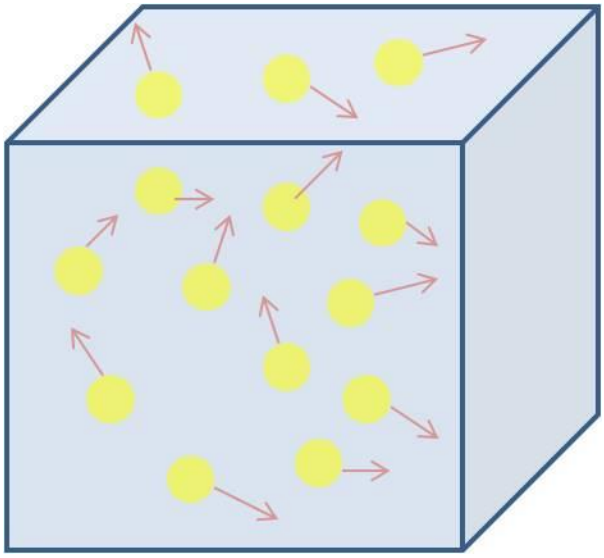

Fig. 1.9 Schematic gas molecules striking the wall of the container, which leads to the flux (the flow rate per unit area).

The mean free path is the average distance a gas molecule covers between two successive collisions. The mean free path is given by:[53]

$$d = \frac{1}{\sqrt{2} n \pi \sigma^2} \quad (1\text{-}7)$$

where n is the number of gas molecules per unit volume, σ is the diameter of the gas molecules. At room temperature, the mean free path of a gas molecule is around 100 nm.

Molecular effusion explains escape from a container through a small orifice, whose thickness is thinner than the mean free path of the gas molecules. In this case, there is no

collision of the gas molecules to the walls of the pore, and the gas molecules will either be rejected by the wall, or directly go across the pore.[53] Based on the flux of gas molecules striking the wall, the number of molecules escaping from the container is:

$$n_{escape} = \frac{A\bar{p}}{\sqrt{2\pi mkT}} = \frac{A\bar{p}}{\sqrt{2\pi M_w RT}} \tag{1-8}$$

where A is the area of the hole, M_w is the mass weight, and R is the gas constant. This is the classical effusion model, which will be used in the follow sections. To step ahead, the classical effusion describes molecules leaving box through a hole to vacuum; the number of residual molecules in the box at time t is:

$$N = N_0 e^{-\frac{A}{V}\sqrt{\frac{kT}{2\pi m}}\cdot t} \tag{1-9}$$

where N_0 is the number of molecules at t=0, A is the pore area, V is the volume of the box. The time constant is the time for the system to lose (1-1/e) of its total number of molecules, which means the decay time constant in this system is:

$$\tau = \frac{V}{A}\sqrt{\frac{2\pi m}{kT}} = \frac{V}{A}\sqrt{\frac{2\pi M_w}{RT}} \tag{1-10}$$

Based on the theory of gas transport, membranes can be used to control the rate of permeations of different species to achieve gas separation. Normally, membranes are divided into two groups: microporous membranes and dense solution-diffusion membranes (as shown in Fig. 1.10).[54]

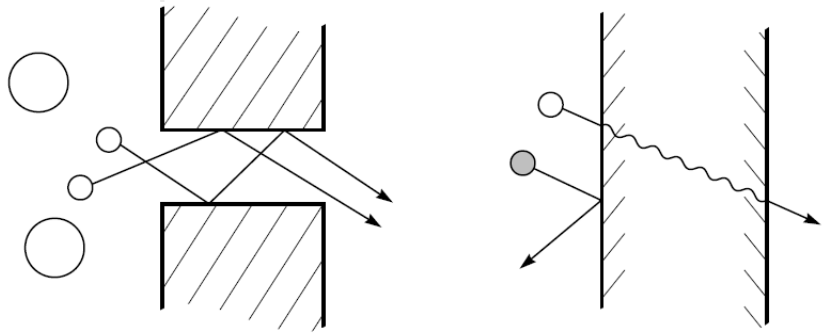

Fig. 1.10 Molecular transport through permanent porous membranes (left) or solution-diffusion membranes (right).[54]

In solution-diffusion membranes, penetrants dissolve in the membrane material and then diffuse through the membranes. Most of the polymeric gas separation membranes are included in the solution-diffusion membranes. The free-volume elements in the membranes are the tiny spaces between polymer chains. Due to the thermal fluctuation, the polymer chains open and close the space in the membrane on the same timescale as the movement of penetrants traversing the membrane. The volume flux is:[54]

$$j_i = \frac{D_i K_i \Delta p_i}{l} \tag{1-11}$$

where D_i is the penetrant's diffusion coefficient, K_i is the sorption coefficient, Δp_i is the pressure difference cross the membrane, and l is the thickness of the membrane

Then the membrane selectivity between two penetrants, i and j, can be derived as:

$$\alpha_{ij} = \frac{D_i}{D_j} \cdot \frac{K_i}{K_j} \tag{1-12}$$

As indicated from the previous equations, both diffusion and sorption will affect the flux. Diffusion is the mobility term, which will decrease as the penetrants' size increases. Sorption coefficient depends on condensibility, which usually increases as molecules size increases. As shown in Fig. 1.11, in glassy polymers, the diffusion term is dominant, so permeability falls with increasing penetrant size. On the other hand, the sorption selectivity term mainly contribute to

the permeance in rubbery polymers. As a result, permeability increases as increasing the molecule's size in rubbery polymers. In application, glassy polymers can be used to permeate air gases (i. e. nitrogen) from organic vapors, while rubbery polymers permeate the organic vapors.[55]

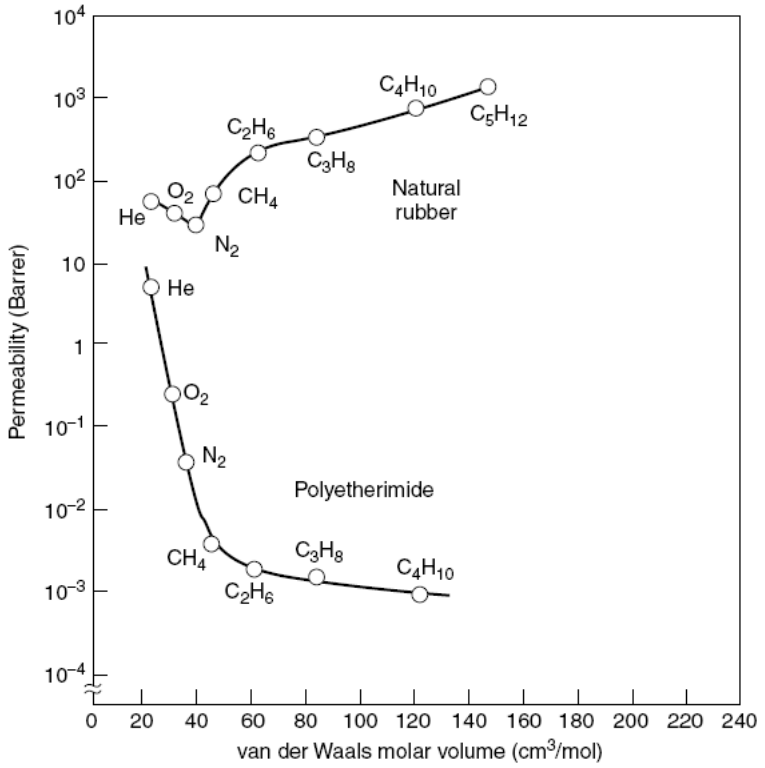

Fig. 1.11 Permeability for rubbery and glassy polymers vs. gas molecular volume.[55]

In pore-flow membranes, the penetrants are transported through tiny permanent pores by pressure-driven flow. The key parameters in porous membranes are tortuosity, porosity, and average pore diameter as shown in Fig. 1.12. Differing in pore sizes, porous membranes can follow different mechanisms (Fig. 1.13). If the pore are relatively large (>1μm), gas permeate the membrane by convective flow, wherein no separation occurs. If the pores are relatively small (similar to the mean free path of the gas molecules), the diffusion through pores follow Knudsen

diffusion. The contributions combine convective flow and Knudsen diffusion is shown in Fig. 1.14. If the pores are extremely small, molecular sieving transport dominates the permeance.

For convective (Poiseuille) flow, the permeation flux is given by:[54]

$$j = \frac{r^2 \varepsilon}{8\eta} \cdot \frac{(p_0 - p_l)(p_0 + p_l)}{\tau l R T} \tag{1-13}$$

where r is the pore radius, ε is the porosity of the membrane, τ is the tortuosity, l is the thickness of the membrane, p_0, p_l is the pressure on two sides of the membrane, η is the viscosity of the gas, R is the ideal gas constant, and T is the temperature. From the permeance equation of convective flow, we can see that there is no selectivity for different gas species.

For Knudsen diffusion, the permeation is:[54]

$$j = \frac{4r\varepsilon}{3} \cdot \left(\frac{2RT}{\pi M_w}\right)^{1/2} \cdot \frac{(p_0 - p_l)}{\tau l R T} \tag{1-14}$$

where M_w is the mass weight of the gas species. The Knudsen diffusion equation gives us indication that the gas species can be separated by the molecular mass differences.

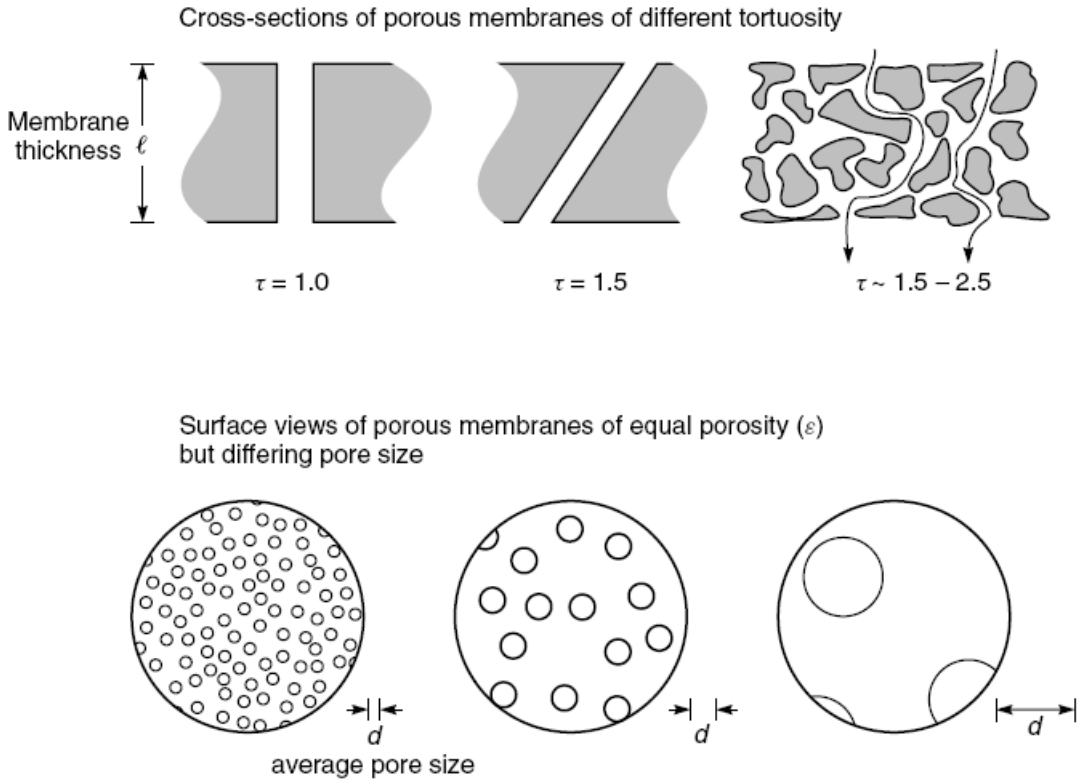

Fig. 1.12 Porous membranes' key parameters: tortuosity (τ), porosity (ε), and average pore diameter (*d*). [54]

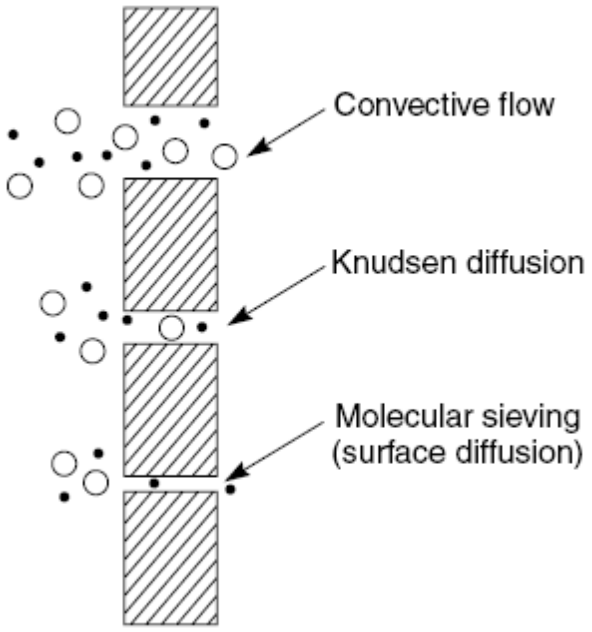

Fig. 1.13 Transport mechanisms of porous membranes.[54,56]

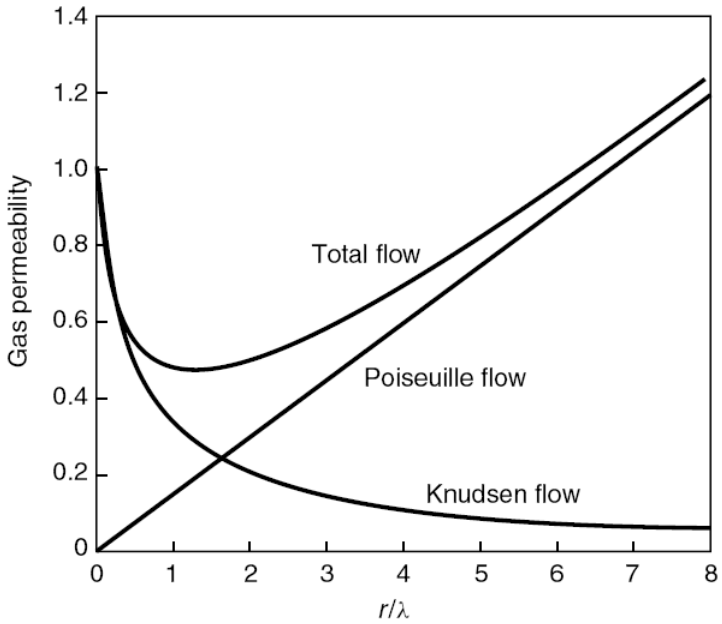

Fig. 1.14 Illustration of the contributions of Poiseuille flow and Knudsen flow as a function of r/λ.[57]

Molecular sieving for gases happens when the pore size is smaller than 1 nm. In this situation, surface adsorption and diffusion add some contributions to the permeance, which means the transport contains both diffusion in the gas phase and diffusion of adsorbed species on the surface of the pores (surface diffusion). The Knudsen diffusion and molecular sieving with/without condensable gases is shown schematically in Fig. 1.15. If the gas is condensable, significant amounts of gas can adsorb onto the pore walls. Sorbed gas molecules can move by a process of surface diffusion, which follows the Fick's law:

$$J_s = -D_s \frac{dc_s}{dx} \tag{1-15}$$

where J_s is the part of the flux from surface diffusion, c_s is the sorbed gas, and D_s is the surface diffusion coefficient.

Since the pore volume is small in molecular sieving case, the surface adsorption of condensed gas will dramatically influence the permeance of the noncondensable gas in the mixture.[58,59] As shown in Fig. 1.16, sorption of sulfur dioxide on the pore walls of the

microporous carbon membrane can restrict or even completely block the flow of hydrogen, depending on the amount of SO_2 sorbed.[60]

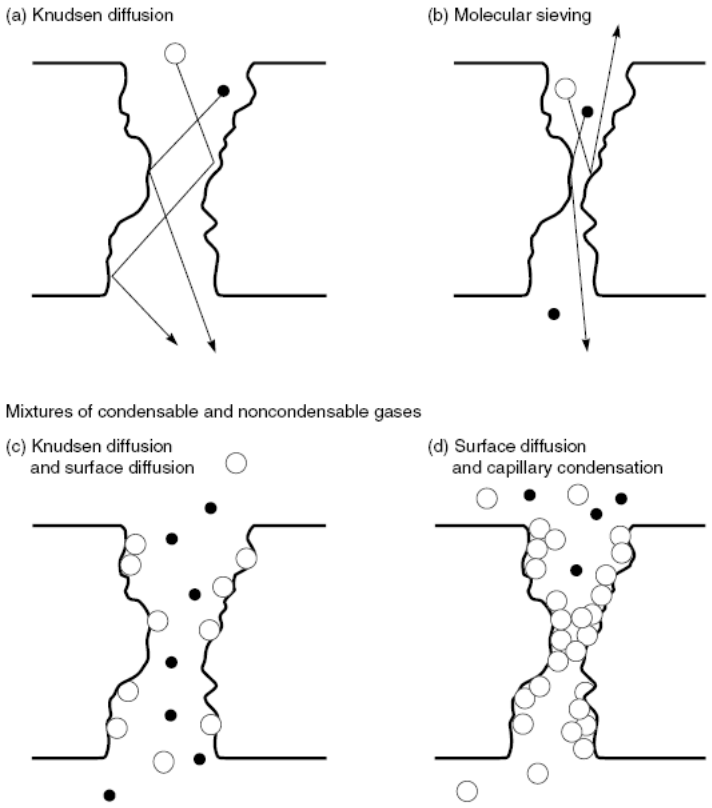

Fig. 1.15 Permeation of noncondensable and condensable gas mixtures through porous membranes with Knudsen diffusion or molecular sieving.[54]

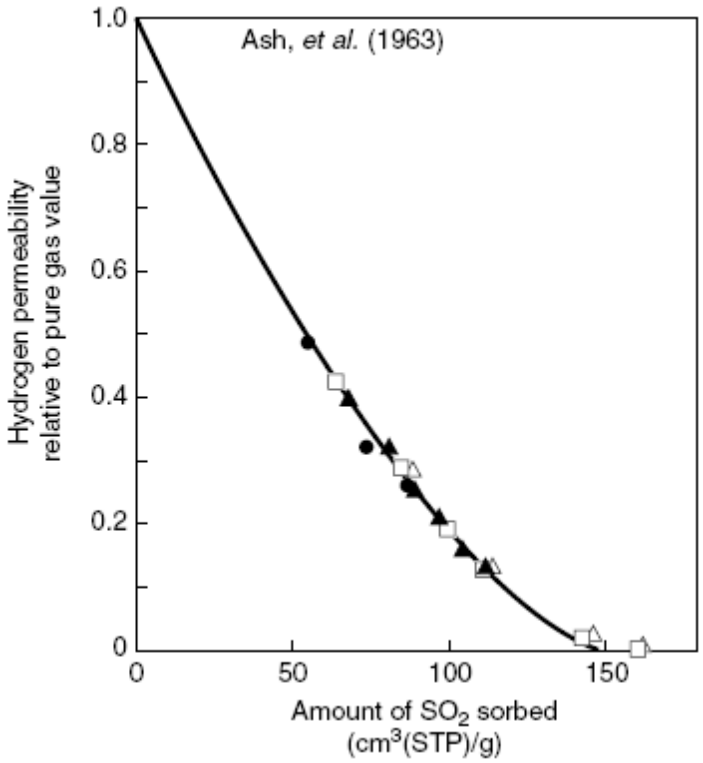

Fig. 1.16 Blocking of hydrogen (noncondensable gas) by changing the amount of SO_2 (condensable gas) with microporous membranes.[60]

The thinner the membrane, the larger the flux we can get. Using ultrathin films as the selective barrier is always a target for the development of membranes. A single layer graphene membrane is an ideal material for gas separation, due to its atomic thickness, ultra high strength, and chemically inert nature. However, the conventional analysis of diffusive transport through a membrane fails into the case of 2D atomically thin membranes.[61] Following is the gas transport mechanism for atomic thin porous graphene membranes. There are two potential pathways for gas transport through porous single layer graphene: i.) effusion pathway; ii.) adsorbed phase pathway.[61]

For the effusion pathway, the pores in graphene membranes have sub-nm diameter (Fig. 1.17). As the size of the pore is comparable to the size of gas molecules, the shape and size of gas molecules cannot be ignored. This is because as the gas molecules are slightly off the center

of the pore, the repulsive atomic force they experience will increase dramatically. And the effusion parameters are the average of the gas molecules of all the entering angles and injecting positions to the orifice. Based on the classical effusion equation, we need to make some modification:

$$\frac{dn}{dt} = \frac{\gamma \Delta p}{\sqrt{2\pi M_w RT}} \tag{1-16}$$

where γ is the transmission coefficient. The transmission coefficient is not only related to the geometric pore area A, but also depends on the transmission energy barrier E_a. In other words, $\gamma = A \cdot e^{E_a/RT}$.

At the same time, the decay time constant should modified to:

$$\tau = \frac{V}{\gamma}\sqrt{\frac{2\pi M_w}{RT}} \tag{1-17}$$

For multilayer graphene or other 2D materials, the effusion path is similar to the monolayer's situation. The pores now go through all the layers.[61]

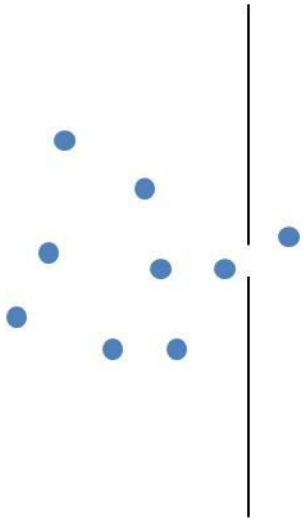

Fig. 1.17 Schematic of gas molecules effusing through porous graphene membrane.

The adsorbed phase pathway contains five steps (Fig. 1.18).[61] Firstly, a gas molecule adsorbed to a site on the surface. Secondly, the molecule diffuses to an orifice and moves into a potential well positioned in the space above the orifice. Thirdly, the molecule passes through the pore to the other side of the graphene. Fourthly, the molecule disassociates from the area of the pore onto the downstream surface of the graphene. Finally, the molecule desorbs from the surface. The whole process is schematically described in Fig. 1.18. In step 2, the molecule must both diffuse to the pore and overcome an activation barrier to position itself above the pore.[61] The permeance of adsorbed phase pathway will saturate at some pressure, which means the leak rate dn/dt vs. pressure difference Δp will not follow linear trend as Δp increases. This is one method to distinguish adsorbed path way with the gas phase pathway, which gives the linear relation between dn/dt and Δp.

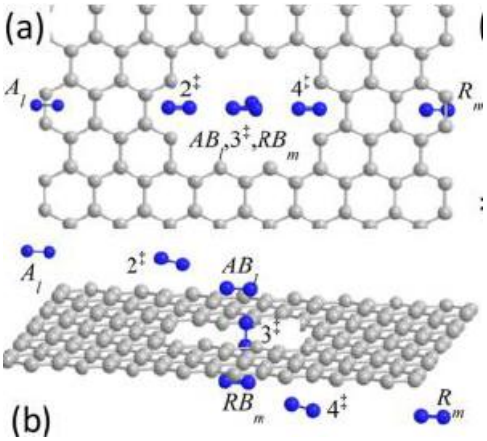

Fig. 1.18 (a) top view of nitrogen passing through a porous graphene; (b) side view.[61]

1.6 Pore Functionalization for Porous Graphene Membranes

For the transport of gas through graphene membranes, not only does the molecular mass, kinetic diameter, and molecular adsorption matter, but also the pore functionalization can play a key role.[62,63] For the calculation of gas transport, molecular dynamics (MD) simulation is the popular method. For MD simulation, each of the N molecules is treated as a point mass and Newton's equations are integrated to simulate their motion.[64] Classical MD simulations have small computational cost, which allow the simulation of large number of molecular trajectories.[63] This method is accurate enough for the gases with enough observable passing-through events within the simulation conditions and time frames. But for the gases with high barrier under limited driving force, MD simulation does not give statistically sufficient results for the passing-through events.

The free energy profile can be calculated in the simulations, and is a theoretical representation of a single energetic pathway, which is along the reaction coordinate.[65] Free energy profile gives additional information for the gases, which overcomes the kinetic resolution limitation of MD simulation.[62] A theoretical and computational study showed that a 4N4H nanopore (Fig. 1.19) with four dangling bonds saturated by hydrogen atoms and other four dangling bonds saturated by nitrogen atoms.[9] The 3.0 Å * 3.8 Å pore can distinguish five gases (H_2, CO_2, Ar, N_2, and CH_4) into two groups based on their sizes: a fast permeation rate for H_2, CO_2, and an extremely slow one for Ar, N_2 and CH_4, which agrees with the experimental results[50]. In order to study the effect of the functionalization, one can manually include or neutralize the charge to separate the functionality effect with the effect of geometrical pore size for the same pore. For example, Fig. 1.20 gives the comparison of the free energy profiles for H_2 and CO_2 between the original porous graphene and the neutralized one. And the estimated fluxes

from the kinetic theory are listed in Table 1. In neutralized case, for H_2, the free energy and the flux are similar; but for CO_2, the permeance rate decreases by 65%. This means functionalization helps increase CO_2 permeance much more than H_2. The dipolar structure of CO_2 with the nanopore's negatively charged rim N atoms is energetically favorable.[62]

In another paper, it also shows that the simulation results agree with experimental results nicely only with certain functionalization.[63] Without functionalization, the simulation results are more than an order of magnitude away from the experimental results[50]. Fig. 1.21 gives three different functionalizations: fun-1 represents hydrogen atoms added to the edge; fun-2 corresponds to a single ethyl group added; fun-3 refers to a single methyl group added to one location with hydrogen atoms added to other pore-rim carbon atoms. Fig. 1.21b shows that fun-2 fit with the experimental results well with both the flux and the selectivity.

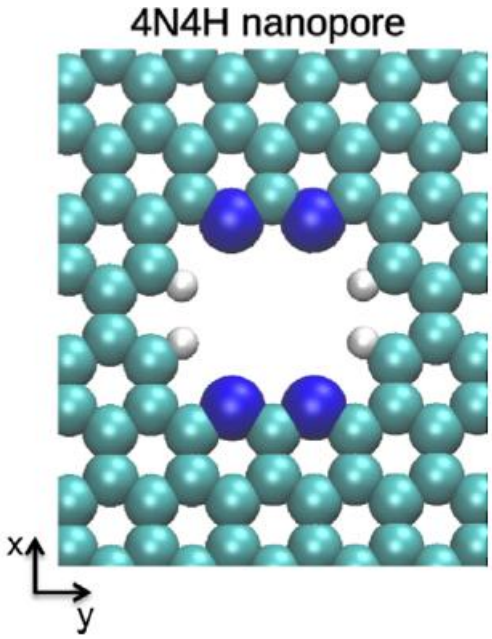

Fig. 1.19 the 4N4H pore structure(carbon, cyan; hydrogen, grey; nitrogen, blue) has dimensions of roughly 3.0*3.8Å[2.9]

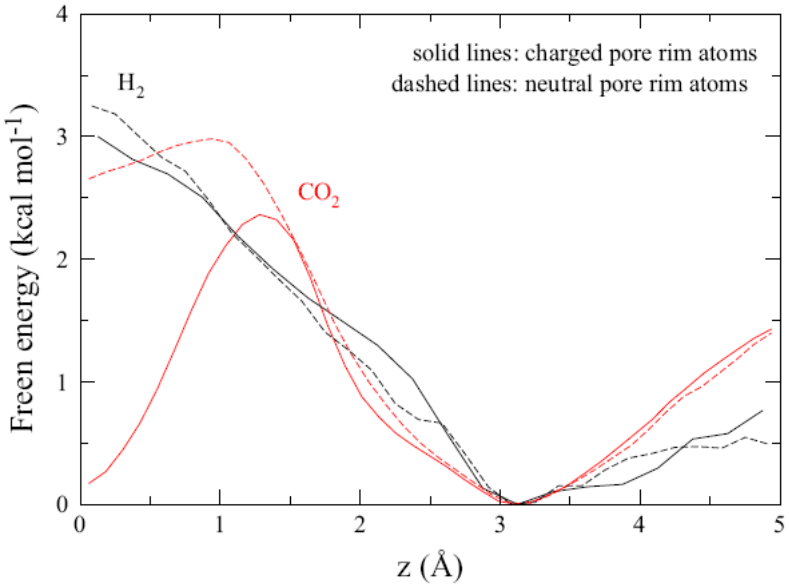

Fig. 1.20 Free energy profile of permeance for H2 and CO2 at 2atm as a function of the distance between the centers of the gas molecule and the pore.[62]

Table 1 Gas permeance barrier(ΔG) and flux in the effect of nanopore functionality.[62]

		H_2	CO_2
Charged rim atoms	ΔG (kcal/mol)	3.0	2.3
	Flux (ns^{-1})	0.18	0.11
Neutral rim atoms	ΔG (kcal/mol)	3.2	3.0
	Flux (ns^{-1})	0.13	0.038

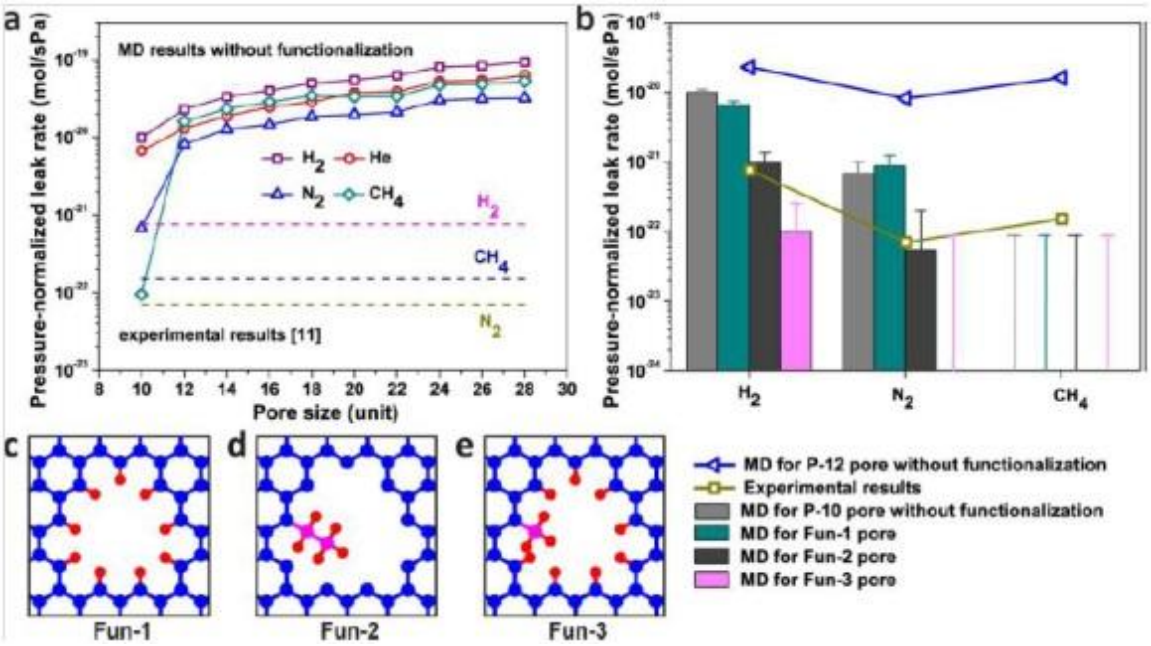

Fig. 1.21 Effects of pore functionalization and comparison with experimental results. (a) MD results for pores without functionalization with existing experimental results. (b) Comparison of MD results for selected pores with existing experimental results. (c-e) schematic of the functinalized pores. Blue spheres, red spheres, and pink spheres represent C atoms in graphene, H atoms, and C atoms in the functional groups.[63]

1.7 Graphene at the Boundary

We have poked atomic holes through graphene to study transport, the stability of those holes over time is important. Monitoring the movement of individual atoms at the edge of a graphene pore was recently achieved by transmission electron microscope (TEM). The traditional methods of obtaining atomic resolution images of surfaces are atomic force microscope (AFM) or Scanning tunneling microscopy (STM). But both of them are not suitable for observing the movement of atoms at the edge. First of all, it is hard to obtain atomic resolution images of suspended graphene membranes with AFM or STM due to the smearing of the images resulting from interactions with the imaging tips. Transmission electron microscopy is one possible technique, because it does not rely on a tip sample interaction to generate an image. The group in Berkeley used Transmission Electron Aberration-corrected Microscope

monochromated (TEAM0.5) to achieve sub-angstrom resolution with 80kV.[66] The low voltage will nearly prevent the damage of the edge from the electron beam itself. Each frame averages 1s of exposure, which is dramatically faster than the AFM/STM. They demonstrated that the dominant process in the dynamics of carbon atoms at the edge of the hole is the migration of dangling carbon atoms. For one σ bond, the energy barrier height is 0.3~0.6ev; for two or three σ bonds, the energy barrier height is 6~12eV.[66] This means the migration for a carbon atom with one bond is much easier than one with multiple bonds, which is also the reason for the stability of a zigzag edge. As shown in Fig. 1.22, in the case of armchair edge, the removal of one atom will expose the neighbor atom with one bond, while the neighbor atom still has two bonds in zigzag situation. Fig. 1.23 shows the migration and edge reconfiguration between armchair and zigzag edges.[66]

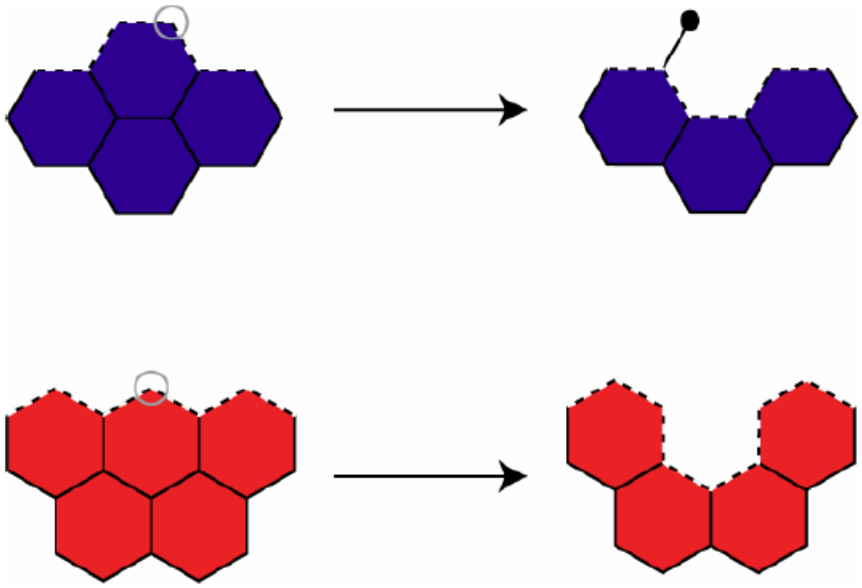

Fig. 1.22 Schematic of zigzag stability (The up is the armchair case, and the bottom is the zigzag case).[66]

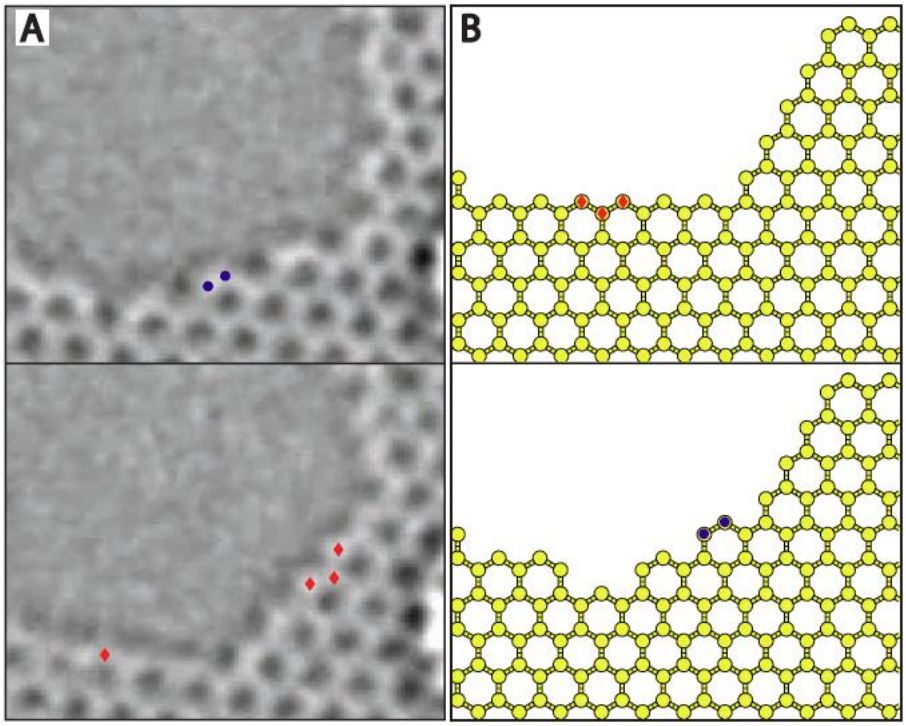

Fig. 1.23 Edge reconfiguration.[66]

1.8 Interaction of Au with Graphene

The high mobility of Au atoms/clusters on graphene surface has raised the interest for systematic study of their adsorption, migration, congregation on graphene with different thickness and substrate underneath. For single layer graphene study with scanning transmission electron microscopy (STEM), no Au atoms are retained on a residue-free, pristine graphene surface; Au atoms tend to congregate to hydrocarbon contamination.[67] The following density functional theory (DFT) study explains the high mobility.[68] The diffusion barriers for Au clusters with 1~4 atoms are 4~36 mev, which are much smaller than the adsorption energies with -0.1~-0.59 ev. They also pointed out that the diffusion of gold clusters is along the c-c bonds (T- or A-sites and B-sites, as shown in Fig. 1.24), no Au clusters would appear in the H sites (center of the hexagon).[68] The Au-Au bond is much stronger than the Au-graphene bond. So the driving force

for clustering of pre-adsorbed gold atoms is lowering the total energy of the system by forming Au-Au bonds.[68]

Fig. 1.24 Positions of foreign atoms on graphene: T site (top of carbon atom, also known as A site), H site (center of the hexagon), B site (bridge site).[67]

Compared with monolayer graphene, bilayer and trilayer graphene has stronger binding energy between Au and graphene, with the contribution of attraction from underside layers (Fig. 1.25 Table 2). With the distances from Au atom to carbon atoms (As shown in Table 2), the migration barrier can be estimate. From Table 3, all of the adatom migration barriers of the lowest energy migration are lower than k_BT at room temperature ($k_BT = 0.026\,eV$), which explains the high mobility of Au atoms on 1, 2, 3-layer graphene.[69]

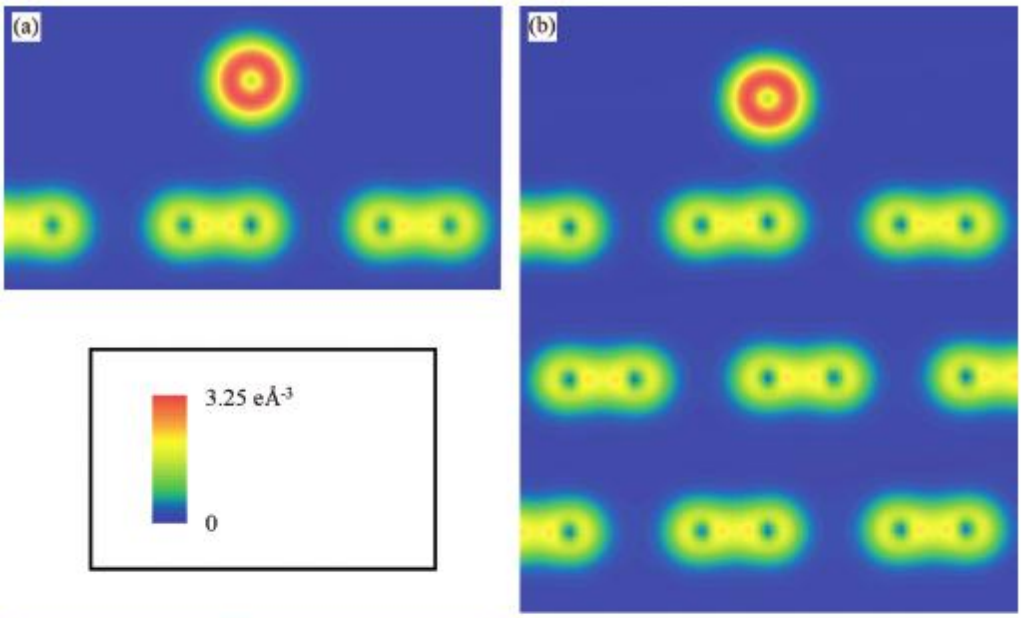

Fig. 1.25 Electron density images of monolayer and multiple layer graphene.[69]

Table 2 Adatom binding energies, Au- carbon distances by ab initio DFT study.[69]

Metal/graphene system	Site	Binding energy, E_b/eV (3 d.p.)	Distance from metal (ad)atom to nearest carbon atom(s) along bond direction(s)/Å (3 d.p.)	Distance along z axis from metal adatom to nearest carbon atom(s)/Å (3 d.p.)	Distance along z axis from metal adatom to fixed top layer carbon atoms/Å (3 d.p.)
Au					
One layer adsorption sites	A	−0.380	**3.082**	**3.082**	3.095
	B	−0.378	3.291	3.215	3.217
	H	−0.367	3.700	3.421	3.408
Two layer adsorption sites	A_1	−0.539	**3.008**	**3.008**	3.025
	A_2	−0.543	**2.661**	**2.661**	2.731
	B	−0.536	3.283	3.207	3.209
	H	−0.522	3.665	3.383	3.379
Three layer adsorption sites	A_1	−0.604	**2.729**	**2.729**	2.807
	A_2	−0.612	**2.702**	**2.702**	2.765
	B	−0.605	3.233	3.156	3.159
	H	−0.590	3.650	3.366	3.360

Table 3 Calculated migration barriers for Au on the lowest nergy migration pathways on pristine graphene by ab initio DFT.[69]

Adatom	Substrate	Path	Migration barrier ΔE/eV (3 d.p.)
Au	One layer	$A \rightarrow B \rightarrow A$	0.007
	Two layer	$A_1 \rightarrow B \rightarrow A_2$	0.008
		$A_2 \rightarrow B \rightarrow A_1$	0.024
	Three layer	$A_1 \rightarrow B \rightarrow A_2$	0.019
		$A_2 \rightarrow B \rightarrow A_1$	0.025

Substrates under the graphene will significantly slow down the Au atom diffusion on graphene. The Au adatom diffusion constant for graphene on SiO_2 is 50 times smaller than that for hexagonal boron nitride supported graphene, and 800 times smaller than that for multilayer graphite[70]. The diffusion constant is inversely proportional to the diffusion energy barrier, which means graphene on SiO_2 has the largest diffusion energy barrier. As shown in Fig. 1.26, the size of Au clusters on graphene with SiO_2 is smaller than that on graphite or h-BN substrates with the same evaporation condition, due to the strong diffusion energy barrier.[70]

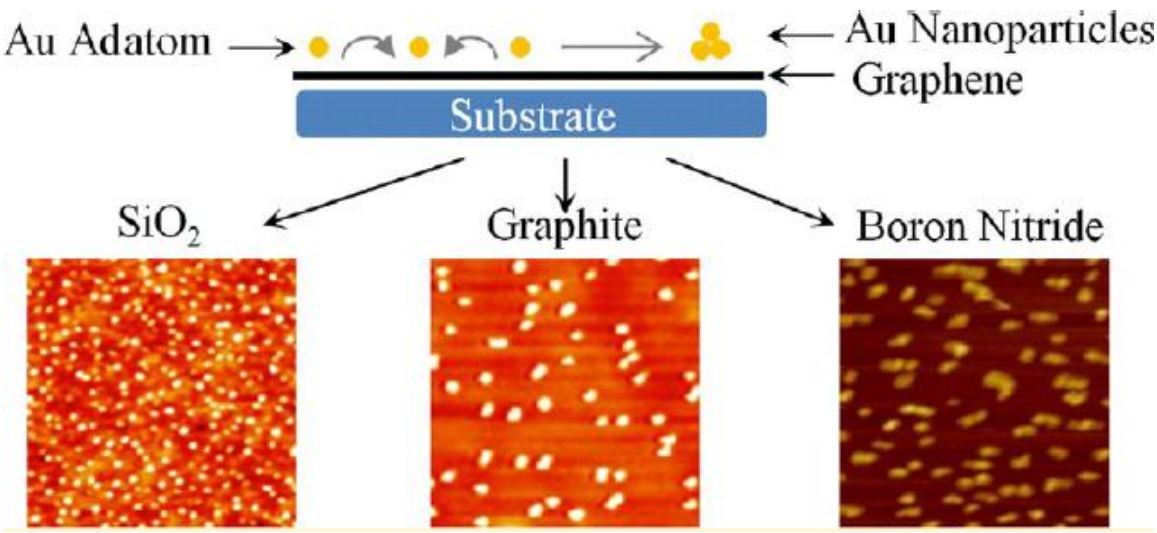

Fig. 1.26 Au clusters on graphene with different substrates SiO2(left), Graphite(middle), h-BN(right), after deposit 1Å of Au.[70]

The Au atoms may not only interact with graphene surface, but also interact with the graphene edge. The dangling bond at the edge of graphene makes a stronger binding energy between Au atom and graphene, which results in a high migration barrier for Au to diffuse along the edge. Fig. 1.27 gives that the binding energy of Au at the edge is from 3eV to 6eV, and the energy barrier for diffusion on armchair edge is one order stronger than the barrier for zigzag case.[71]

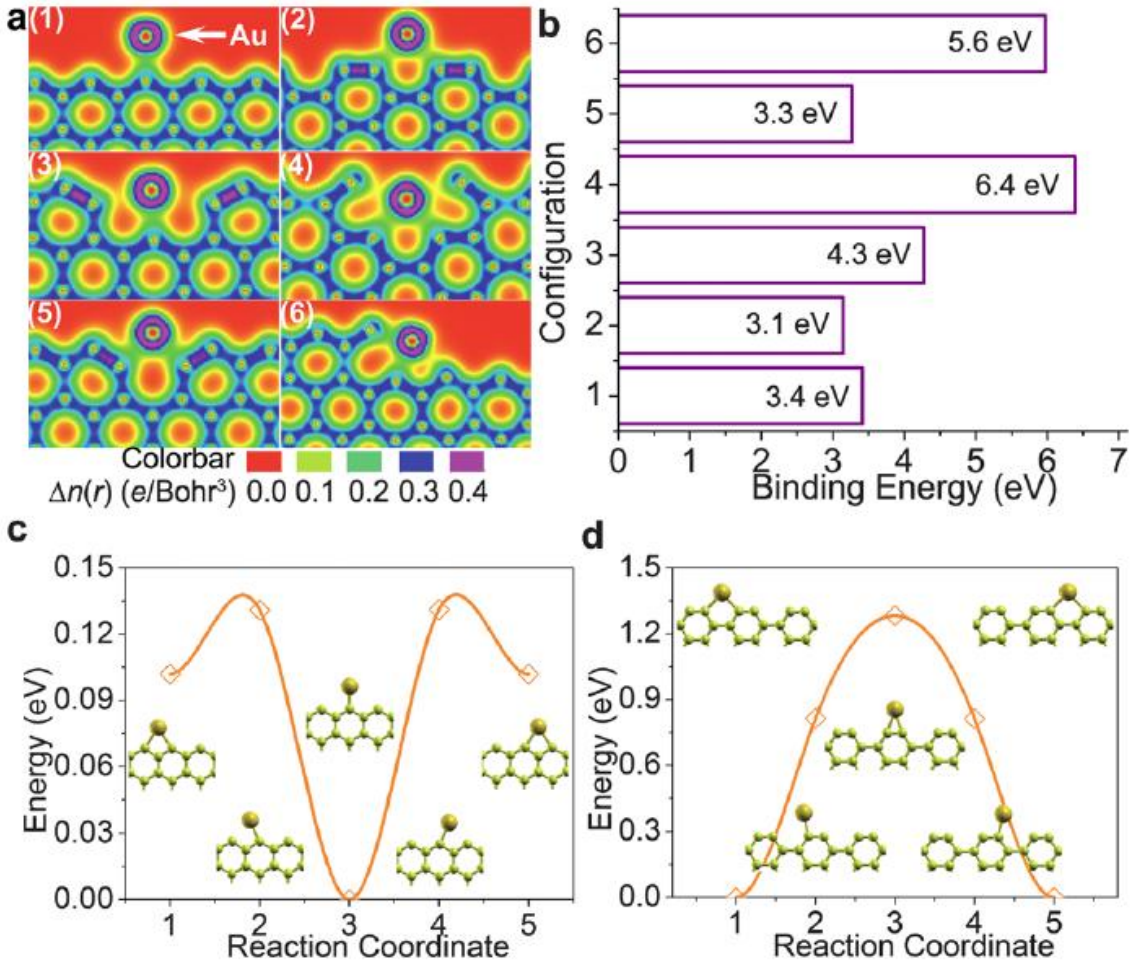

Fig. 1.27 (a) Charge density of an Au atom at different configuration edge. (b) Corresponded binding energy to (a). (c) Migration of Au at zigzag edge. (d) Migration of Au at armchair edge.[71]

1.9 Conclusions

Some fundamental concepts were introduced in this chapter to pave the way for following chapters. Graphene is well studied 2D material, and introducing nanopores in graphene has become a niche area. DNA translocation through few-nm nanopores on graphene was achieved. Few-angstrom nanopores on graphene membrane are projected to be useful in gas separations by theory and simulation. The pore functionalization may affect the permeance of the graphene membranes. Moreover, the atoms movement at the boundary (pore mouth) may affect the performance of the porous graphene membranes. In Chapter 4, we will introduce the first experimental results, using porous graphene for the gas separation. In Chapter 5, we will talk about the interaction between the gas molecules and the single pores. In the next chapter, we will focus on the mechanical properties of NEMS.

Chapter 2 Nanomechanics

2.1 Introduction

Suspended graphene devices are part of the family of nanoelectromechanical systems (NEMS). In this section, we will introduce the definition, advantages, challenges and significant applications of NEMS.[72] NEMS are made of mechanical elements and electronic circuits on the nano scale. Electro-mechanical systems contain two parts: a mechanical element and transducer. The mechanical element will change the input into the movement of the mechanical element. It can be the deflection under the applied force, the change of the amplitude of oscillation, the difference of the frequency of oscillation and so on. A transducer converts mechanical energy to electrical or optical signals. Nano-electromechanical systems are mechanical elements and electronic circuits on the nano scale (Fig. 2.1).[72]

NEMS are ultralow-power devices. The thermal fluctuation for NEMS is at the 10^{-18} W level, which means we can get signal-to-noise ratios of 10^6, if we drive a NEMS device at 10^{-12} W power.[72] And NEMS can be fabricated from silicon or other compatible materials to integrated circuit fabrication. As a result, we can fabricate the mechanical elements and auxiliary electronic components on the same chip. This can decrease the noise, and supply a possibility for more complex design.

Michael Roukes pointed out that there are three principal challenges of NEMS applications:[72] communicating signals from the nanoscale to the macroscopic world; understanding and controlling microscopic mechanics; and developing methods for reproducible and routine nanofabrication. Firstly, the signal from NEMS is pretty small, which is difficult to get. For example, the size of a beam is 1000 x 100 x 10 nm^3(L x W x t),[73] so the change of the

displacements in its thickness direction is only a fraction of a nanometer. This requires the transducers to have a far greater precision to readout the positions. Secondly, fundamental physics changes rapidly as the size scale is decreased to nanometers. Atomistic behavior will emerge.[74] Some of the phenomenon may contradict day-to-day human experience, which may require one to unlearn knowledge in order to effectively understand NEMS. Finally, it is difficult for NEMS to be fabricated. NEMS can respond to masses on the level of single atoms. This is perfect for mass sensing, but for fabrication, it can make device reproducibility troublesome.[75]

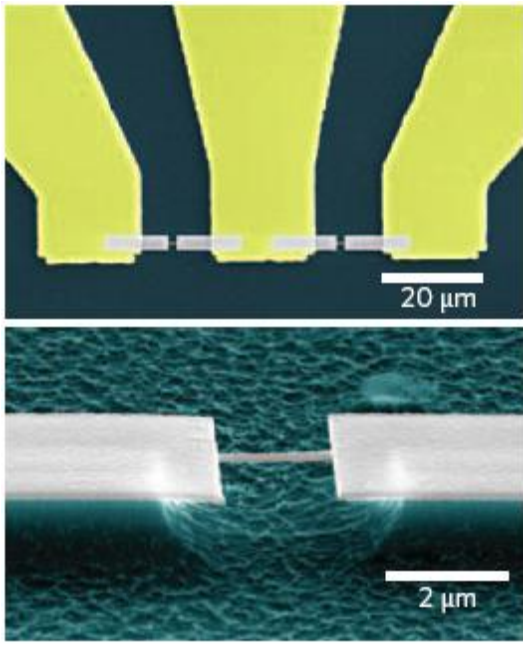

Fig. 2.1 Scanning Electron Micrographs(SEM) showing doubly clamped beam NEMS device, which is embedded in a nanofabricated UHF bridge circuit.[73]

2.2 Stress and Strain

Stress and strain are two fundamental parameters for NEMS mechanical devices. The stress vector represents the force per unit area acting on the surface. For the stress vector σ_{ij}, i is direction of normal on surface, and j is the direction of force. The stress tensor is (Fig. 2.2):

$$\sigma = \begin{bmatrix} \sigma_{11} & \sigma_{12} & \sigma_{13} \\ \sigma_{21} & \sigma_{22} & \sigma_{23} \\ \sigma_{31} & \sigma_{32} & \sigma_{33} \end{bmatrix} \tag{2-1}$$

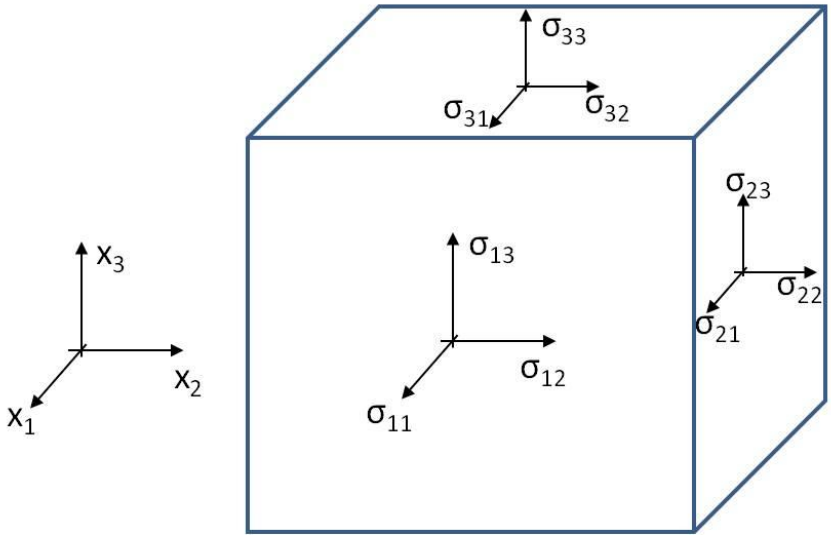

Fig. 2.2 Schematic of stress components.

The components σ_{11}, σ_{22}, σ_{33} are called normal stresses, since the direction of the stress vector is parallel to the normal of the surface. The components σ_{ij} $i \neq j$ are the shearing stresses, where the direction of the stress is perpendicular to the normal of the surface. If an external moment proportional to the volume does not exist, the symmetry condition holds:[76]

$$\sigma_{ij} = \sigma_{ji} \tag{2-2}$$

The stress can cause deformation. The relative change in shape and/or size will be defined as strain tensors. If both the original and the deformed configurations of the body are

described in the same rectangular Cartesian coordinate system (Fig. 2.3), the strain tensors can be described as a Green-Lagrange strain tensor by the material coordinate:

$$E_{ij} = \frac{1}{2}\left(\frac{\partial u_j}{\partial a_i} + \frac{\partial u_i}{\partial a_j} + \frac{\partial u_\alpha}{\partial a_i}\frac{\partial u_\alpha}{\partial a_j}\right) \tag{2-3}$$

Or be defined as Euler-Almansi's strain tensor by the spatial coordinate:

$$e_{ij} = \frac{1}{2}\left(\frac{\partial u_j}{\partial a_i} + \frac{\partial u_i}{\partial a_j} - \frac{\partial u_\alpha}{\partial a_i}\frac{\partial u_\alpha}{\partial a_j}\right) \tag{2-4}$$

For small deformation, their first derivatives are so small that the multiple terms can be negligible, which means there is little difference in the material and spatial coordinates. Then both the Green-Lagrange strain tensor and the Euler-Almansi's strain tensor reduces to Cauchy's infinitesimal strain tensor

$$e_{ij} = \frac{1}{2}\left(\frac{\partial u_j}{\partial a_i} + \frac{\partial u_i}{\partial a_j}\right) \tag{2-5}$$

According to the engineering problems, the normal strains are:

$$\epsilon_x = \frac{\partial u}{\partial x},\ \epsilon_y = \frac{\partial v}{\partial y},\ \epsilon_z = \frac{\partial \omega}{\partial z} \tag{2-6}$$

and the shear strains are:

$$r_{xy} = 2e_{xy} = \frac{\partial u}{\partial y} + \frac{\partial v}{\partial x}, r_{yz} = 2e_{yz} = \frac{\partial v}{\partial z} + \frac{\partial \omega}{\partial y},\ r_{xz} = 2e_{xz} = \frac{\partial u}{\partial z} + \frac{\partial \omega}{\partial x} \tag{2-7}$$

The normal strains give extension or shrinking, and the shear strains represent change of angle (Fig. 2.4).

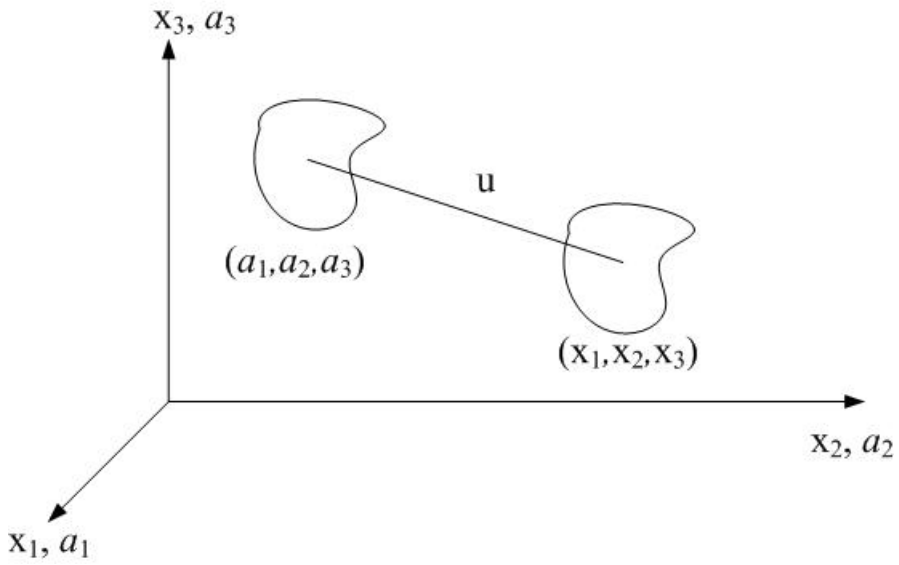

Fig. 2.3 displacement vectors.

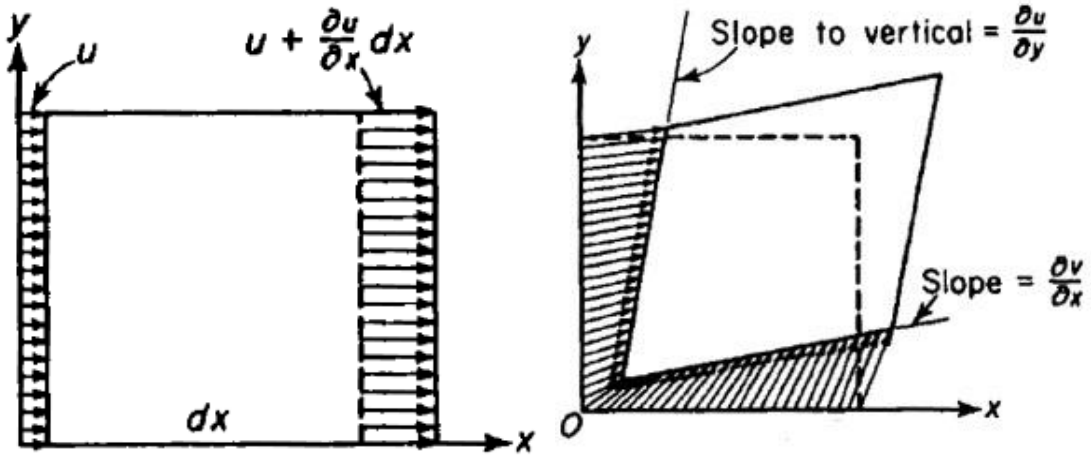

Fig. 2.4 Deformation of infinitesimal strain components.[76]

For our experiments, we focused on 2D materials. So the general forms can be simplified into 2D cases. The stress is simply:

$$\sigma_{ij} = \begin{bmatrix} \sigma_{11} & \sigma_{12} \\ \sigma_{21} & \sigma_{22} \end{bmatrix} \tag{2-8}$$

2.3 Young's Modulus and Hardness

The stresses and strains can be related by constitutive equations, which describe the macroscopic behavior due to the internal constitution of the material. Hooke's law is obeyed by the ideal elastic solid. For the uniaxial stress:

$$\sigma_{xx} = E\epsilon_{xx} \tag{2-9}$$

where E is the Young's modulus.

For the pure shear:

$$\tau_{xy} = G\gamma_{xy} \tag{2-10}$$

where G is the shear modulus, τ_{xy} is the shear stress, and γ_{xy} is the shear strain. The shear strain is the strain in the strain matrix, excluding the strain in diagonal.

For general cases, the generalized Hooke's law should be applied:

$$\sigma_{ij} = D_{ijkl}e_{kl} \tag{2-11}$$

where D_{ijkl} is the material tensor/elasticity tensor, which has 81 components. But after the symmetry of σ and e are applied, independent components reduced to 36. Moreover, $D_{ijkl} = D_{klij}$, only 21 components are needed for anisotropic elastic materials.

For isotropic materials, the generalized Hooke's law can be represent by the Young's modulus E, and the Poisson's ratio ν:

$$\begin{Bmatrix} \sigma_{11} \\ \sigma_{22} \\ \sigma_{33} \\ \sigma_{23} \\ \sigma_{31} \\ \sigma_{12} \end{Bmatrix} = \frac{E}{(1+\nu)(1-2\nu)} \begin{bmatrix} 1-\nu & \nu & \nu & 0 & 0 & 0 \\ \nu & 1-\nu & \nu & 0 & 0 & 0 \\ \nu & \nu & 1-\nu & 0 & 0 & 0 \\ 0 & 0 & 0 & \frac{1-2\nu}{2} & 0 & 0 \\ 0 & 0 & 0 & 0 & \frac{1-2\nu}{2} & 0 \\ 0 & 0 & 0 & 0 & 0 & \frac{1-2\nu}{2} \end{bmatrix} \begin{Bmatrix} e_{11} \\ e_{22} \\ e_{33} \\ 2e_{23} \\ 2e_{31} \\ 2e_{12} \end{Bmatrix} \tag{2-12}$$

$$\begin{Bmatrix} e_{11} \\ e_{22} \\ e_{33} \\ 2e_{23} \\ 2e_{31} \\ 2e_{12} \end{Bmatrix} = \frac{1}{E}\begin{bmatrix} 1 & -\nu & -\nu & & 0 & 0 & 0 & \\ -\nu & 1 & -\nu & & 0 & 0 & 0 & \\ -\nu & -\nu & 1 & & 0 & 0 & 0 & \\ 0 & 0 & 0 & 2(1+\nu) & & 0 & & 0 \\ 0 & 0 & 0 & 0 & & 2(1+\nu) & & 0 \\ 0 & 0 & 0 & 0 & & 0 & & 2(1+\nu) \end{bmatrix} \begin{Bmatrix} \sigma_{11} \\ \sigma_{22} \\ \sigma_{33} \\ \sigma_{23} \\ \sigma_{31} \\ \sigma_{12} \end{Bmatrix} \quad (2\text{-}13)$$

For the 2D ultrathin membrane cases, it is a plane stress problem ($\sigma_z, \sigma_{xz}, \sigma_{yz} \sim 0$). In this case, the constitutive equations simplify to:

$$\begin{bmatrix} \sigma_{11} \\ \sigma_{22} \\ \sigma_{12} \end{bmatrix} = \frac{E}{1-\nu^2}\begin{bmatrix} 1 & \upsilon & 0 \\ \upsilon & 1 & 0 \\ 0 & 0 & \frac{1-\nu}{2} \end{bmatrix} \begin{bmatrix} e_{11} \\ e_{22} \\ \gamma_{12} \end{bmatrix} \quad (2\text{-}14)$$

2.4 Bulge Test

Bulge test is a common way of measuring mechanical properties for the thin film structure membranes, including Young's modulus, residual stress, and yield stress from the pressure difference (as shown in Fig. 2.5).

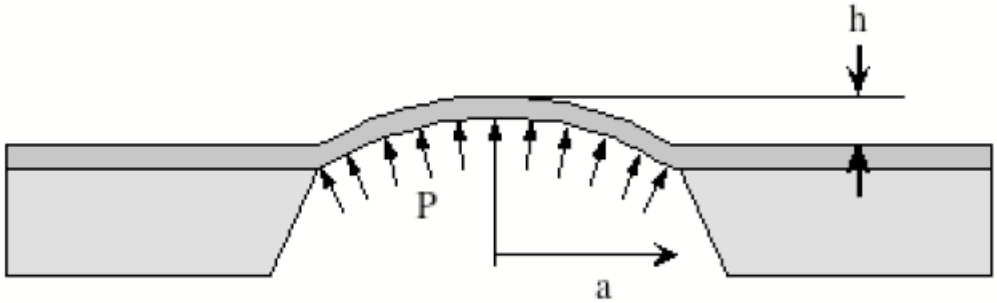

Fig. 2.5 Schematic of bulged up membrane.[77]

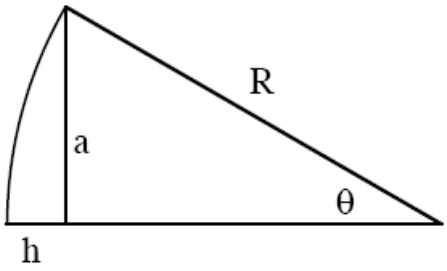

Fig. 2.6 Geometrical reference diagram.[77]

From the geometry (Fig. 2.6), we can get:

$$R^2 = (R-h)^2 + a^2 \tag{2-15}$$

where a is the radius of the flat membrane, h is the maximum height of the bulged up membrane, and R is the radius of the curvature.

After derivation, the R can be represented by h and a:

$$R = \frac{h^2+a^2}{2h} \approx \frac{a^2}{2h} \ (a \gg h) \tag{2-16}$$

From the equilibrium of force for the stress and pressure:

$$(\sigma sin\theta) \cdot 2\pi at = p\pi a^2$$

where $sin\theta = \frac{a}{R} \approx \frac{2h}{a}$, t is the thickness of the membrane

Then

$$\sigma = \frac{pa^2}{4ht} \tag{2-17}$$

From Hooke's law:

$$\sigma = E\varepsilon \tag{2-18}$$

If residual stress, σ_0, is not negligible in the membrane:

$$\sigma = E\varepsilon + \sigma_0 \tag{2-19}$$

From the definition, the film strain:

$$\varepsilon = \frac{\Delta L}{L} = \frac{\frac{2\theta}{2\pi} \cdot 2\pi R - 2a}{2a} = \frac{\theta R - a}{a} \tag{2-20}$$

where $\theta = \arcsin\left(\frac{a}{R}\right) \approx \frac{a}{R} + \frac{\left(\frac{a}{R}\right)^3}{6}$

Then $= \frac{a + \frac{a^3}{6R^2} - a}{a} = \frac{a^2}{6R^2}$, into Hooke's law with residual stress:

$$p = \frac{8h^3 Et}{3a^4} + \frac{4\sigma_0 th}{a^2} \tag{2-21}$$

When the residual stress dominates, the second term on the right of the equation is predominant, where the pressure vs. deflection curve is almost linear. As the pressure continues to increase, the first term on the right of the equation overwhelm the second term. Then the pressure vs. deflection curve follows cubic trend.[77]

The previous method is easy and simple. But deviations from this estimation may come from:

a. Bulge up not truly a spherical section;

b. $R = \frac{h^2 + a^2}{2h} \approx \frac{a^2}{2h}$ $(a \gg h)$;

c. $\theta = \arcsin\left(\frac{a}{R}\right) \approx \frac{a}{R} + \frac{\left(\frac{a}{R}\right)^3}{6}$, when $\theta \approx 0$

A more accurate method is to use Hencky's solution,[50] which is the relationship between the pressure difference and the maximum deflection for a pressurized circular clamped membrane:

$$p = \frac{K(\nu)h^3 Et}{a^4} + \frac{4\sigma_0 th}{a^2} \tag{2-22}$$

where $K(\nu)$ is related to the Poisson's ratio. From the bulk property, the Poisson's ratio for graphene and alumina are 0.16 and 0.24, respectively. For graphene $K(\nu = 0.16) = 3.09 = (1 + 16\%) * 8/3$; For alumina, $K(\nu = 0.24) = 3.35 = (1 + 26\%) * 8/3$.[78,79]

2.5 Harmonic Oscillator

A harmonic oscillator represents many physical devices, including NEMS resonators. The general equation for a damped harmonic oscillator is:

$$\frac{d^2x}{dt^2} + r\frac{dx}{dt} + \omega_0^2 x = 0 \tag{2-23}$$

where r is the coefficient related to damping and ω_0 is the natural frequency.

Depending on the value of $r^2/4$ and ω_0^2, the equation has three different solutions, represented in Fig. 2.7.

a) light damping ($\frac{\gamma^2}{4} < \omega_0^2$), $x = A_0 \exp(-\gamma t/2)\cos(\omega t)$, where $\omega = (\omega_0^2 - \frac{\gamma^2}{4})^{1/2}$;

b) critical damping ($\frac{\gamma^2}{4} = \omega_0^2$), $x = A_0 \exp\left(-\frac{\gamma t}{2}\right) + \mathrm{Bt}\exp\left(-\frac{\gamma t}{2}\right)$;

c) heavy damping ($\frac{\gamma^2}{4} > \omega_0^2$), $x = \exp\left(-\frac{\gamma t}{2}\right)[A\exp(\alpha t) + B\exp(-\alpha t)]$, where $\alpha = (\frac{\gamma^2}{4} - \omega_0^2)^{1/2}$

One key parameter to define damping is the quality factor, which is:[80]

$$Q = \frac{Energy\ stored\ in\ the\ oscillator}{Energy\ dissipated\ per\ radian} = \frac{f_0}{\Delta f} = \frac{f_0}{f_2 - f_1} \tag{2-24}$$

where f_0 is the frequency with max amplitude of the vibration, f_1 and f_2 are the frequencies at half-max amplitude, as shown in Fig. 2.8.

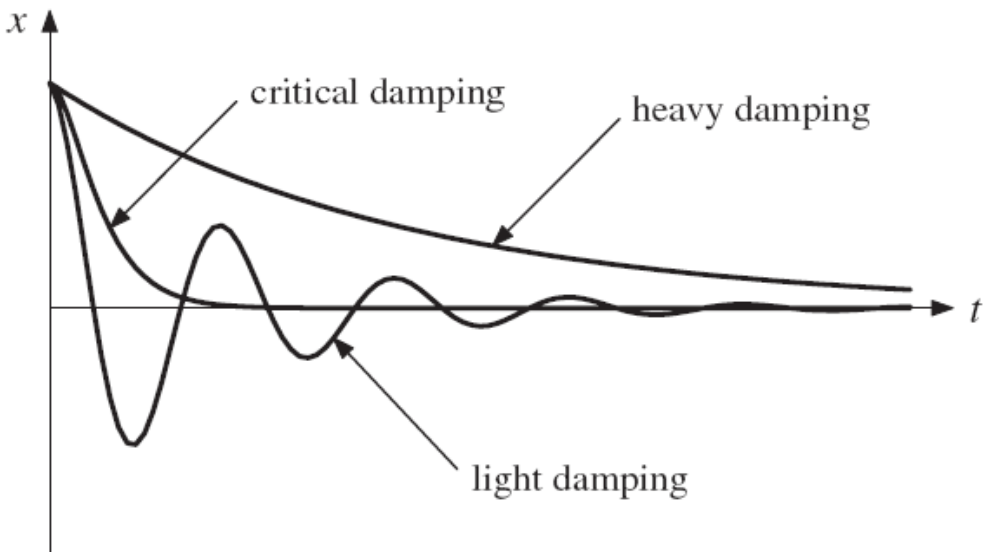

Fig. 2.7 The motion of a damped oscillator on a time scale.[80]

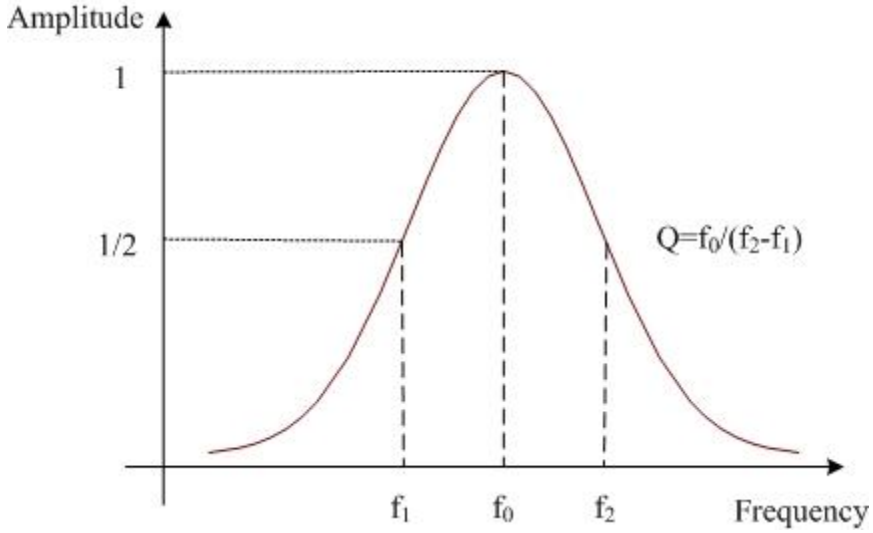

Fig. 2.8 The schematic for the definition of quality factor in spectrum.

As the damping term will extract energy from the resonance system, we need the external force to maintain the movement:

$$\frac{d^2x}{dt^2} + r\frac{dx}{dt} + \omega_0^2 x = \frac{F_0}{m}\cos(\omega t) \tag{2-25}$$

The solution for the light damping situation is: $x = A(\omega)\cos(\omega t - \delta)$, where $A(\omega) = \frac{a\omega_0^2}{[(\omega_0^2-\omega^2)^2+\omega^2\gamma^2]^{1/2}}$, $a = \frac{F_0}{m\omega_0^2}$, $\omega_0 = \sqrt{k/m}$

When $\omega = \omega_0(1 - \frac{\gamma^2}{2\omega_0^2})^{1/2}$, $A_{max} = \frac{a\omega_0/\gamma}{(1-\gamma^2/4\omega_0^2)^{1/2}} = \frac{aQ}{(1-1/(4Q^2))^{1/2}}$ [80]

For NEMS resonators, the Q is normally extremely high($Q \gg 1$).[81] Then the amplitude can be simplified as $A_{max} = \frac{aQ}{(1-1/(4Q^2))^{1/2}} \xrightarrow{Q\gg1} aQ$. Because of their small sizes, NEMS can measure extremely small displacements, weak forces and so on. Firstly, the natural frequency of the mechanical systems is:[82]

$$f_0 = \frac{1}{2\pi}\sqrt{\frac{k_{eff}}{m_{eff}}} \tag{2-26}$$

where k_{eff} is the effective spring constant and m_{eff} is the effective mass of the oscillator. This equation is a general form for 1 degree-of-freedom (1DOF) vibration problems. No matter if the resonator is beam, cantilever, or membrane; it can be modeled as a spring with a mass with/without damping. If we shrink the size of the systems as the linear dimension l, the effective mass m_{eff} is proportional to l^3, and the effective spring constant k_{eff} is proportional to l. It means the natural frequency is inversely proportional to l, so the frequency increases geometrically as the size decreases. High frequency is very important because the response time is fast, and the frequency can also increase other performances, i.e. sensitivity.[81] The small effective mass of the resonator gives NEMS a high sensitivity to additional masses. This is a valuable attribute for a wide range of sensing applications. Recently, there are a lot of papers about NEMS mass sensing. Some of them even reach atomic scale mass sensitivity.[73,75,83]

2.6 Dynamics of Membranes

In solid mechanics, a membrane is defined as a pre-tensioned two-dimensional plate, whose bending moment can be ignored. For the NEMS graphene resonator in my thesis,

membrane dynamics is a better estimation for the movement, compared with plate dynamics. For the circular membrane with field variable $\omega(r, \phi, t)$ as shown in Fig. 2.9, the motion equation in polar coordinates is:[84]

$$\mu\omega_{,tt} - T\left(\omega_{,rr} + \frac{1}{r}\omega_{,r} + \frac{1}{r^2}\omega_{,\phi\phi}\right) = 0 \tag{2-27}$$

where μ is the mass per unit area, T is the tension per unit length, $\omega_{,tt}$ is the second derivative to time t, $\omega_{,rr}$ is the second derivative to r, $\omega_{,r}$ is the first derivative to r, and $\omega_{,\phi\phi}$ is the second derivative to ϕ.

With clamped boundary condition (Fig. 2.9):

$$\omega(a, \phi, t) \equiv 0 \tag{2-28}$$

The vibration modes are shown in Fig. 2.10, with resonant frequency:[82]

$$f = \frac{\alpha_{(m,n)}}{2\pi}\sqrt{\frac{S}{\rho_A a^2}} \tag{2-29}$$

where S is the tension across the membrane, ρ_A is the mass density, a is the radius, $\alpha_{(m,n)}$ is the coefficient depending on the modes: $\alpha_{(0,1)} = 2.404$, $\alpha_{(1,1)} = 3.832$, $\alpha_{(0,2)} = 5.520$, $\alpha_{(1,2)} = 7.016$, $\alpha_{(0,3)} = 8.654$, $\alpha_{(0,1)} = 10.173$. For the graphene resonators, the fundamental mode (m=0, n=1) are the most studied modes.

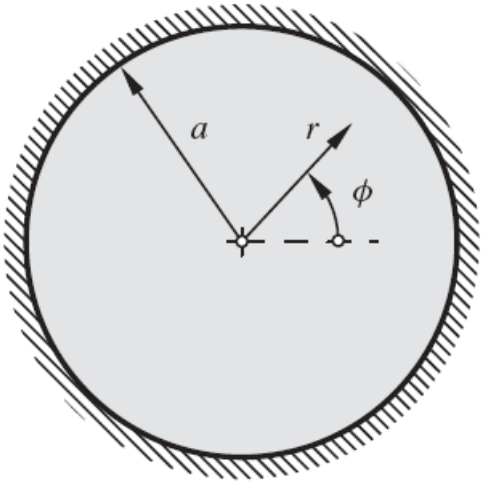

Fig. 2.9 A circular membrane clamped at the edge.[84]

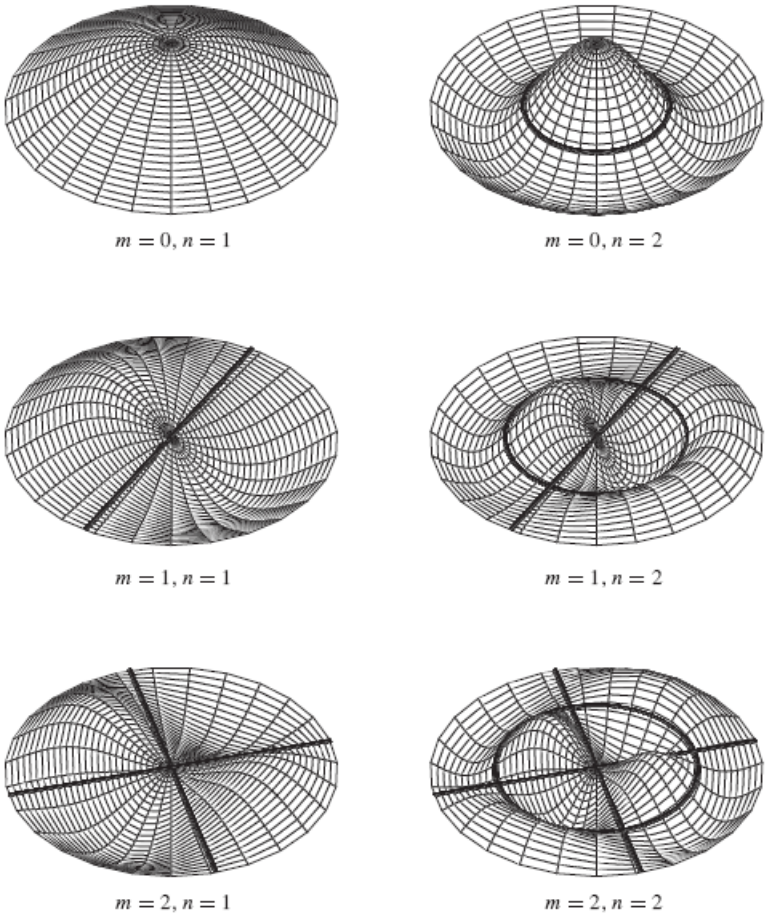

Fig. 2.10 First six mode-shapes with fixed boundary condition.[84]

For the fundamental mode of the circular membrane, the resonant frequency is:

$$f = \frac{2.404}{2\pi}\sqrt{\frac{S}{\rho_A a^2}} \tag{2-30}$$

From the Hencky's solution, we have $\Delta p = \frac{K(\nu)h^3 Et}{a^4} + \frac{4S_0 th}{a^2}$ with $S = S_0 + \frac{\Delta p a^2}{4h}$. If the contribution of the initial tension S_0 can be ignored, combining the Hencky's solution with the resonant frequency equation leads to:

$$f^3 = 7 \times 10^{-3}\sqrt{\frac{K(\nu)Et}{a^4 \rho_A^3}}\Delta p \tag{2-31}$$

where f^3 is proportional to the pressure difference Δp cross the circular membrane. This equation will be used for the ultrathin film mass density calculation in Chapter 5.

2.7 Optical Detection-Interference

Optical interference is a popular technique to detect minor movement of NEMS. For the detection of NEMS resonators, they use either Michelson interferometer for opaque and relatively wide resonators,[85] or Fabry-Perot interferometer for partially-transparent samples (i.e. graphene resonators),[86-88] as shown in Fig. 2.11. The interference signal comes from the coherence of two waves. Generally speaking, there are two kinds of coherence: temporal coherence, and spatial coherence. Temporal coherence measures the average correlation between itself and after time τ; spatial coherence gives the ability of interference between two points of the same wave over the time average.

An arbitrary optical wave $u(\vec{r}, t) = Re[U(\vec{r}, t)]$, where $U(\vec{r}, t)$ is the complex wavefunction. The average intensity:

$$I(\vec{r}, t) = < |U(\vec{r}, t)|^2 > \tag{2-32}$$

where $<\cdot>$ denotes an ensemble average.

In order to check the temporal coherence, we fix the $\vec{r}$ in $U(\vec{r},t)$. And now $U(\vec{r},t) = U(t)$. The temporal coherence function:[89]

$$G(\tau) =< U^*(t)U(t+\tau) > \tag{2-33}$$

And the normalized temporal coherence function:[89]

$$g(\tau) = \frac{G(\tau)}{G(0)} = \frac{<U^*(t)U(t+\tau)>}{<U^*(t)U(t)>} \tag{2-34}$$

where $0 \leq g(\tau) \leq 1$. $g(\tau) = 0$ means that the process "forgets" itself, so that light fluctuations at points separated by a time period longer than τ are independent. $g(\tau) = 1$ represents that the light fluctuations are exactly the same after separated by a time τ. The value of $g(\tau)$ between 0 and 1 gives partial temporal coherence. If $g(\tau)$ decreases monotonically with time delay, the value τ_c, with $g(\tau)$ decreasing to a prescribed value (i.e. 0.5, or 1/e), names the coherence time. And the light travelling in the distance $c\tau_c$ is effectively coherent, thus the definition for coherence length is:[89]

$$l_c = c\tau_c \tag{2-35}$$

where c is the speed of light, and τ_c is the coherence time.

The spectrum width of the light can be described as:[89]

$$\Delta\nu_c = \frac{1}{\tau_c} \tag{2-36}$$

For spatial coherence, we fix the t in $U(\vec{r},t)$. And now $U(\vec{r},t) = U(\vec{r})$. The normalized spatial coherence function:[89]

$$g(\vec{r}_1,\vec{r}_2) = \frac{G(\vec{r}_1,\vec{r}_2)}{\sqrt{I(\vec{r}_1)I(\vec{r}_2)}} = \frac{<U^*(\vec{r}_1,t)U(\vec{r}_2,t)>}{\sqrt{I(\vec{r}_1)I(\vec{r}_2)}} \tag{2-37}$$

Where $0 \leq g(\vec{r}_1,\vec{r}_2) \leq 1$. The explanation of spatial coherence is quite similar as temporal coherence; the only difference is the change from time period τ to distance $\vec{r}_1 - \vec{r}_2$. When $0 < g(\vec{r}_1,\vec{r}_2) < 1$, the wave has partial spatial coherence.

The more general complex degree of coherence is defined by:[89]

$$g(\vec{r}_1,\vec{r}_2)=\frac{G(\vec{r}_1,\vec{r}_2,\tau)}{\sqrt{I(\vec{r}_1)I(\vec{r}_2)}}=\frac{<U^*(\vec{r}_1,t)U(\vec{r}_2,t+\tau)>}{\sqrt{I(\vec{r}_1)I(\vec{r}_2)}} \quad (2\text{-}38)$$

A single mode CW laser is both spatially and temporally coherent. On the contrary, sunlight is neither spatially or temporally coherent. For spatial coherence, the path difference of the two waves should be much smaller than the coherent length; for temporal coherence, the time difference of two waves needs to be significant shorter than the coherent time (shown in Table 4).

The interferometers detect the intensity of the field under two waves merged:

$$I(x)=|u(\vec{r}_1,t)+u(\vec{r}_2,t)|^2$$

$$=|A_1|^2+|A_2|^2+A_1A_2^*(\hat{p}_1\cdot\hat{p}_2^*)\cos[(\vec{k}_1-\vec{k}_2)\cdot\vec{r}+(\omega_1-\omega_2)t] \quad (2\text{-}39)$$

where A_1, A_2 are the amplitude for the waves. $\vec{k}_1$, $\vec{k}_2$ are the k-vectors, ω_1, ω_2 are the frequencies of the waves, and $\hat{p}_1$, $\hat{p}_2$ represent the polarization of the waves. If the two waves share the same polarization (co-polarized waves), $\hat{p}_1\cdot\hat{p}_2^*=1$. For the waves with the same frequency $\omega_1-\omega_2=0$.

Then the equation is modified to:

$$I(x)=|A_1|^2+|A_2|^2+A_1A_2^*\cos[(\vec{k}_1-\vec{k}_2)\cdot\vec{r}] \quad (2\text{-}40)$$

Where $A_1A_2^*$ gives the the degree of interference:

$$A_1A_2^*=a_1a_2e^{i\emptyset} \quad (2\text{-}41)$$

where a_1, a_2 are the amplitude of wave1 and wave2; $\emptyset$ is the phase difference between two waves. For the design of the interferometer, we want to maximize $A_1A_2^*$. If $a_1$and a_2 are given, $\emptyset$ is the only parameter to be optimized. Typically, we want the design to reach $\emptyset=2n\pi$, avoid $\emptyset=(2n+1)\pi$.

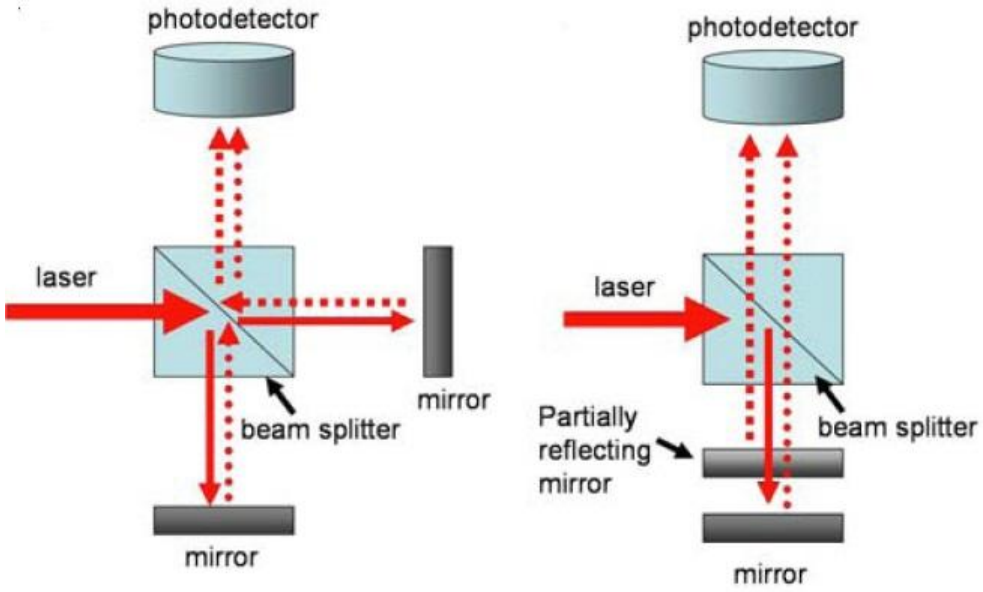

Fig. 2.11 Schematic of Michelson interferometer (left) and Fabry-Perot interferometer (right).[90]

Table 4 Spectral width, coherence times, and coherence length for different light sources.[89]

Source	$\Delta\nu_c$ (Hz)	$T_c = 1/\Delta\nu_c$	lc=c T_c
Filtered sunlight (λ_0=0.4~0.8μm)	$3.75*10^{14}$	2.67 fs	800nm
Light-emitting diode (λ_0=1μm, $\Delta\lambda_0$=50nm)	$1.5*10^{13}$	67 fs	20 μm
Low-pressure sodium lamp	$5*10^{11}$	2 ps	600 μm
Multimode He-Ne laser (λ_0=633nm)	$1.5*10^{9}$	0.67 ns	20 cm
Single-mode He-Ne laser (λ_0=633nm)	$1*10^{6}$	1 μs	300 m

We use the Fabry-Perot interference to measure the graphene membrane resonators. From Fig. 2.12, the blue laser (405nm) is the drive laser, and the red laser(633nm) is the detection laser. The blue laser is modulated by the intensity modulator, goes through the optical path, and reaches the sample. It could change the temperature on or near the membrane, which causes a periodic force. With this force, the resonator can be vibrated. The movement of the resonator is

detected by the red laser by Fabry-Perot interference, and then the reflected signal will be collected by the photo detector. Finally, we can use the network analyzer to analyze the signal.

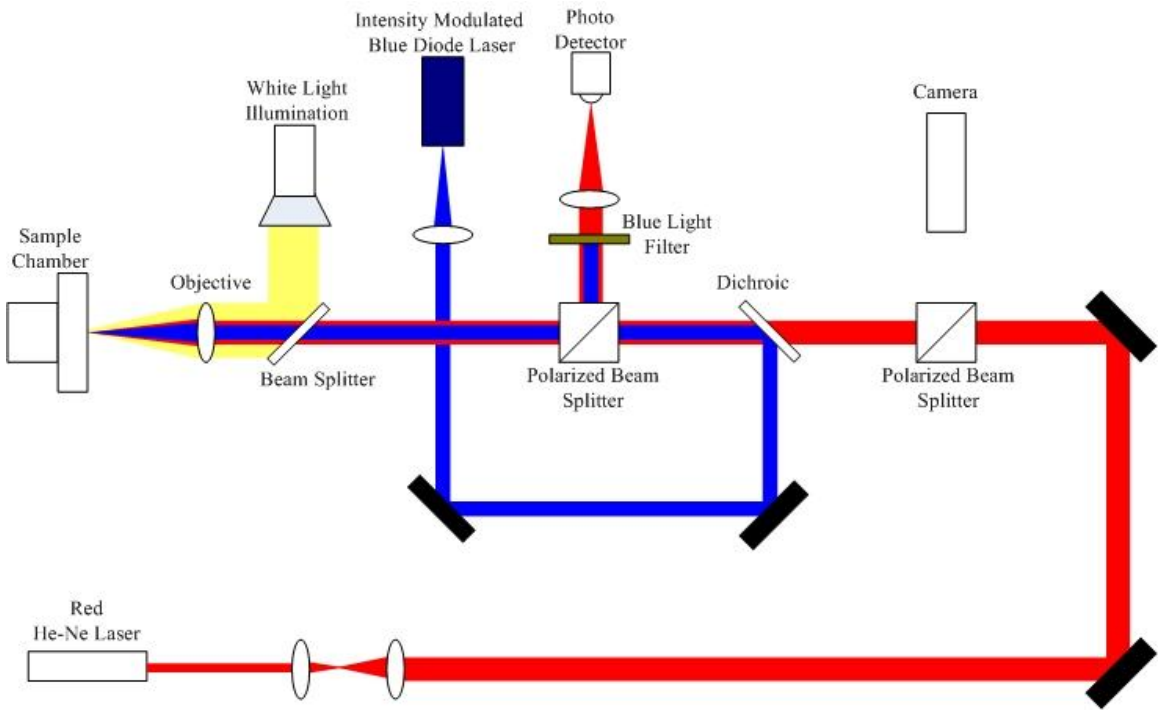

(a)

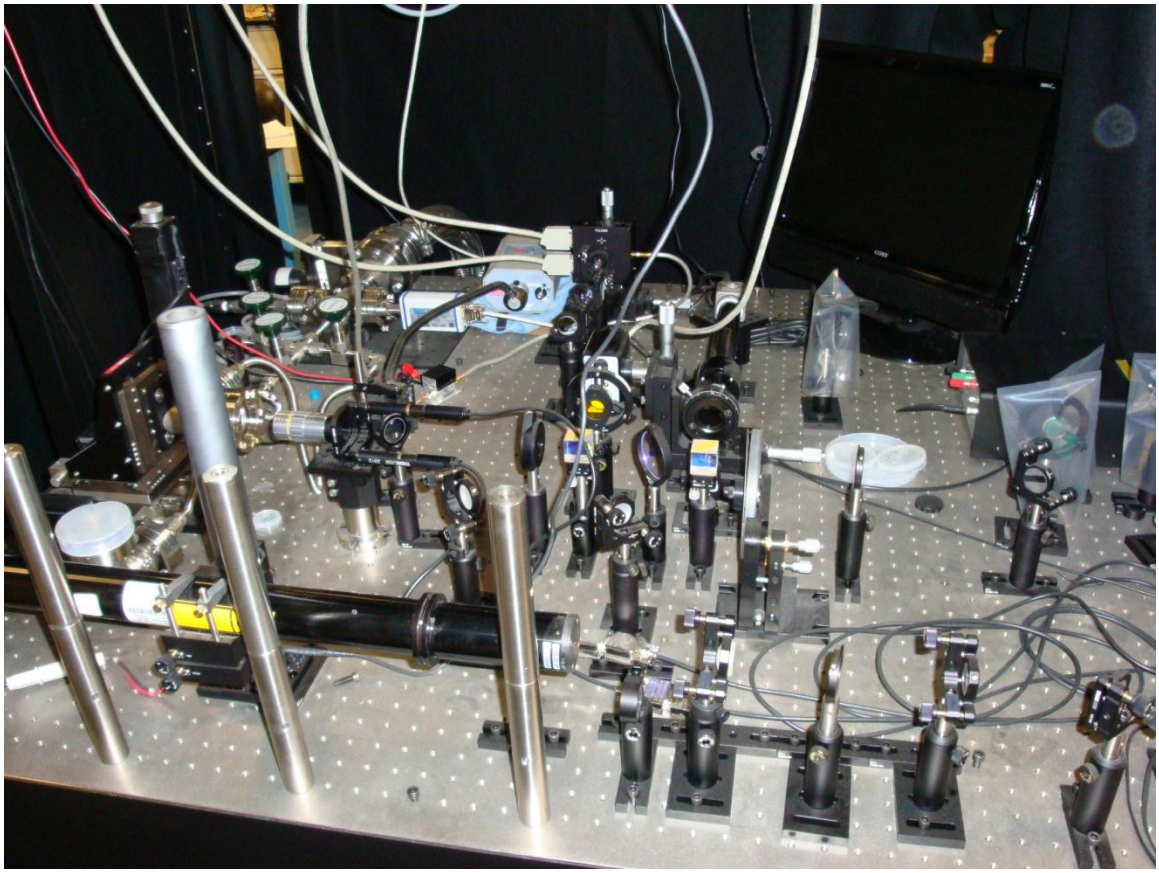

(b)

Fig. 2.12 (a) Schematic of the system set up; (b)Tested system.[91]

The fast leak rate of the porous graphene membrane was measured from the changes in the resonant frequency of the membrane versus time.[50] A pressure difference was induced across the membrane, which would increase the resonant frequency by introducing tension. If the gas molecules can go through the porous graphene membrane, the pressure difference would decrease to zero gradually, which would make the resonant frequency drop to the initial value quickly. But if the molecules could not go through the membrane, the pressure difference would persist for a while, which would provide a constant resonant frequency. An example of measurements taken for this thesis is shown in Fig. 2.13.

In this case, an etched porous graphene was placed in vacuum chamber of 0.1torr for several days to ensure the microcavity is at equilibrium with the pressure of the vacuum chamber.

A pure gas species was then introduced into the same vacuum chamber at a given pressure and the resonant frequency was measured continuously. The resonant frequency decreases with time (as the pressure in the microcavity goes from vacuum to the external pressure), and from the rate of decrease, the leak rate through the membrane can be derived. From Fig. 2.13, the leak rate for H_2, N_2, CO_2, CH_4 were several seconds; but no significant change of the frequency for SF_6 for several minutes. This membrane will be referred to as 'Bi-4.9Å', as it is a bilayer membrane with sieving kinetic diameter of SF_6(4.9Å).

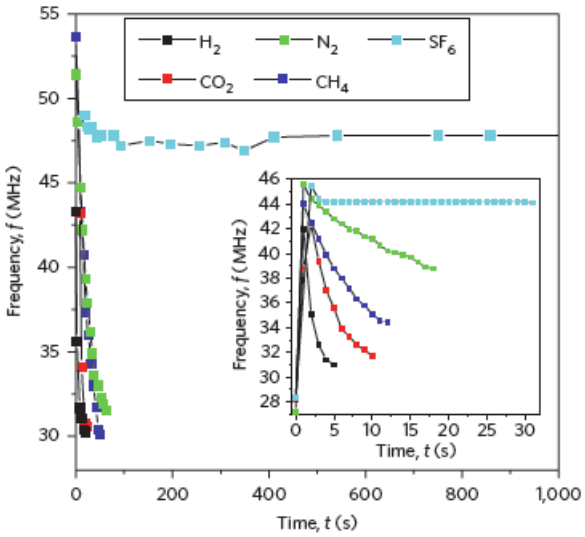

Fig. 2.13 Frequency versus time for various gases with a pressure of 100 torr introduced into the vacuum chamber. Inset: data from the same device with 80torr pressure.[50]

We can also determine the equation for *dn/dt* from *df/dt*:[50]

$$\frac{dn}{dt} =$$

$$\frac{V}{RT}\left[\frac{1}{2}\left(\frac{8743{S_0}^2\rho_A - 47785{S_0}^2\rho_A{}^2a^2f^2 + 81589\rho_A{}^3a^4f^4}{K(\nu)Ew}\right)^{1/2} + \right.$$

$$\left.\frac{81589\rho_A{}^3a^4f^4 - 23892S_0\rho_A{}^2a^2f^2}{K(\nu)Ew\left(\frac{8744{S_0}^2\rho_A - 47785{S_0}^2\rho_A{}^2a^2f^2 + 81589\rho_A{}^3a^4f^4}{K(\nu)Ew}\right)^{1/2}}\right]\frac{df}{dt} \qquad (2\text{-}42)$$

where S_0 is the initial tension of the membrane, ρ_A is the mass density, E is the elastic constant, $K(\nu)$ is the constant from Hencky's solution, w is the thickness of the membrane, a is the radius of the membrane, f is the resonance frequency, V is the volume of the microcavity, treated as a constant in our case, R is the gas constant, T is the temperature, and $\frac{df}{dt}$ is the change of the frequency.

From the leak rates of all the membranes, we can get the selectivity for the membranes (Table 5).

Table 5 Ideal gas separation factors for membrane 'Bi-4.9Å'.[50]

	H_2	CO_2	N_2	CH_4	SF_6
H_2	--	3	11	5	N/A
CO_2	--	--	3.6	1.7	N/A
N_2	--	--	--	0.5	N/A
CH_4	--	--	--	--	N/A
SF_6	--	--	--	--	--

2.8 Conclusions

This chapter introduced the basis of solid state mechanics and dynamics for NEMS, especially for graphene NEMS resonators. Optical detection for graphene resonators was introduced. In next chapter, we will review ALD, the material involved in one of the projects.

Chapter 3 Atomic Layer Deposition (ALD)

3.1 Introduction

ALD becomes a key technique for science and technology progress, which can be used to achieve ultrathin films in our lab. ALD reaction is continuous and almost pin hole free, even for the high aspect ratio.[92] Many of the ALD materials are stable, which can be used in hash environments. What's more, there are numerous applications for flexible ultrathin insulating or oxide films, which may come from ALD.

3.2 Atomic Layer Deposition

Atomic layer deposition (ALD) becomes an important surface technology with motivation towards scaling down microelectronic devices. Semiconductor processing is the main driver for ALD, since ALD meets the needs of continuous and pinhole-free films of semiconductor devices. Other applications come from magnetic read/write heads[93] and diffusion barrier coating.[94] Most ALD processes are based on binary reaction sequences, as shown in Fig. 3.1. Some materials have been grown by ALD, shown in Fig. 3.2.

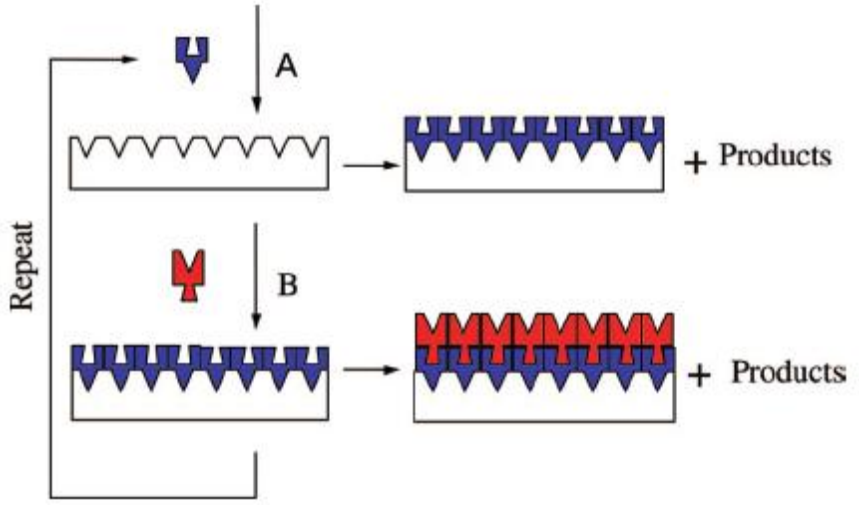

Fig. 3.1 Schematic of ALD using self-limiting surface chemistry and an AB binary reaction sequence.[95]

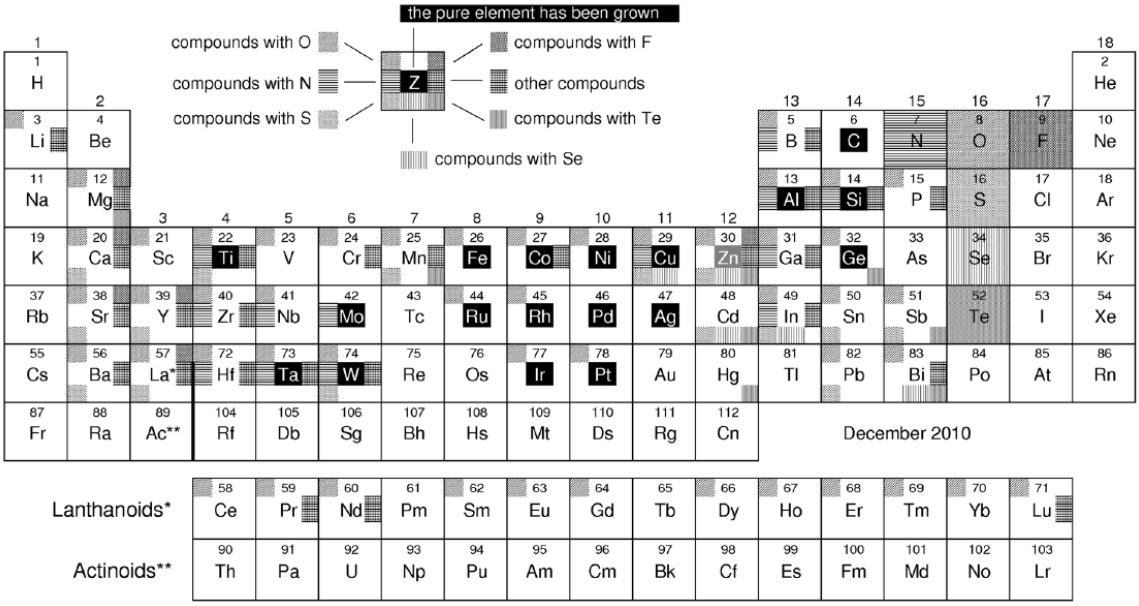

Fig. 3.2 The materials grown by ALD.[96]

The reactants in ALD should be thermally unstable, which is easy to react without crucial condition, i. e. inorganic or metalorganic. Alkyls are ideal candidates for ALD reactants, since they are very reactive. Another necessary property for surface ALD reactions is self-termination, which requires surface adsorption to be irreversible. Physisorption is always reversible, while

chemisorptions can be reversible or irreversible. So the adsorption in ALD is limited to irreversible chemisorptions. The adsorption rate is defined by:

$$\frac{dQ}{dt} = r_a - r_d = k_a p(1 - Q) - k_d Q \tag{3-1}$$

where r_a is the adsorption rate, r_d is desorption rate, k_a is the adsorption rate constant, k_d is the desorption rate constant, p is partial pressure, and Q is the chemisorption coverage. After saturation the adsorption rate is zero, Langmuir isotherm gives the chemisorption coverage in equilibrium:

$$Q_{eq} = \frac{k_a p}{k_a p + k_d} = \frac{1}{1 + (kp)^{-1}} \tag{3-2}$$

For irreversible adsorption, the equilibrium constant $k \to \infty$, then $Q_{eq} \to 1$. So the chemisorption coverage becomes:

$$Q = Q_{eq}\left(1 - e^{-(k_a p + k_d)t}\right) = 1 - e^{-k_a p t} \tag{3-3}$$

The chemisorption mechanisms in ALD have three different kinds: a. ligand exchange, b. dissociation, c. association, which is shown in Fig. 3.3. In ligand exchange, the ligand is combined with a surface group and released as a gaseous reaction. For dissociation, the reactant molecule is separated onto reactive sites on the surface. According to association, the reactant forms a coordinative bond with a reactive site, and no ligand is released.[97]

The reason for the self-limiting (self-termination) is a finite number of surface sites can only deposit a certain number of surface species. The factors causing saturation are steric hindrance, and the number of reactive surface sites. In some situations, even though space remains available on the surface, no bonding sites are accessible. The reaction continues until steric hindrance stops it, which causes growth of less than a monolayer per cycle.[98] Temperature

can also affect the growth per cycle (GPC) by affecting the number and type of reactive sites on the surface, and through changing the preferred reaction mechanisms. What's more, another issue to impact GPC is the number of cycles. From the very beginning, ALD reaction cycle happens on the surface of the original substrate material. Then, it occurs on a surface with both the original substrate and the ALD-grown material. Finally, it reacts on a surface with only the ALD grown material exposed. Different steps will give you different GPC. Generally speaking, the growth mode has three types (as shown in Fig. 3.4): a. two dimensional growth, b. island growth, and c. random deposition.

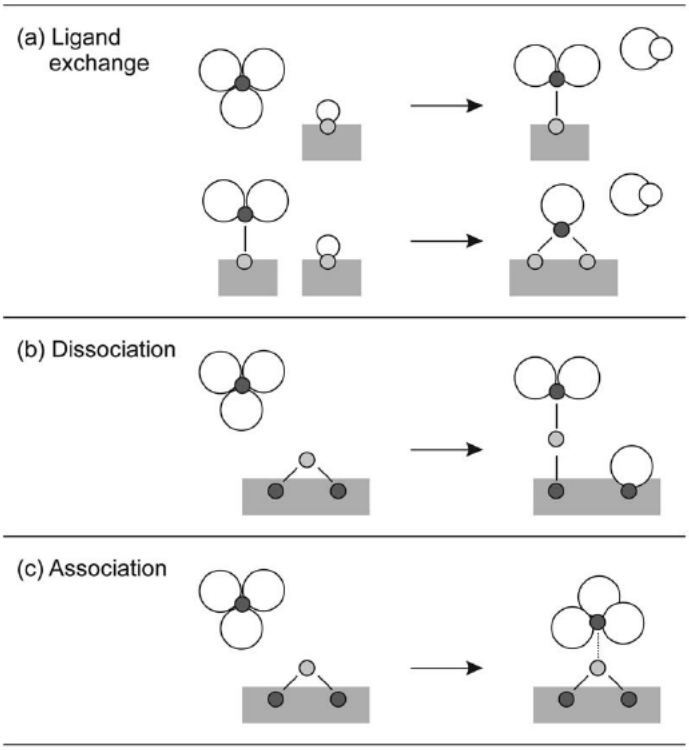

Fig. 3.3 Chemisorption mechanisms for ALD.[97]

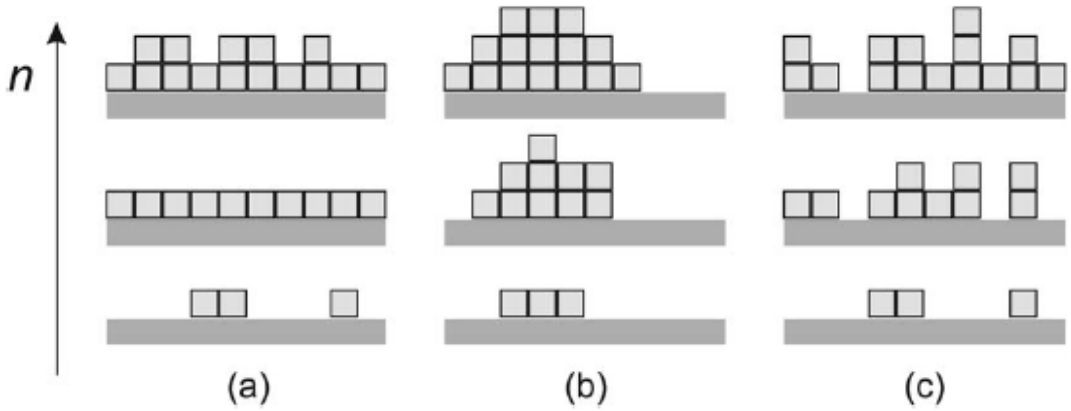

Fig. 3.4 Schematic illustration of growth mode: (a) 2D growth, (b) island growth, and (c) random deposition, where n is the cycle of growth.[97]

The most common ALD system is the ALD of Al_2O_3. There are two ways to deposit Al_2O_3: either one can use trimethylaluminum (TMA) and H_2O,[99,100] or TMA and ozone.[101,102] The formal one is thermal ALD, which is closely related to chemical vapor deposition (CVD); the latter one is plasma or radical-enhanced ALD, which can react at temperatures as low as room temperature. The growth thickness per AB cycle is 1.1~1.2Å,[103,104] which is comparable with the thickness of one Al_2O_3 'monolayer'. The mass gain per cycle from quartz crystal microbalance (QCM) and the thickness, which is determined by ellipsometric measurement, profilometry and AFM step height measurements, were used to estimate the density of 3.0 g/cm^3 for Al_2O_3 ALD films, reacted at 177 ° C.[105] The TMA/H_2O growth is self-terminated, and the GPC was independent of the reaction pressures. As shown in Fig. 3.5, the GPC decreases with temperature, due to the change of the inherent reaction mechanisms and variation in the number of reactive surface groups (i.e. OH groups). TMA/H_2O is 2D growth, because of the smooth layers formed and having the expected mass density.[103,106] For the chemisorption mechanisms, the Al_2O_3 ALD is a combination of ligand exchange with OH group (releasing methane), and dissociation with surface oxygen bridges.

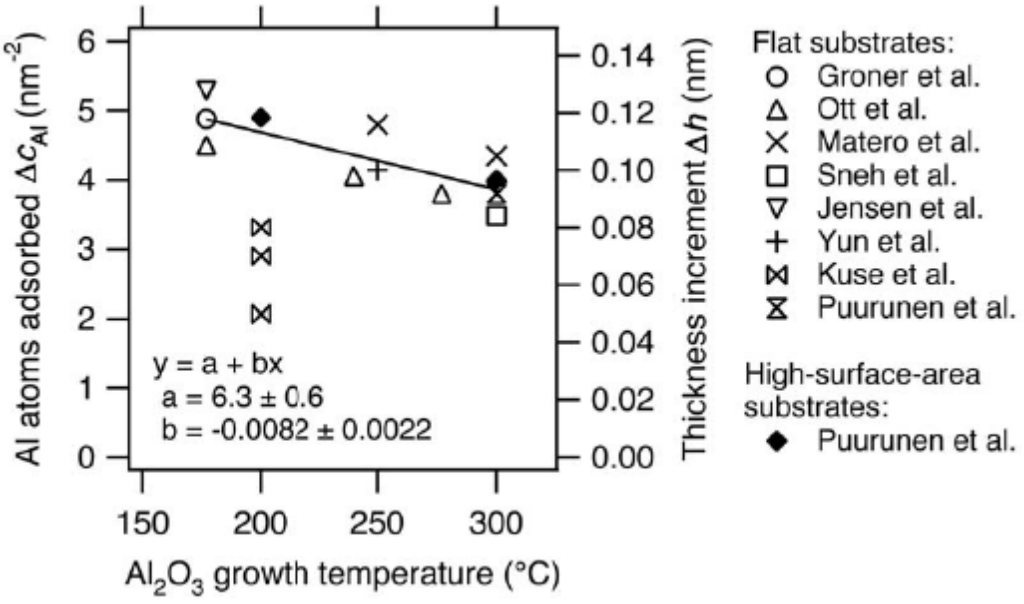

Fig. 3.5 GPC of TMA/H2O vs temperature.[103,107-113]

There are different types of ALD reactors. One kind of reactors' reactants is exposed without using a carrier gas and sometimes with throttled pumping.[103,114,115] On the other hand, some ALD reactors' reactants are exposed with a carrier gas (most of the flow is inert gases) flowing through the reactor.[104,116] Some 'batch' reactors can deposit on many samples simultaneously.

High- K dielectric ALD Al_2O_3 has been studied as a candidate to replace SiO_2 as gate electrics. Complementary metal oxide semiconductor (CMOS) field effect transistors (FET) have continued to be improved, following Moore's law for decades.[117] More and more devices in the same chip require smaller and smaller sizes of devices. But once the thickness of SiO_2 is smaller than 2nm, the strong gate leakage current exists from tunneling electrons through SiO_2.[117] Thus new material is desired to replace SiO_2 as a gate oxide.

The source-drain current of the FET controls by the gate capacitance:[117]

$$C_{gate} = \frac{K\varepsilon_0 A}{t} \tag{3-4}$$

where ε_0 is the vacuum permittivity, A is the area of the capacitance, K is the relative permittivity, and t is the thickness of the oxide. Tunneling current is extremely sensitive to the distance, which means increasing the thickness will dramatically reduce the leakage current. But adding the thickness of the oxide will also decrease the gate capacitance. The solution is to seek a high-K dielectric with thick oxide, which will limit the leakage current with relatively high gate capacitance.

Six conditions need to be satisfied to choose high-K dielectric as gate electrics.[117] (a) It needs high enough K value; (b) It needs to be thermodynamically stable, due to direct contact with Si; (c) It must be kinetically stable, since the high temperature annealing for the device is needed to release the impurities; (d) It should act as an insulator, which means the band offset of Si should be over 1 eV; (e) It needs to have good electrical inter face with Si; (f) It must have few bulk electrically active defects.[117] Al_2O_3 satisfies all the requirements for the high-K dielectric as gate electrics. Compared with other deposition methods, ALD Al_2O_3 has excellent coverage, good purity, pin-hole free, atomic thickness, and large area.[117]

Combination of ALD Al_2O_3 and carbon nanotube (CNT) or graphene leads to new applications. Graphene or CNT insulated and protected by passivation layer is necessary for its applications, such as, building blocks for the fabrication of nanodevices,[118] field effect transistors,[119,120] surrounded gate transistor,[121,122] field-emission electron sources,[123] and nanoprobes for microscopy.[124] ALD Al_2O_3 gives perfect protection as passivation layer for CNT or graphene. But direct deposition is difficult, since the surface of graphene or CNT is inert and does not contain chemical species that allow for the reaction. Consequently, isolated Al_2O_3 nanospheres are grown on defects of CNT and graphene, and nanoribbons are formulated along the step edges of the graphene surface.[125-127] Pretreatments are needed for the Al_2O_3 ALD

coating. Wet chemistry treatments, including inorganic or organic approaches,[128-135] are effective as pretreatments. But the liquid-based techniques are experimentally tedious and may not be scaled-up, and its functionalization changes the hybridization of CNT or graphene. Another method is using ozone or O_2 plasma to increase the surface energy of graphene before the coating, which introduced defects in the graphene lattice.[136,137] Certain substrate such as Cu may enhance the coating, but it is not a universal method for an arbitrary substrate or suspended graphene/CNT.[138] Compared with previous pretreatments method, we prefer NO_2/TMA pretreatment. It is simple, which can be finished in the same instrument as the coating. It is easy to scale up, and the only limit is the volume of the ALD coating chamber. This method does not change the property of CNT or graphene, and do not introduce any extra defects. The classical recipe is 50 cycles of NO_2/TMA at room temperature. NO_2 monolayer is physisorbed to CNT/graphene, and TMA is adsorbed onto the NO2. This forms a self-terminationg monolayer around CNT or on graphene, providing an adhesion layer for the nucleation and growth of Al_2O_3 ALD films, as shown in Fig. 3.6.[125,139,140]

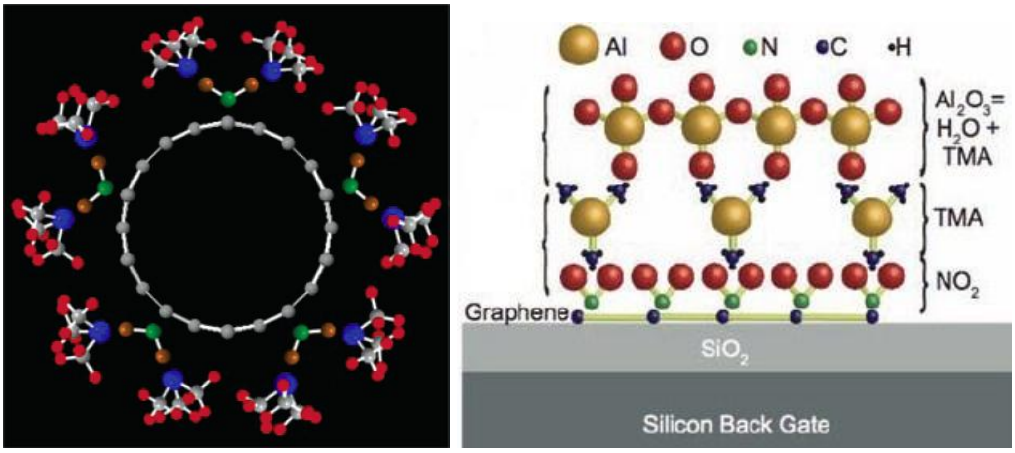

(a) (b)

Fig. 3.6 (a) Schematic of NO2/TMA functionalization mechanism. NO_2 is adsorbed on the CNT surface, followed by TMA.[139] (b) Illumination of oxide deposition process on graphene. NO_2/TMA pretreatment is followed by H_2O/TMA growth.[140]

3.3 Mechanical Properties of Al_2O_3 ALD

As stated previously, high dielectric constant (high-K) materials are known as a solution for reducing gate leakage current and dielectric breakdown beyond the 45 nm technology node. As one of the high-K material, Al_2O_3 ALD is well studied for its electrical properties. The previously less studied mechanical properties are essential to the design and engineering of ALD coated devices. What's more, the mechanical properties for 2D materials may be quite different as their bulk counterparts, due to their high surface area to volume ratio and their different material structures created by unique processing methods. The typical mechanical properties, we are considering, are Young's modulus, hardness, initial stress, and density.

Nanoindentation is a popular technique that has been employed to study many types of thin films. From the measured load vs depth relationship (Fig. 3.7), modulus and hardness may be determined. For example, from the raw indentation results (Fig. 3.8), the value of E = 183.9 ± 6.46 GPa and H = 11.6 ± 0.7 GPa were determined for Al_2O_3 films.[141]

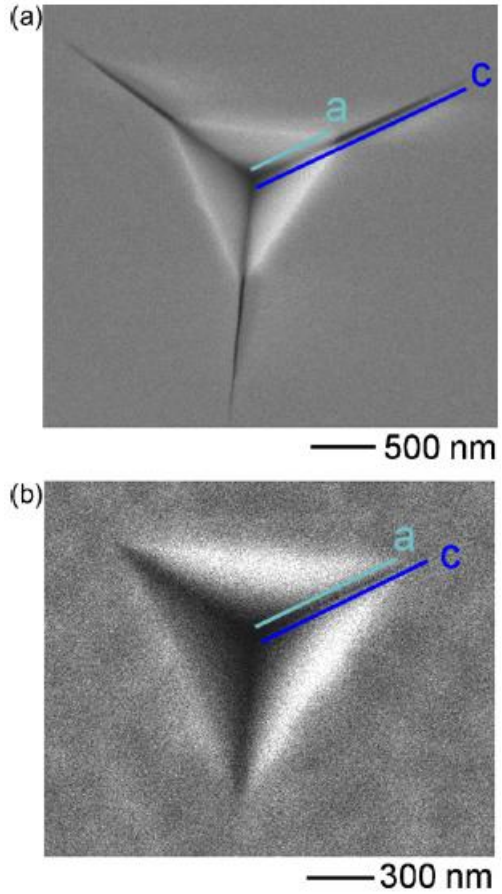

Fig. 3.7 FESEM images of the residual impression remaining after indentation to (a) Al_2O_3, and (b) SiO_2 coatings on Si.[141]

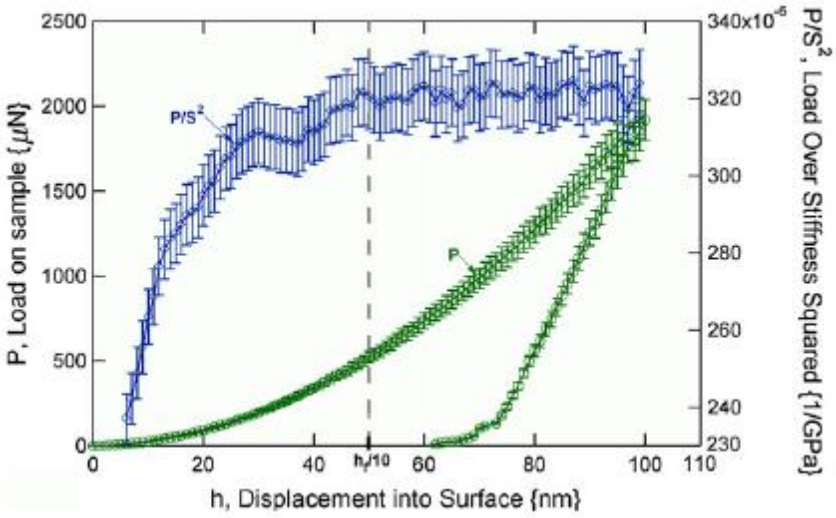

Fig. 3.8 load vs. depth for 500nm thick Al_2O_3 film on Si.[141]

Wafer curvature method measures the stress in Al_2O_3 films. As shown in Fig. 3.9, the films were heated to 275 ℃ and then cooled to 25 ℃. The data was recorded from three consecutive thermal cycles.[141]

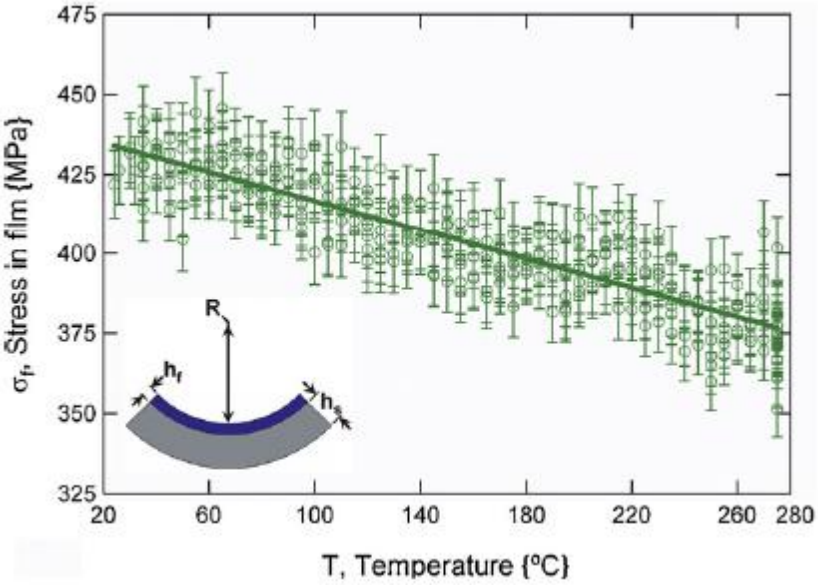

Fig. 3.9 Stress results for 100nm Al_2O_3 deposited on Si.[141]

Bulge test and nanobeam deflection can also be used to determine the Young's modulus of thin films. For bulge test, differential pressure was applied to the membrane (Fig. 3.10a). After finding out the deflection vs. pressure curves, Young's modulus can be calculated from: [142]

$$E = (p - \frac{4t\sigma_0}{r^2}\omega_0)/(\frac{(7-\upsilon)}{3(1-\upsilon)r^4}\omega_0^3) \quad (3\text{-}5)$$

where υ is the Poisson's ratio; E is the Young's modulus; p is the pressure difference; σ_0 is the initial tension, and ω_0 is the deflection. The Young's modulus was measured at 181 ± 20 GPa.[143]

According to nanobeam deflection measurement, a constant force was employed to the cantilever in different positions. The deflections were recorded, corresponding to the position (as shown in Fig. 3.10b). Young's modulus is:

$$E = 4 \cdot \frac{Fx^3}{\Delta z w t^3} \tag{3-6}$$

where E is the Young's modulus, Δz is the deflection, w the width, x the contact point, F the force, and t the thickness of the cantilever.[144] From the fit of the measured data, they got the Young's modulus is 168 ± 8 GPa for the 100nm-thick cantilever, and it is 182 ± 32 GPa for the 50nm-thick cantilever.[143]

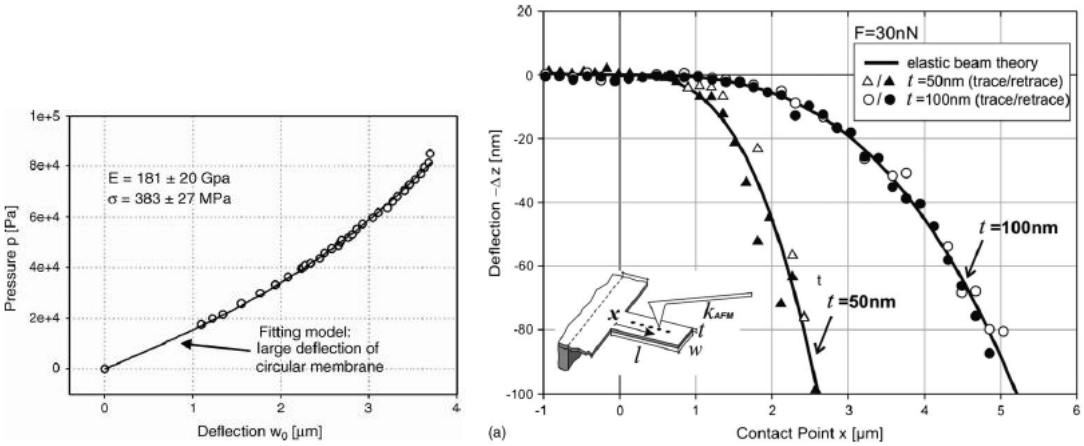

Fig. 3.10 (a) Bulge test results; (b) AFM-based nanobeam deflection measurements.[143]

Craighead's group demonstrated the ability to simultaneously measure Young's modulus and density of ~21nm ALD alumina by a resonance method using an interferometer. They have coated ALD films on both sides of the Si cantilever resonators (Fig. 3.11 a-h). The resonant frequencies are very sensitive to the mass change of the NEMS resonators, and the coating of the ALD will shift down the frequencies. They compared the resonant frequencies of both in-plane and out-of-plane modes for the resonators before and after coating (Fig. 3.11 i-j). From the comparison, the Young's modulus and density of coated films were deduced to be ~170 GPa and 3g/cm^3, respectively. [145]

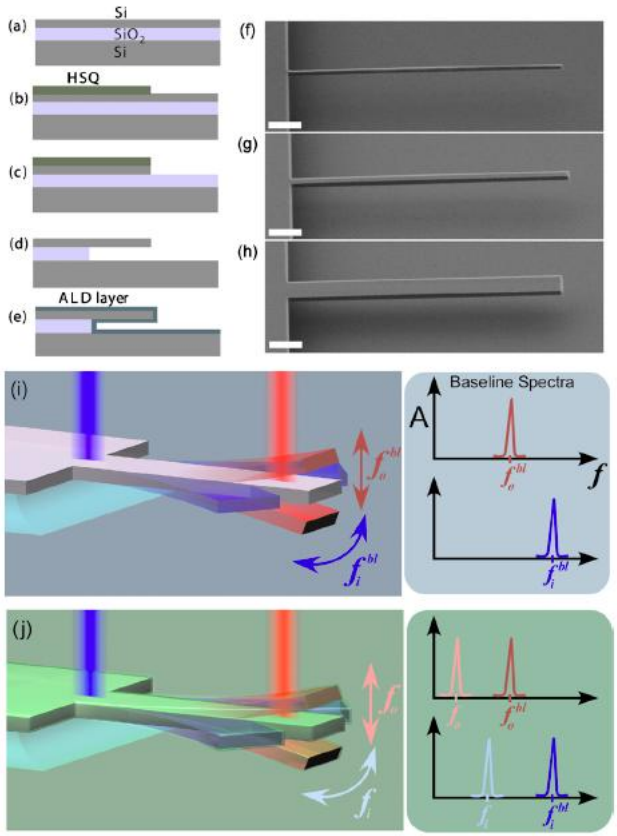

Fig. 3.11 Fabrication sequence of nanomechanical cantilevers devices and experimental schematic for measuring the NEMS resonators.[145]

3.4 Conclusions

ALD is an important technique mostly used in coating, but also can be used to create a structured membrane. The state of the art for the mechanical properties of Al_2O_3 ALD was reviewed. In chapter 5, we will present newly-determined mechanical properties of ultrathin ALD films.

Chapter 4 Single Nanopore Molecular Valves in Graphene for Controlling Gas Phase Transport

4.1 Introduction

The ability to control the quantity and location of a single file molecular flux to a precise location in space has important applications for nanoscale 3D printing, catalysis, and sensor design. Barrier materials containing pores with molecular dimensions have been used to control molecular compositions in the gas phase, but unlike their aqueous counterparts, none has enabled an ability to observe or control single pore transport.[146-156] Herein, we demonstrate gas transport through atomically thin, monolayer graphene opened with a single (nominally) molecular-sized, sub-nm pore demonstrating the ability to detect and control the gas flux. This is accomplished using ~nm sized gold clusters formed on the surface of the graphene. Such clusters migrate and partially block the pore. We also observe stochastic switching of small magnitude in the gas flux indicative of modulation by a single pore even without gold clusters. The stochastic switching is analyzed using a Hidden Markov Model to fit to discrete and repeatable states, and the switching frequency is used to estimate the energy of the transition that occurs. This work presents an example of creating single nanopore molecular valves to control gas phase transport through a comparably-sized pore.[9,61-63,90,157-164] These nanopore molecular valves open possibilities for unique sensors, catalytic processes, and approaches to molecular synthesis based on the controllable switching of a molecular gas flux reminiscent of ion channels in biological cell membranes and solid state nanopores.[38]

4.2 Material and Method

The methods for device fabrication and pressurization follow closely references. [8,50,79,165] Suspended graphene membranes were fabricated using mechanical exfoliation on silicon oxide substrates with predefined etched wells. The wells were defined by photolithography on an oxidized silicon wafer with 90nm silicon oxide on top and have a diameter of 4~5 μm. Reactive Ion Etching was used to etch the wells to a depth of 400~1000 nm, and the 'scotch tape' method was used to deposit graphene over the wells. The gold atoms were evaporated onto the graphene in vacuum (CVC 3-boat thermal evaporator, at 0.1 Å/s for less than 0.5 s).

To pressurize the inside of the microcavity, we put the sample into a high pressure chamber with a certain gas species at a prescribed pressure, which we call the charging pressure. After several hours or days, depending on the gas species used, the pressure in the microcavity comes to equilibrium with the charging pressure. The pristine graphene sheet is impermeable to any gases, but the gas can diffuse through the silicon oxide substrate. To reach pressure equilibrium, we wait 4~30 days, which is longer than the time for equilibrium to make sure the accuracy of the measurements.

After measuring the leaking rate for the pristine graphene, we etched pores by exposing the graphene membranes to a UV lamp (λ_1=185nm, λ_2=254nm) under ambient conditions. We first pressurized them with pure H_2 up to 200 kPa above ambient pressure. After the microcavity reached equilibrium we removed it from the pressure chamber and measured the deflection using AFM. We continue with a series of short UV exposures (less than one minute) followed by quick AFM scans (few minutes). Once a pore is created whose size is between H_2 and N_2, then the deflection abruptly changes from positive to negative. Once a pore is created, the leak rate is

dominated by transport through the pores and 1~12 hours of pressurization, depending on the gas species, is sufficient for equilibrium.

4.3 Leak Rate for Pristine Graphene

The leak rate can be derived from a mass balance on the microcavity using the ideal gas law and Hencky's solution for a clamped circular membrane and follows closely reference:[50]

$$\frac{dn}{dt} = \frac{1}{RT}[3K(\nu)\frac{Et}{a^4}\delta^2 \cdot (V_0 + V_b) + \left(P_{atm} + K(\nu)\frac{Et}{a^4}\delta^3\right) \cdot C(\nu)\pi a^2] \cdot \frac{d\delta}{dt} \qquad (4\text{-}1)$$

where R is the gas constant, T is the temperature, E = 1 TPa is the Young's modulus, t = 0.335 nm is the thickness of the membrane, a is the radius of the membrane (microwell), V_0 is the microcavity volume at zero deflection, V_b is the bulged up volume calculation from deflection, P_{atm} is the ambient pressure, δ is the maximum deflection of the membrane, $K(\nu = 0.16) = 3.09$, and $C(\nu = 0.16) = 0.52$ are constants determined by the Hencky's solution.

The maximum deflection versus time was measured for pristine unetched graphene membranes (Fig. 4.1). The samples were inserted into the high pressure chamber with ~200 kPa charging H_2. After few weeks, the internal pressure of the microcavity reached equilibrium with the charging pressure. Continuous AFM scanning was taken during the first 100 min of removal from the pressure chamber, and the deflection decreased by a few nanometers. From the slope of the deflection vs. time and equation 4-1, we determine that the permeance is ~6 x 10^{-25}mol $s^{-1}Pa^{-1}$, which is one order of magnitude slower than the H_2 permeance of the porous graphene membranes.

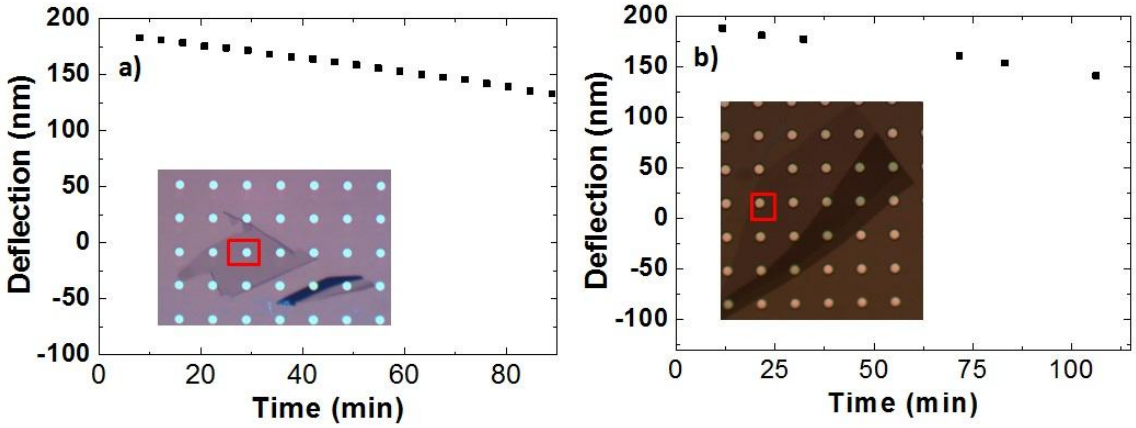

Fig. 4.1 Maximum deflection vs time before etching (a) Maximum deflection vs time for pristine graphene with gold, formed porous graphene membrane in section 4.5&4.6; (insets): optical image of monolayer graphene flake; (b) Maximum deflection vs time for pristine graphene, which was before etching for membrane in section 4.7&4.8 (inlay): optical image of monolayer graphene flake.

4.4 Description of Data Fitting (calculating permeance vs time)

Due to the stochastic nature of the switching of transport in the porous graphene, we developed a solution to determine the permeance as a function of maximum deflection. This is different than the solution of equation 4-1 from which we extract a constant permeance. For the porous membranes, we first used least square fit method to smooth the dn/dt data. In order to fit the data, we developed a model that describes the deflection of the microcavity versus time. We start with a mass balance based on the ideal gas law with P (pressure), V (volume), n (mols), and T (temperature) describing the state of the microcavity. The differential with respect to time describes the rate at which molecules leave the chamber, which is the transport rate.

$$PV = nRT \tag{4-2}$$

$$\frac{d}{dt}(PV) = RT\frac{dn}{dt} \tag{4-3}$$

Pressure and deflection are related by the mechanical properties of the graphene and geometry, therefore pressure (P) can be described as a function of deflection. Similarly, the

volume of the well is directly related to the deflection. Therefore the ideal gas law can be written with those two terms as function of the deflection.

$$\frac{d\delta}{dt}\frac{d(P(\delta)V(\delta))}{d\delta} = RT\frac{dn}{dt} \tag{4-4}$$

The relation between pressure and deflection is described by the following equation.

$$P(\delta) = \frac{EtK(\nu)}{a^4}\delta^3 + \frac{4S_0}{a^2}\delta + P_{atm} = p_3\delta^3 + p_1\delta + P_{atm} \tag{4-5}$$

where S_0 is the initial surface tension of the graphene which has a well known value of 0.1N/m.[8,165] The mechanical constants used are well established from numerous experiments of graphene membranes in a similar geometry.[7,50,79,165] For convenience, the parameters have been lumped into the constants p_1 and p_3. The relation between volume and deflection is described by the following equation.

$$V(\delta) = C(\nu)a^2\pi\delta + V_0 = \upsilon_1\delta + V_0 \tag{4-6}$$

The constants for linear deflection term have been lumped together into υ_1 for convenience.

The normalized dn/dt, which is proportional to permeance, is calculated by dividing dn/dt by the pressure difference of the effusing gas species. Classical effusion results in a linear relation between the rate of transport and the pressure difference, and therefore we define a constant value for normalized dn/dt, represented by k. The gas within the microcavity is assumed to be pure, and therefore total pressure $P(\delta)$ is equal to the partial pressure of the gas. P_{ext} is the partial pressure of the gas species in atmosphere and is approximately zero for all of the gases tested (except O_2 and N_2).

$$\frac{dn}{dt} = k(P(\delta) - P_{ext}) \tag{4-7}$$

By assuming this form for dn/dt, the differential equation can be written in terms of the deflection as follows.

$$\frac{d\delta}{dt}\frac{d(P(\delta)V(\delta))}{d\delta} = RTk(P(\delta) - P_{ext}) \tag{4-8}$$

$$\frac{d\delta}{dt}\left(\left(P_{atm}\upsilon_1 + p_1V_0\right) + \left(2p_1\upsilon_1\right)\delta + \left(3p_3V_0\right)\delta^2 + \left(4p_3\upsilon_1\right)\delta^3\right) = RTk(P_{atm} - P_{ext} + p_1\delta + p_3\delta^3) \tag{4-9}$$

The dependence on the deflection is represented as a single arbitrary function, y.

$$y(\delta) = \frac{\left(P_{atm}\upsilon_1 + p_1V_0\right) + \left(2p_1\upsilon_1\right)\delta + \left(3p_3V_0\right)\delta^2 + (4p_3\upsilon_1)\delta^3}{\left(P_{atm} - P_{ext}\right) + p_1\delta + p_3\delta^3} \tag{4-10}$$

$$y(\delta)\frac{d\delta}{dt} = RTk \tag{4-11}$$

The differential equation is separable and can be solved.

$$\int_{\delta_0}^{\delta} y(\delta)\,d\delta = RTk\int_0^t dt \tag{4-12}$$

$$Y(\delta) - Y(\delta_0) = RTkt \tag{4-13}$$

The resulting form is a line. The values of the integral, $Y(\delta)$, can be calculated numerically for each experimental deflection point. A segment of these values is fit using the analytical least squares line fit, and gives results for $Y(\delta_0)$ and k when temperature is known.

For the results of permeance or flux, the fitting method is applied to a segment of 5 data points, and the resulting values are assigned to the center data point. A value of k, the permeance, is calculated at each point by proceeding through the data set in this manner. Permeance values following only include points with deflection above 50 nm. Points below 50 nm were excluded because small errors in the pressure correlation, and small amounts of air in the microcavity in

some runs results in large errors in the permeance calculation at points lower than 50 nm deflection. When a full five points aren't available for the points at the beginning and end of the deflection data set, only the three or four nearest points are used to fit a value of permeation.

4.5 Stochastic Switching of Gas Transport by AuNC

We studied 2 types of nanopore molecular valves: a porous single layer of suspended graphene with no gold nanoclusters on its surface (PSLG) and a porous single layer of suspended graphene on top of which we evaporated gold nanoclusters (PSLG-AuNCs). To fabricate both types of devices, we start with suspended pristine monolayer graphene. The graphene is mechanically exfoliated over predefined etched wells on a silicon substrate with 90 nm of thermal silicon oxide on top. This forms a graphene-sealed microcavity which confines a $\sim \mu m^3$ volume of gas underneath the suspended graphene. For the PSLG-AuNCs samples, gold atoms are evaporated onto the graphene after exfoliation and prior to poration. Molecular sized pores in the graphene are introduced using UV-induced oxidation.[50] In the first few hours after UV-induced oxidation, the gold clusters are observed to migrate and congregate on the surface of the graphene (Fig. 4.2a-b).

A pressurized blister test is used to determine the leak rate out of the graphene sealed microcavity.[50] The microcavity is filled with 300 kPa of pure H_2, and the membrane is bulged up due to the pressure difference across the membrane (Fig. 4.3a and d). We then monitor the deflection of the membrane using an AFM (Fig. 4.3d-f). For the PSLG-AuNC device, the leak rate of gas out of the microcavity is slow initially, and the membrane deflection changes slowly

with time (Fig. 4.3d). A fit to a membrane mechanics model is shown as a red line. During scanning there is a sudden jump in the deflection and a much faster leak rate is observed (Fig. 4.3e). This change from bulged up to bulged down occurs in ~30 s and is indicative of a rapid leaking of all of the H_2 gas inside the microcavity, while any leak of air back into the cavity is much slower. A line cut through the center of the membrane during this process is shown in Fig. 4.4. From the line cut (blue lines in Fig. 4.3 d-f), we can see the maximum deflection drops from 147nm to -115nm in ~1 minute (Fig. 4.5). We attribute this sudden change in the deflection to migration of the gold nanoclusters on the surface of the membrane that "opened" a single pore in the graphene membrane allowing a fast leak rate (Fig. 4.3a-c). A single pore in the graphene membrane is likely responsible for the sudden change in permeance since it is unlikely that multiple identical pores opened simultaneously.

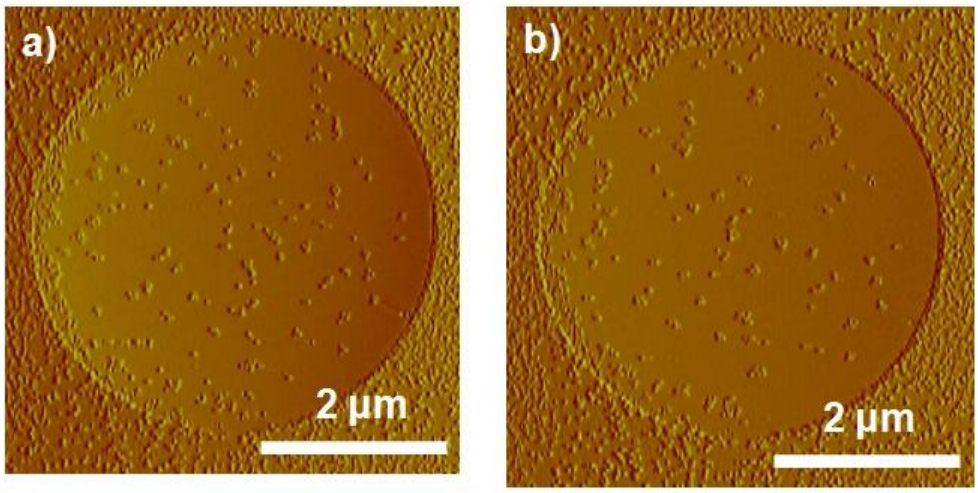

Fig. 4.2 AFM amplitude images showing the movement of gold nanoparticles on a suspended graphene membrane.

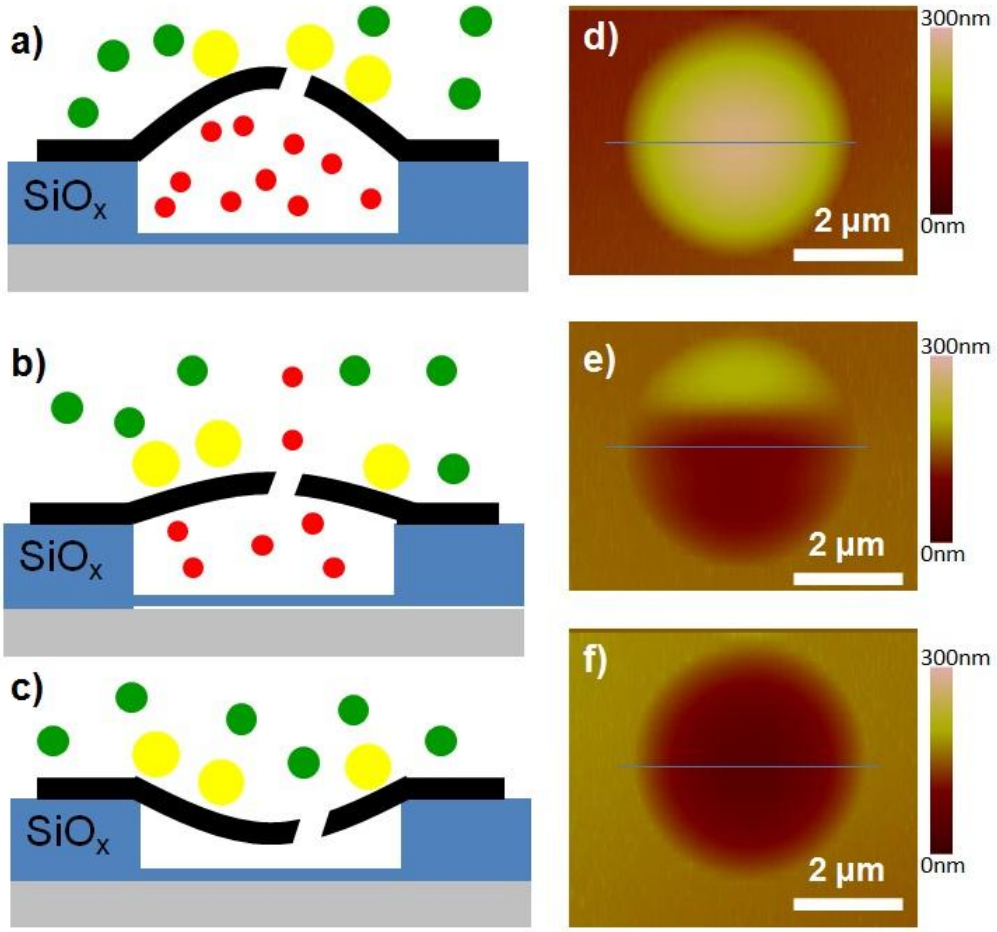

Fig. 4.3 (a-c) Schematic of the gold nanoparticles (yellow solid circles) blocking and unblocking the pore on the monolayer graphene membrane; (d-f) AFM height images capturing the deflection change in (a-c).

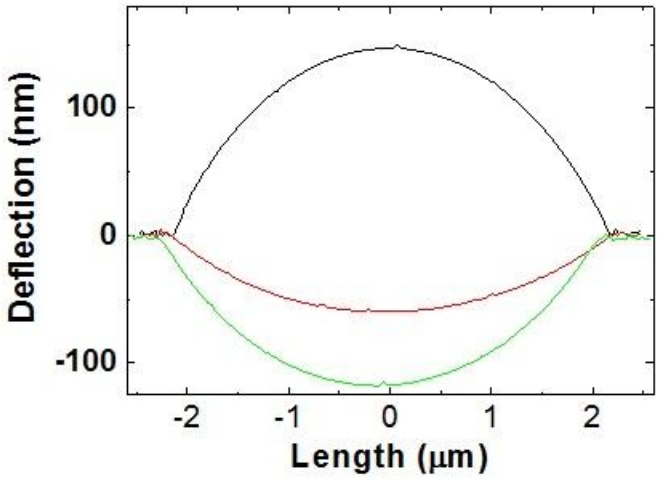

Fig. 4.4 Deflection vs. position through the center of the membrane in Fig. 4.3 (d-f).

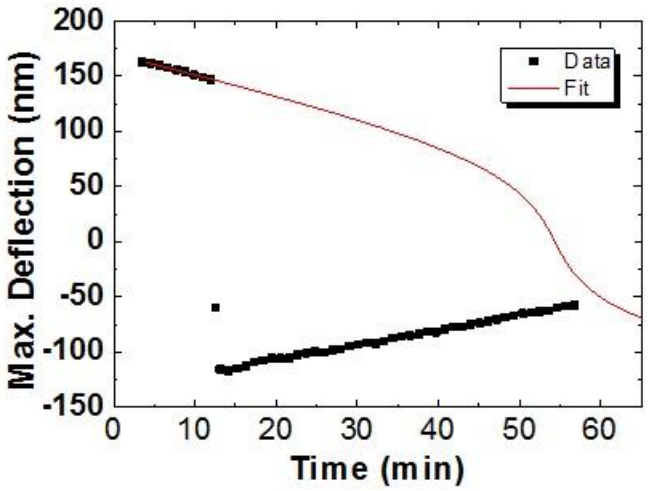

Fig. 4.5 Maximum deflection vs. time for the dramatic leak rate change. The solid red line is a fit to the data before switching using the membrane mechanics model.

Fig. 4.5 plots an extrapolated fit of the deflection data before the sudden drop in deflection. This extrapolation represents the expected trajectory if the pore had continued in the blocked state at the start of the run. It was calculated by numerically linearizing the deflection data prior to the sudden drop (0 to 12 minutes) via equation 4-12 to the form of equation 4-13. From the analytical least squares fit, values for the two parameters, $Y(\delta_0)$ and k, can be determined based on all the points in the range of 0 to 12 minutes.

To create a fit and extrapolation for the deflection, a set of artificial evenly spaced deflection values between the maximum and minimum deflections are put in the form of equation 4-13. The fitted values of the two parameters, $Y(\delta_0)$ and k, are used to solve for time at each of the artificial deflection points. Then the artificial deflection points are plotted against the calculated times as the fit and extrapolation.

4.6 Controlling the Leak Rate by Laser Induced Heating

The change in permeance can be trigged by laser induced heating in vacuum to stimulate movement of the AuNCs. After that, we pressurized the sample in the same chamber to reach the designed pressure in the microcavity. After which the method was the same as previously described in 'Material and Method' section. In this case, the membrane in Fig. 4.2 displays a fast permeance as evidence from a decrease in the maximum deflection vs. time of H_2 gas taking place in less than 30 minutes (Fig. 4.6). The permeance is relatively constant over many measurements at different starting internal pressures of hydrogen suggesting that eventually the AuNCs have stopped migrating. This is further confirmed by AFM images (Fig. 4.6 inset) which show the configuration of AuNCs as stable. After shining a laser on the surface of the membrane, the permeance slows considerably, now taking ~ 30 – 90 minutes to leak out depending on the initial internal pressure (Fig. 4.7). Again the leak rate is stable during these measurements over multiple internal pressures. An AFM image of the surface of the membrane after laser exposure shows a change in the configuration of AuNC on the surface of the membrane (Fig. 4.7 inset).

From the max deflection vs. time curves (Fig. 4.6 and 4.7), the rate of change of the number of molecules, n, constitutes a leak rate dn/dt that can be extracted assuming the simple membrane mechanics model (Fig. 4.8a).[50] We observe that the leak rate shows a linear dependence on the pressure difference with a slope of $8.41 \pm 0.26 \times 10^{-24}$ mol-s^{-1}-Pa^{-1} before and $1.70 \pm 0.02 \times 10^{-24}$ mol-s^{-1}-Pa^{-1} after laser exposure, consistent with nanopore transport[63]. A histogram of the leak rate normalized by the pressure difference, which we define as the permeance, is shown in Fig. 4.8b. Counts on the histogram correspond to a permeance calculation based on the slope around each deflection data point. There are clearly 2 defined states of the leak rate before and after laser exposure.

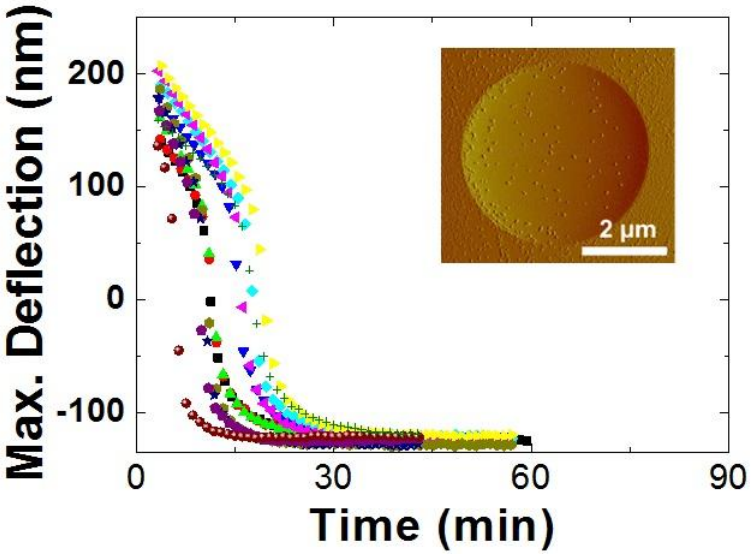

Fig. 4.6 Maximum deflection of the graphene membrane before focusing a laser beam at the center of the membrane. Different colors represent different charging pressures. The charging pressure is from 200 kPa to 700 kPa to 200 kPa, in 100 kPa increments; (inset) AFM amplitude images of the graphene membrane corresponding to the state of the graphene membrane for the measurements.

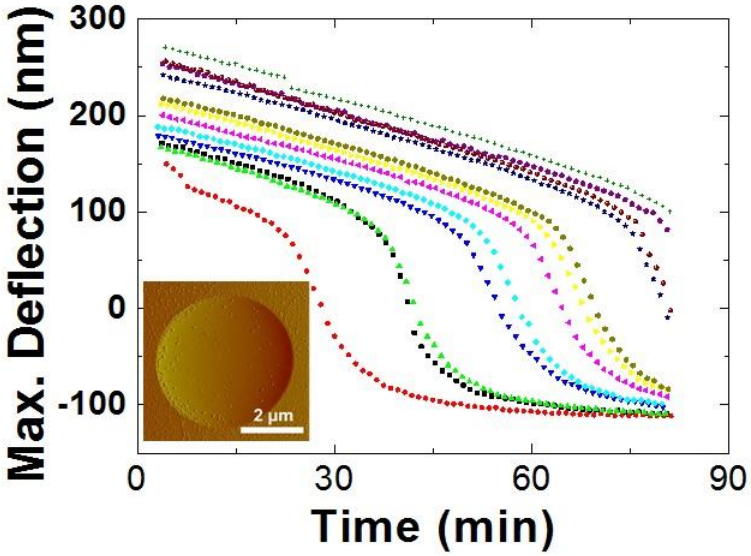

Fig. 4.7 Maximum deflection of the graphene membrane after focusing a laser beam at the center of the membrane. Different colors represent different charging pressures. The charging pressure is from 200 kPa to 850 kPa, in 50 kPa, 100 kPa, or 150 kPa increments. (inset) AFM amplitude images of the graphene membrane corresponding to the state of the graphene membrane for the measurements.

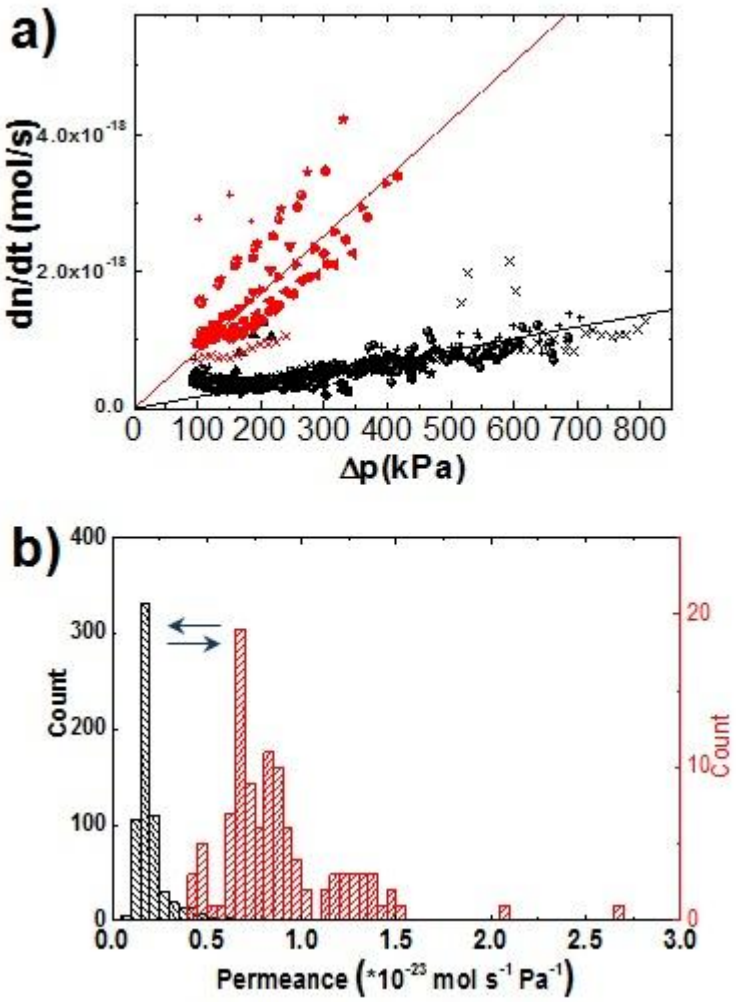

Fig. 4.8 (a) Leak rate dn/dt vs. pressure difference Δp for Fig. 4.6-shown in red and Fig. 4.7 – shown in black; (b) Histogram of the permeance from (data in (a) –red) and (data in (b)-black).

Fig. 4.8 shows switching of the permeance by laser induced heating which moves the AuNCs towards the pore site. This process is reversible. Further experiments on the same graphene membrane in Fig. 4.8 continue to show a slow leak rate (gray colored bar). Additional laser induced heating of the membrane resulted in a faster permeance shown by the magenta colored bars in Fig. 4.9.

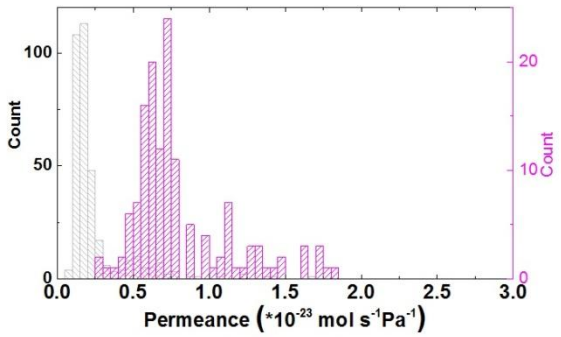

Fig. 4.9 Histogram of the permeance from (data in gray) to (data in magenta) by laser induced heating again.

Gas transport through the porous graphene membranes can be modeled using classical effusion. When the pore size is smaller than the mean free path of the molecule, classical effusion dictates that the time constant for the decay of the number of molecules in the graphene sealed microcavity is given by:

$$\tau = \frac{V}{\gamma}\sqrt{\frac{2\pi M_w}{\mathrm{R}T}} \tag{4-14}$$

where V is the volume of the container, γ is the transmission coefficient, M_w is the molecular mass, R is the ideal gas constant, and T is the temperature.[52] The transmission coefficient, γ, incorporates both the physical geometry of the pore, and any energy barrier from molecular interactions between the molecule and the pore. Due to the small volume of gas in the graphene sealed microchamber (~1 μm^3), the time constant for the effusion due to a single defect can be considerably long (tens of minutes) making our geometry ideally suited for measuring the leak rate through a single sub-nm pore and for observing sub-$Å^2$ changes in the transmission coefficient. Correspondingly, the leak rate dn/dt assuming classical effusion is given by:

$$\frac{\mathrm{dn}}{\mathrm{dt}} = \frac{\gamma}{\sqrt{2\pi M_w \mathrm{R}T}} \cdot \Delta p \tag{4-15}$$

where Δp is the pressure difference across the membrane [63]. A plot of dn/dt vs. Δp shows a linear dependence further supporting classical effusion (Fig. 4.8a). The transmission coefficient can be

deduced from the slope and changes from 0.15 Å^2 (before) to 0.03 Å^2 (after) laser heating. The transmission coefficient is the geometric area of the pore (a few Å^2) multiplied by a transmission probability that an impinging gas atom or molecule has sufficient energy to pass through the potential barrier of the pore. Hence, γ is considerably smaller than the cross sectional area of the test gas H_2 (2.89 Å) providing further evidence that the pore is on the order of the kinetic diameter of H_2 and we are measuring small changes in the energy barrier from molecular interactions between the gas and pore mouth.

4.7 Influence of Gas Species on Leak Rate

The ability to observe small changes in γ allows us to vary the molecular size and study how that influences gas transport in the same SLGM. For this study, we used a single SLGM that contained no AuNCs. The leak rate, dn/dt, of helium gas through SLGM shows a linear dependence on Δp and is relatively constant over a range of Δp from 200 kPa to 700 kPa (Fig. 4.10 inset). This agrees with classical effusion with a slope equal to 1.5 $\pm$0.01 x 10^{-23} mol-s^{-1}-Pa^{-1} corresponding to γ = 0.36 Å^2 (Fig. 4.10). The permeance for other noble gases, Ar, Ne, as well as He, are shown as a histogram with average values and standard deviations of 4.1 $\pm$2.1 x 10^{-25}, 2.5 $\pm$1.6 x 10^{-24}, and 1.5 $\pm$0.2 x 10^{-23} mol-s^{-1}-Pa^{-1}, respectively (Fig. 4.11). This follows a trend of a slower leak rates for larger gas atoms. In addition to the noble gases, we measured the leak rate of the non-noble gas molecules, H_2, CO_2, and N_2O both before and after introducing the molecular-sized pores (Fig. 4.12). Data for the non-porated graphene was taken on a separate but similar monolayer graphene membrane and the measured leak rates agree well with a leak

primarily through the underlying silicon oxide substrate.[8,50,79] In all cases, there was a considerable increase in the leak rate after poration supporting that the leak rate is primarily through the molecular-sized pore.

We can deduce the transmission coefficient as a function of the kinetic diameter for all the gases measured. As expected for the noble gases, the transmission coefficient increases as the kinetic diameter decreases: (Ar) 0.027 ±0.017 Å^2, (Ne) 0.14 ±0.09 Å^2, and (He) 0.36 ±0.05 Å^2 (Fig. 4.13), further confirming that the pore size is on the order of the kinetic diameter and showing the influence of the molecular size on γ. In addition, the leak rate of H_2, roughly follows the trend observed with the noble gas atoms. However, CO_2 and N_2O follow a very different trend (inset Fig. 4.13). Their leak rates and transmission coefficients are considerably larger than one would expect from their kinetic diameter (CO_2) 0.65 ±0.52 Å^2, and (N_2O) 1.52 ±1.21 Å^2. We attribute this to chemical interactions that N_2O and CO_2 have with the pore which lowers the energy barrier to transport. These experiments demonstrate that gas transport of polar gas molecules clearly shows a strong influence on chemical interactions between the molecule and the pore consistent with recent theoretical calculations.[161,163]

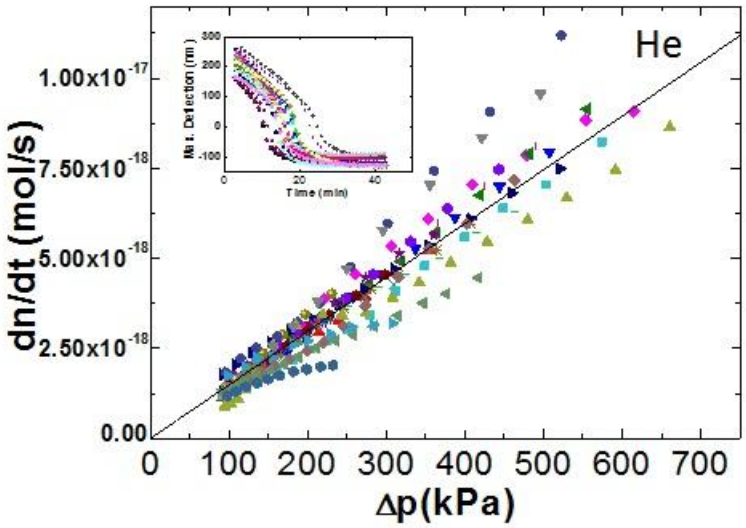

Fig. 4.10 Leak rate dn/dt vs. pressure difference *Δp* for He gas (inset) Maximum deflection vs. time for He gas.

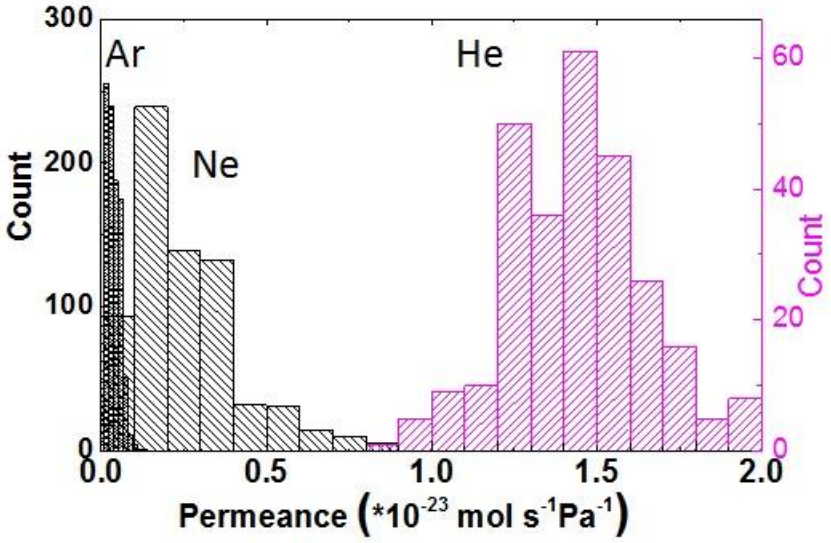

Fig. 4.11 Histogram of permeance for the noble gases, Ar, Ne, and He.

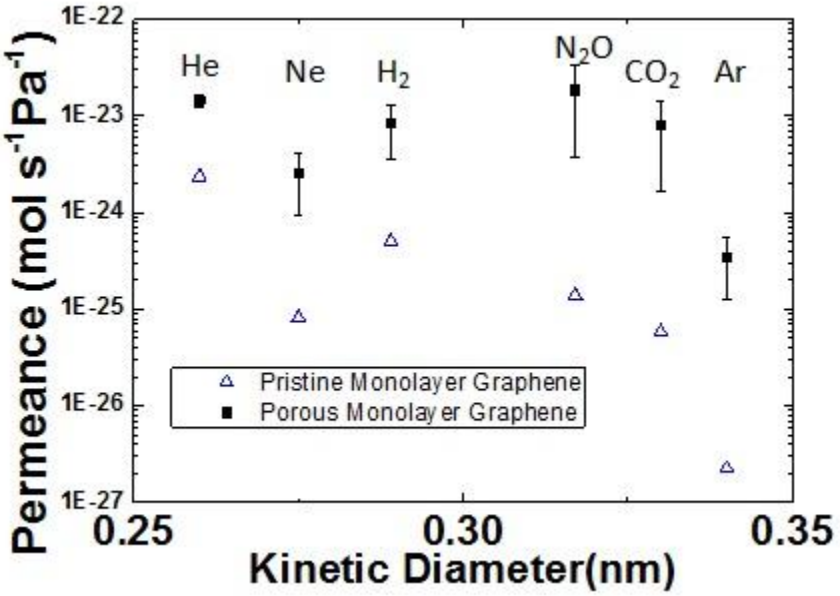

Fig. 4.12 Permeance vs. kinetic diameter for all of the measured gases before (blue) and after (black) etching.

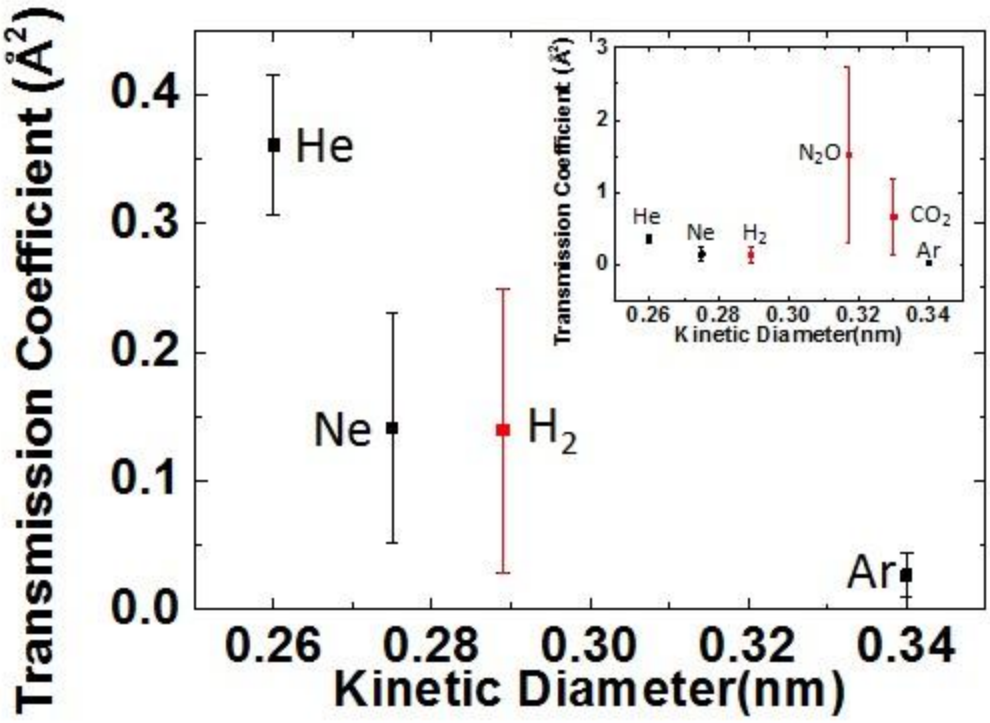

Fig. 4.13 Transmission coefficient vs. kinetic diameter for He, Ne, H_2, and Ar. (inset) Transmission coefficient vs. kinetic diameter for He, Ne, H_2, N_2O, CO_2, and Ar.

The original data of the max deflection vs. time for He, Ne, Ar, H_2, N_2O, and CO_2 are shown in Fig. 4.14. Different colors represent different measurement for the same PSLG. From

this data, we extracted the leak rate dn/dt vs. pressure difference Δp and the corresponding permeance.

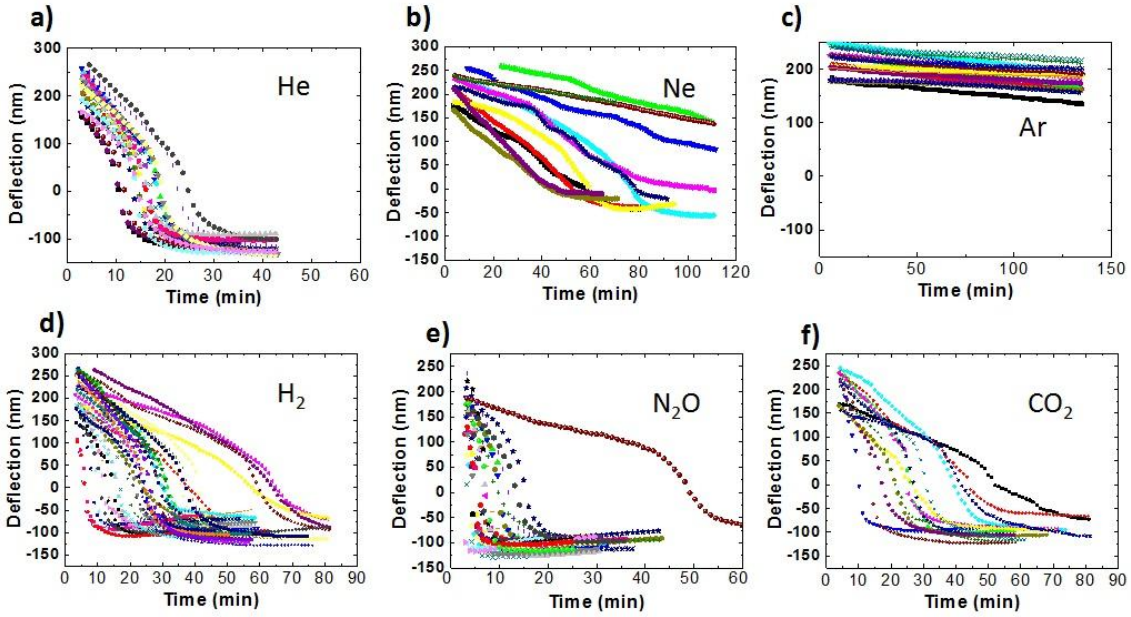

Fig. 4.14 Maximum Deflection vs time of multiple gases for porous monolayer graphene membrane in Fig. 4.12&4.13.

4.8 Schocastic Switching of Porous Graphene without AuNC

Though the leak rates are relatively constant over long time periods (days) of repeated measurements, the transmission coefficient demonstrates discretized fluctuations indicative of stochastic switching. Fig. 4.15a shows the concatenated permeance over time along with a fit to discrete states using Hidden Markov modeling (see details below). The data in Fig. 4.15a was taken over the course of five days where a dashed line corresponds to the start of a new measurement. All measurements are concatenated into a single observed time axis so that the repetition of certain states and values of permeance can be seen. This switching is clearly seen in Fig. 4.15b where the permeance switches five times within 1 hour (black circles). The histogram

of the permeance for Ne is plotted in Fig. 4.15c. The permeance shows a large number of states on the low end of the spectrum with occasional switching to faster leak rates. We fit these permeance values versus time to discrete states and applied a Hidden Markov model (HMM) to elucidate transition rates [166,167]. The frequency of switching between the states also yields an approximate value for the activation energy of the switching process, 0.9 eV. This is comparable to the activation energy required for rearrangement of molecule bonds, such as cis-trans isomerization.[168] These calculations comparing a the model pore and experimental results demonstrate that relatively minor changes in the pore can have an observable impact on the permeation characteristics of the pore.

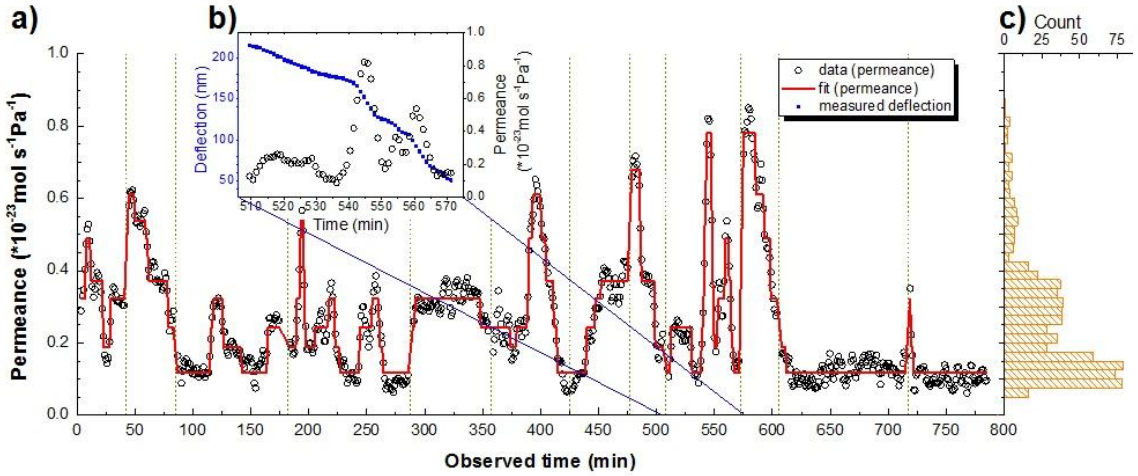

Fig. 4.15 Stochastic switching of the leak rate through porous monolayer graphene without gold nanoparticles (a) Permeance (black circles) and fit (red line) vs. time for all the Ne data. Bottom axis, observable time, corresponds to the 800 minutes of measurements taken over five days after repeated pressurization. Each measurement is separated by a dashed line. (b) Single experimental run within (a) matching highlighted time range. Left axis, blue squares - Maximum deflection versus time for Neon. Right axis– permeance vs. time calculated from the change in deflection vs. time in. (c) Histogram of the permeance for all the data in (a).

For fitting permeance versus time to discrete states, we applied a hidden Markov model (HMM). HMM describes a system that can switch between various states, however the states are not directly observable and must be inferred from changes in output. This type of modeling has

been applied in fluorescence and sensing applications to model the changes in observed fluorescence from interactions with an analyte.[169] The states and fit were calculated using the program HaMMy, which was originally developed for HMM analysis of FRET systems.[167]

The data from multiple runs was analyzed together by concatenating all data sets so that they have a shared time axis, called observed time. This represents the time in which data was being measured. The experiments for Ne were done over the course of five days, and the time between experiments is excluded for the fitting but noted by dashed lines in Fig. 4.15. For estimating the frequency of transitions between states, the transitions that occurred between the end of the previous experiment and the start of the next are excluded. Only points and time when the deflection is above 50 nm are included. When input into the program HaMMy, the permeance data is normalized by the maximum value, however, after the Markov model fit is generated, the permeance is converted back to absolute values.

The fitting algorithm fits the data to states that are distinct from each other and treats the transitions between states as instantaneous. The program was used to fit up to ten states, but it can also return empty states if the number of recognizable states is lower than ten.

The frequency of transitions between states can be used to estimate the activation energy of the pore transitions. For Ne, the hidden Markov modeling identified 26 transitions that did not occur during the time between experimental runs. The total observed time was 785 minutes. Therefore, the frequency is about 1 transition per 30 minutes, or $2\text{x}10^{-3}$ 1/s. The kinetic rate constant is approximately equivalent to the frequency. For an elementary process, the kinetic rate constant consists of an attempt frequency, *A*, and an exponential dependence on activation energy.

$$k = Ae^{-E_a/RT} \approx 2\times10^{-3}\ 1/s \tag{4-16}$$

Molecular vibrations typically occur within a few orders of magnitude of 10^{13} 1/s.[170] We assume A=10^{13}, and our data give us k based on one switching in 30minutes. Assuming a temperature of 298 K, the activation energy for a transition, E_a, can be estimated as 0.94 eV.

4.9 Estimation of Change in Permeance from Pore Rearrangement

We attribute the stochastic switching in leak rates to small fluctuations at the pore site which modulate the transmission probability. One possible source of fluctuations is reaction of the pore edge functionalization with atmospheric species; another is pore isomerization, in which the pore transitions between stable chemical states through rearrangement, but no gain or loss, of the atoms around the pore. Fig. 4.16a illustrates the simplest possible rearrangement: moving a single carbon atom in a simplified model pore which excludes functionalization. The effective size is around the expected pore size based on the observed molecular sieving. Even for this simplified model, this small rearrangement results in a relatively significant change in the energy barrier, as shown in Fig. 4.16b. That change in the model pore's estimated energy barrier gives an expected change in the permeance of around a factor of two or three, which is consistent with the magnitude of the experimentally observed changes in Fig. 4.15. The sensitivity of the leak rate to small rearrangements at a single pore further supports the hypothesis that a single pore is responsible for the observed gas transport in the measured porous graphene.

a)

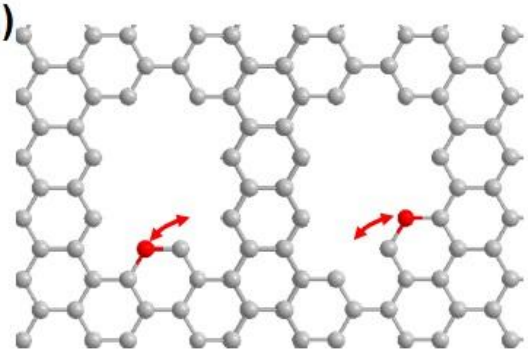

b)

Gas	Calculated energy barrier /(R*298 K) Left pore	Right pore	Expected ratio of permeances (right/ left)
He	0	0	1.0
Ne	0	0.73	0.5
H_2	0	1.12	0.3

Fig. 4.16 Atom Rearrangement at pore mouth. (a) Representation of a simple model pore rearrangement. (b) Estimation of barrier energy for two pores depicted in (a) and the expected ratio of permeance between the two.

In Fig. 4.16 b, it was shown that a small rearrangement in the pore could result in a meaningful change in the barrier energy and the expected permeance. The ratio is derived from an alternate form of equation 4-15 rearranged in terms of permeance, θ. The transmission coefficient, γ, is expanded into a geometric area term, a_g, and a barrier energy, E_a, term.

$$\theta = \frac{1}{\Delta p}\frac{\mathrm{dn}}{\mathrm{dt}} = \frac{\gamma}{\sqrt{2\pi M_w \mathrm{R}T}} = \frac{a_g e^{-E_a/RT}}{\sqrt{2\pi M_w \mathrm{R}T}} \tag{4-17}$$

When there is a pore rearrangement, both component terms of the effective pore area can change. However, as a first order approximation, we will assume only the geometric area term remains approximately constant. Therefore, the ratio of the permeances reported in Fig. 4.16b is simply the following:

$$\frac{\theta_2}{\theta_1} = \frac{a_{g,2} e^{-E_{a,2}/RT}}{a_{g,1} e^{-E_{a,1}/RT}} \sim \frac{e^{-E_{a,2}/RT}}{e^{-E_{a,1}/RT}} \tag{4-18}$$

The energy barriers for pore configuration 1, $E_{a,1}$, and pore configuration 2, $E_{a,2}$, are calculated using a single-center Lennard-Jones potential with the following parameters.

Table 6 Parameters for Lennard-Jones Potential Calculation

Center	σ (Å)	ϵ / k_B (K)
C [171]	2.960	34.2
Ar [172]	3.542	93.3
He [172]	2.551	10.22
Ne [172]	2.820	32.8
CO_2 [172]	3.941	195.2
H_2 [172]	2.827	59.7
N_2 [172]	3.798	71.4
N_2O [172]	3.828	232.4
O_2 [172]	3.467	106.7

Fig. 4.16b only includes He, H_2, and Ne. The full list of energy barriers is listed below. Energy barriers that are negative mean that the interaction energy for being in the center of the pore is more favorable than as a free gas molecule; the energy barrier is treated as zero in this case. For the larger molecules the energy barrier is larger and means those molecules would permeate very slowly, effectively blocked relative to the low barrier. CO_2 and N_2O show large energy barriers even though experiments show they permeate quickly; as discussed in the manuscript, this is believed to be the result of favorable electronic interactions that lower the total interaction energy, which is not captured by the simple Lennard-Jones (L-J) potential.

Table 7 Calculated Energy Barriers

	L-J Energy barrier Ea/(R*298)	
Gas	Fig 4.16a Left	Fig 4.16a Right
He	0 (-0.83)	0 (-0.37)
Ne	0 (-0.96)	0.73
H_2	0 (-1.36)	1.12
O_2	7.29	23.8
Ar	8.55	25.7
N_2	14.5	36.8
CO_2	45.5	109.2
N_2O	40.9	102.4

4.10 Conclusions

In conclusion, we created molecular valves in graphene which allow us to control the gas flux through a single (nominally) molecular-sized nanopore. The process can be controlled by movement of AuNC on the graphene surface. These results lead to a greater understanding of molecular gas transport through molecular-sized pores in atomically-thin materials. The switching observed may lead to unique sensors based on the reversible switching of molecular transport through ~atomic size pores reminiscent of ion channels in biological cell membranes, i. e. sensors for molecules that change configurations, or single molecule binding events.

Chapter 5 Ultrathin Oxide Films by Atomic Layer Deposition on Graphene

5.1 Introduction

Two-dimensional (2D) materials are promising nanomechanical structures.[12,29] Graphene, the best known and studied of this class of materials, boasts a high Young's modulus, intrinsic strength, gas impermeability, and excellent thermal and electrical conductivity.[7,8,14,18,87] There are possible applications where flexible ultrathin insulating or oxide films are needed with comparable mechanical properties. The integration of graphene with other two dimensional (2D) or quasi-2D materials may also lead to new functional properties for the composite materials.[140,173-176] Currently, the range of ultra-thin materials is severely limited by the materials and length-scales that are accessible through thin film fabrication.

Mechanical and chemical exfoliation, as well as growth techniques such as chemical vapor deposition, can produce just a handful of ultra-thin layered materials.[23,29,31,177,178] As traditional materials approach ~ 1 nm film thicknesses, fabrication of freely suspended films is difficult due to stresses or significant voids in the films that destroy the mechanical integrity of the film. To overcome these problems, we use suspended graphene membranes as sacrificial supports to grow high quality ALD films and then remove the graphene to leave the ALD thin film. These experiments demonstrate that ALD on graphene offers a route to create free-standing, ultrathin, quasi-2D structures with atomically controlled thickness and mechanical properties comparable to their bulk counterparts.[92,104,179,180]

5.2 Experimental Methods

Graphene is deposited using mechanical exfoliation over pre-defined etched wells similar to previously described methods (see Fig. 5.1a).[8,29,79] A series of wells with ~5-8 μm diameters were defined by photolithography on a silicon wafer with 90 nm of thermally grown silicon oxide. Dry plasma etching (CF_4 + O_2, followed by SF_6) is used to etch wells that are 500 nm – 3 μm and the "scotch tape" method is used to deposit graphene.[29]

Atomic layer deposition on the graphene is performed in a homebuilt reactor following a recipe similar to one previously reported for ALD alumina growth on carbon nanotubes.[125,139] The samples are placed inside the ALD reactor, pumped down to ~30 mTorr, and held at 180 ℃ for 30 min - 1 h before beginning the reaction. The reactor is purged with 20 sequences of argon purging before performing the NO_2/TMA nucleation treatment. Each argon purge involved dosing argon to 1 Torr for 60 s and then pumping for 60 s.

The nucleation treatment involves a dose of NO_2 to 1 Torr for 60 s followed by pumping for 60 s. Subsequently, a dose of TMA to 1 Torr for 60 s is applied, followed by pumping for 60 s. This process is repeated 10 times. After forming this adhesion layer, ALD of alumina is performed by cycling TMA/H_20 doses as follows: dose TMA to 1 Torr for 60 sec, pump for 60 sec, then dose Argon at 20 Torr for 60 sec and pump for 60 seconds 5 times, dose H_2O to 1 Torr for 60 s, pump for 60 s, then dose Argon at 20 Torr for 60 s and pump for 60 s 5 times. This represents 1 cycle of ALD. After the TMA/H_2O cycles are complete, the reactor is purged again with argon and then the samples are removed. All reactions were performed at 180 ($\pm$0.5) ℃.

In summary, atomic layer deposition films are fabricated using a combination of deposition and etching using a suspended graphene support. The graphene provides an atomically-smooth growth surface that can easily be etched away. Graphene is mechanically

exfoliated over predefined wells as illustrated in Fig. 5.1a. The graphene is then exposed to a trimethylaluminum (TMA) and NO_2 treatment that forms an adhesion layer for ALD nucleation.[125,134,139] Aluminum oxide ALD is subsequently grown using TMA/H_2O doses.[103,181] An example of such a graphene/ALD composite film after 7 cycles of alumina ALD is shown in Fig. 5.1b. We then use oxidative etching of the underlying graphene support to leave only the thin alumina ALD film suspended over the predefined well as displayed in Fig. 5.1c. After the graphene is etched away, the film is no longer visible in the optical microscope, and Raman spectroscopy was used to confirm the absence of graphene (Fig. 5.3).

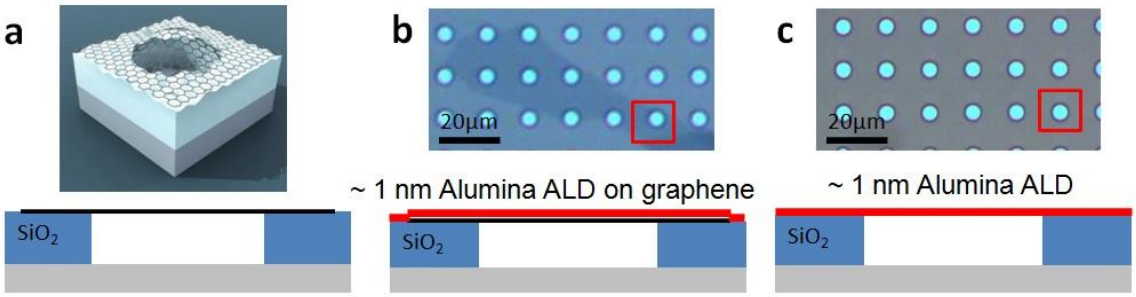

Fig. 5.1 (a) Schematic of a graphene membrane before atomic layer deposition (ALD). (b) (upper) Optical image of an exfoliated graphene flake with 7 cycles of alumina ALD. (lower) side view schematic of this graphene/ALD composite. (c) Optical image of a pure alumina film after graphene is etched away. (lower) side view schematic of this pure ALD film.

Image of cross-section for ALD/graphene composites is observed by TEM. Cross-sections of alumina/graphene devices on SiO_2 substrates were prepared using a focused ion beam lift-out. Before cross-sectioning, the samples were coated with ~20 nm of amorphous carbon followed by a thick platinum layer to protect the sample surfaces. The samples were imaged using a 200 kV electron beam in a FEI Technai-F-20 TEM/STEM. The composition of each layer was verified with electron energy-loss spectroscopy. TEM/STEM was used to image the alumina that was formed on graphene after 10 cycles of TMA/NO_2 nucleation treatment

followed by 5 cycles of TMA/H_2O ALD deposition. From these images, the observed alumina layer was amorphous and 2.8 ± 0.3 nm thick.

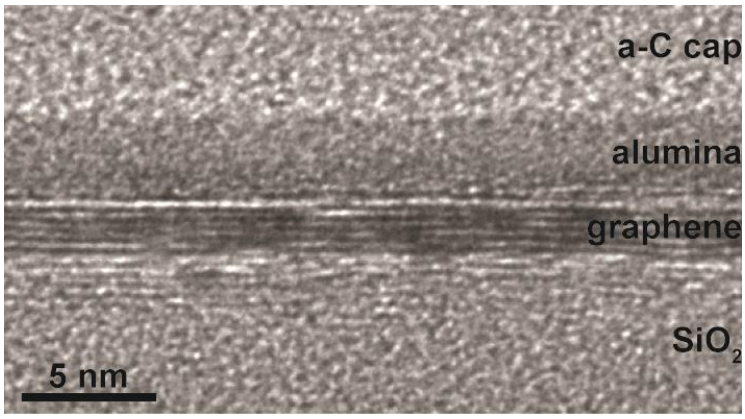

Fig. 5.2 Bright-field TEM image of a cross-section of supported alumina ALD film on 5-layer graphene supported on silicon oxide. The amorphous alumina layer is 2.8 ± 0.3 nm thick.

Raman spectroscopy was used to confirm the removal of graphene after etching.[29] Fig. 5.3 shows Raman spectroscopy of a graphene/ALD composite film before etching of graphene. The Raman spectrum shows the G and 2D peaks that are characteristic of a bilayer graphene membrane. After etching, the G and 2D peak are not detectable in the Raman spectrum confirming that all the graphene was etched away leaving only the suspended pure alumina ALD film.

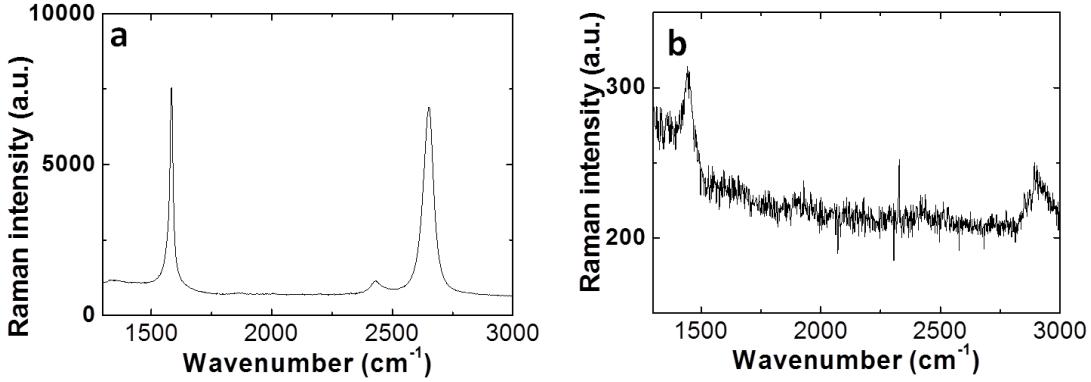

Fig. 5.3 (a) Raman spectrum for one of the graphene/ALD composite films in Fig. 3.1b. (b) A representative Raman spectrum on one of the pure alumina ALD films in Fig. 3.1C.

5.3 Young's Modulus of ALD Membranes

We have used blister test to get the Young's modulus of ALD membranes. A pressure difference is applied to the film using a previously reported method where slow diffusion through the SiO_2 substrate over-pressurizes the film-sealed microchamber.[8,79] An atomic force microscope (AFM) image of such an over-pressurized suspended film in Fig. 5.1c is shown in Fig. 5.4a. The ALD film is bulged upward with a maximum deflection through the center of the film, δ = 261 nm, and a radius, a = 2.76 μm, consistent with the radius of the predefined well. At increasing Δp, the film stretches further as δ increases as characterized in Fig. 5.4b. During AFM imaging, the bulge is stable suggesting a constant pressure difference and no significant leak rate of gas out of the microchamber, similar to previous results on graphene membranes[8]. This behavior implies that the aluminum oxide films are pinhole-free and impermeable to the nitrogen gas used for pressurization.

The deformation of the film follows:[79,182]

$$\Delta p = K(\nu)\frac{\delta^3}{a^4}Et \tag{5-1}$$

where E is Young's modulus, t is the thickness of the film, and K(υ) is a constant that depends on the Poisson's ratio. For the case of aluminum oxide, K(υ = 0.24) = 3.35.

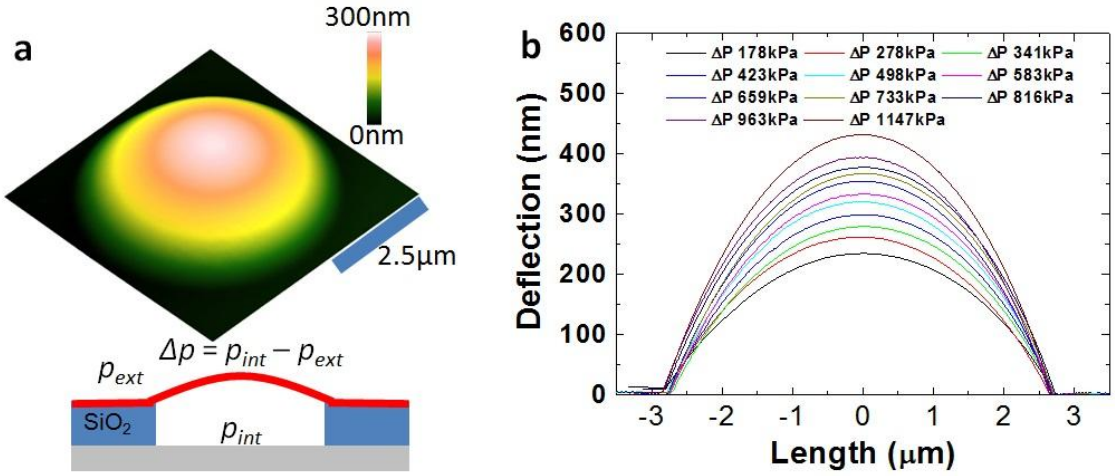

Fig. 5.4 (a) (upper) Atomic force microscope image of a pressurized 7 cycle pure alumina ALD film with Δp = 278 kPa. This film corresponds to the film boxed in red in Fig. 5.1 (b) and (c). (b) Deflection vs. position through the center of the film in (a) at different Δp.

Fig. 5.5 shows $K(\upsilon)\frac{\delta^3}{a^4}$vs. Δp for 18 pure alumina ALD films (graphene etched away) fabricated on an exfoliated graphene flake using 7 cycles of alumina ALD. The behavior of each film follows a line as expected from equation (5-1). The average and standard deviation of the slope of these lines gives Et = 250 ± 12 GPa-nm.

A method identical to one previously used to determine the elastic constants of pressurized graphene membranes was used to determine the elastic constants of the pure ALD films for a number of different films formed using 4 – 15 cycles.[8] Fig. 5.6 shows additional blister test data for the other pure ALD films fabricated and tested in this study. All of the films shown in one plot are from the same ALD coating on multiple graphene membrane supports. The *Et* values are extracted from the slopes.

The plot of *Et* vs. number of ALD cycles is shown in Fig. 5.7. A best fit line of the data gives a slope of Et_{cycle} = 16.9 ± 1.4 GPa – nm with an intercept of E_0t_0 = 127.1 ± 13.1 GPa – nm. This slope corresponds to $E_{ALD\ Al2O3}$= 154 ± 13 GPa assuming an ALD growth rate of 0.11

nm/cycle.[103,106] This Young's modulus is comparable to previous measurements on much thicker (tens to hundreds of nm) alumina ALD films that have Young's moduli of 168 – 220 GPa.[141,143,183] Because the films are freely suspended, a mechanical support does not influence the mechanical properties of the ALD thin films. The high Young's modulus is remarkable considering our samples are 2 – 3 orders of magnitude thinner than previously measured ALD films.

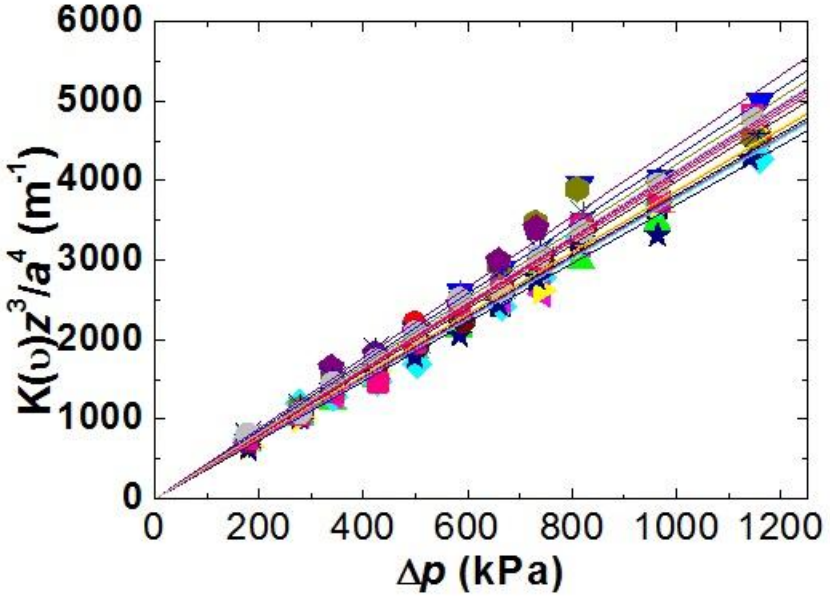

Fig. 5.5 $K(\nu)z^3/a^4$ versus Δp for 18 pure ALD films with 7 cycles of alumina ALD. Colored lines are best fits to each sample. The average and standard deviation of all the slopes corresponds to Et = 250 ± 12 GPa-nm.

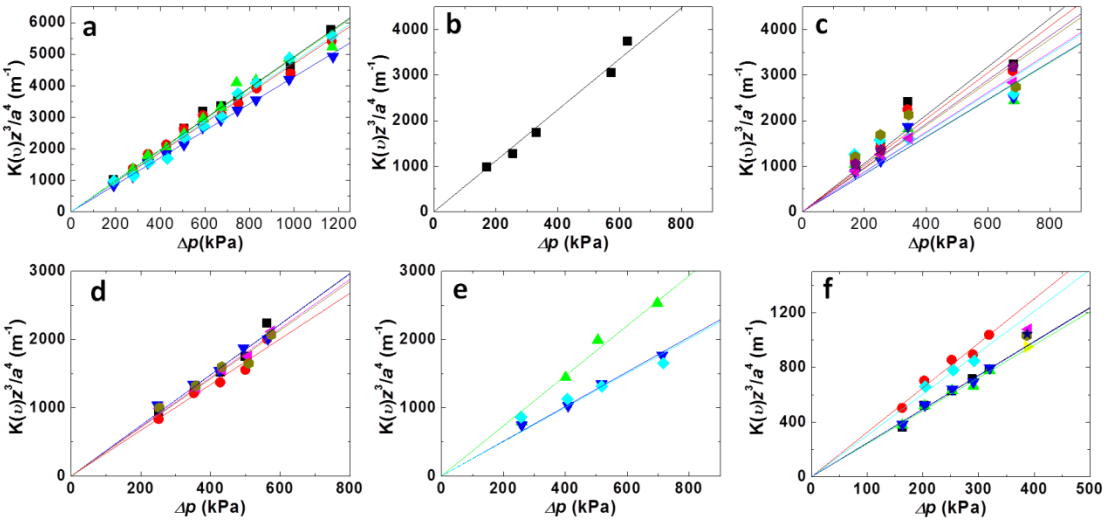

Fig. 5.6 $K(\nu)\delta^3/a^4$ versus Δp for (a) 5 pure ALD films with 8 cycles of alumina ALD. The average and standard deviation of all the slopes corresponds to Et = 213 ± 12 GPa-nm. (b) 1 pure ALD films with 5 cycles of alumina ALD. The slope is a best fit line and corresponds to Et = 180 ± 6 GPa-nm. (c) 8 pure ALD films with 5 cycles of alumina ALD. The average and standard deviation of all the slopes corresponds to Et = 219 ± 21 GPa-nm. (d) 5 pure ALD films with 8 cycles of alumina ALD. The average and standard deviation of all the slopes corresponds to Et = 280 ± 12 GPa-nm. (e) 3 pure ALD films with 10 cycles of alumina ALD. The average and standard deviation of all the slopes corresponds to Et = 355 ± 71 GPa-nm. (f) 9 pure ALD films with 15 cycles of alumina ALD. The average and standard deviation of all the slopes corresponds to Et = 375 ± 38 GPa-nm.

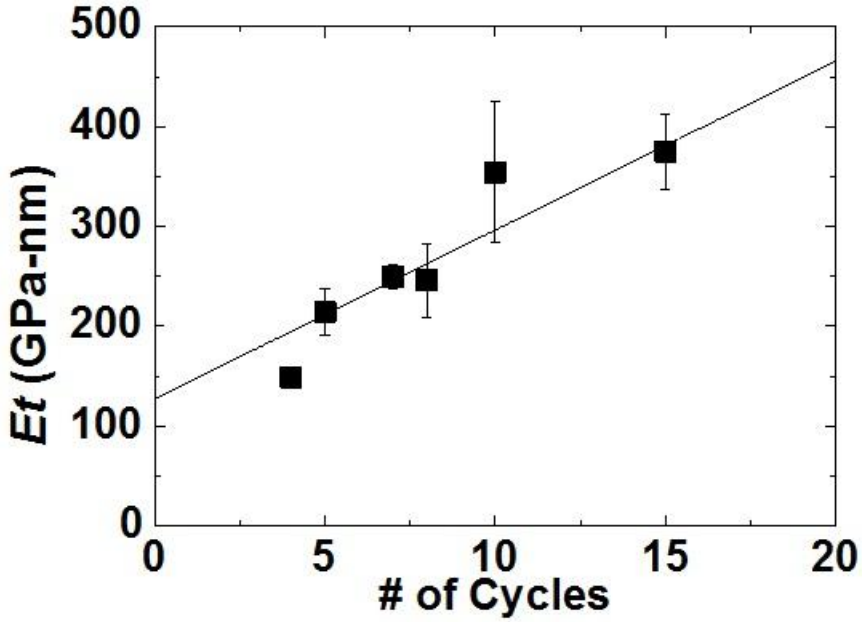

Fig. 5.7 Et vs. # of cycles for all the pure ALD films measured. The standard deviation is shown as error bars. The solid line is a best fit to the data and corresponds to Et_{cycle} = 16.9 ± 1.4 GPa – nm with an intercept of E_0t_0 = 127.1 ± 13.1 GPa – nm. This corresponds to $E_{ALD\ Al2O3}$ = 154 ± 13 GPa assuming a thickness gain per cycle of t_{cycle} = 0.11 nm.

5.4 Mass Density for ALD Membranes

The mass density can be calculated from the resonance method experiments. The pressure induced-strain in the film can be used to tune the mechanical resonance frequency of the suspended films. Fig. 5.8 demonstrates this behavior for a graphene/ALD composite film fabricated using 5 cycles of alumina ALD. The mechanical resonance is actuated and detected optically as previously reported.[8,87] We were unable to measure a resonance frequency for the pure alumina ALD films presumably due to the lack of optical reflectivity from these samples. The frequency first decreases and then increases as the film transitions from a bulged upward to a depressed downward state.

At sufficiently large pressures far from the minimum frequency, the frequency scales as $f^3 \alpha \Delta p$. The slope shows a dramatic decrease in frequency with the addition of alumina ALD cycles as shown in Fig. 5.9. The pressure inside of the microcavity in Fig. 5.9 is much lower than the inside pressure in Fig. 5.8, which makes the y-intercept at p_{ext}=0 much lower. This behavior can be explained by the pressure-induced changes in the tension in a stretched circular film according to:

$$f^3 = 7\times10^{-3}\sqrt{\frac{\mathrm{K}(\upsilon)Et}{a^4\rho_A{}^3}}\Delta p \qquad (5\text{-}2)$$

where ρ_A is the mass per unit area. From the slope of the lines in Fig. 5.9 and using $\mathrm{K}(\upsilon)Et$ determined by a pressurized blister test on the composite ALD/graphene film, we can determine ρ_A of each suspended film before and after each ALD process. All samples showed an increase in ρ_A with number of alumina ALD cycles as displayed in Fig. 5.10a. The first three cycles showed a larger increase in ρ_A that may be related to the initial nucleation of alumina ALD. The finite ρ_A before any ALD cycles is attributed to the additional mass from the adhesion layer.

Using the measured ρ_A, we can estimate the volume density of the ALD films, ρ_V, and the areal mass density of the adhesion layer from pretreatment, ρ_{A_ad}. Because all the samples have an adhesion layer with an unknown ρ_{A_ad}, we first determine ρ_V from the slope of the lines in Fig. 5.10a for coatings after the nucleation treatment. This determination yields $\rho_V = 2.3 \pm 0.4$ g/cm^3 assuming an ALD growth rate of 0.11 nm/cycle.[103] (The anomalously large value at 12 cycles shown in blue was not used in calculating this average and standard deviation.) We then deduce ρ_{A_ad} from the measured ρ_A using $\rho_{A\_ad} = \rho_A - \rho_V * N$, where N is the number of alumina ALD cycles. This derivation yields an average value and standard deviation of $\rho_{A\_ad} = 1.4 \pm 0.3 * 10^{-7}$ g/cm^2. We can then determine ρ_V for every ALD film in Fig. 5.10a. This procedure yields $\rho_V = 2.4 \pm 0.7$ g/cm^3 as shown in Fig. 5.10b. This density is comparable within experimental error to previous densities measured on thicker alumina ALD thin films of 3.0 g/cm.[3 105]

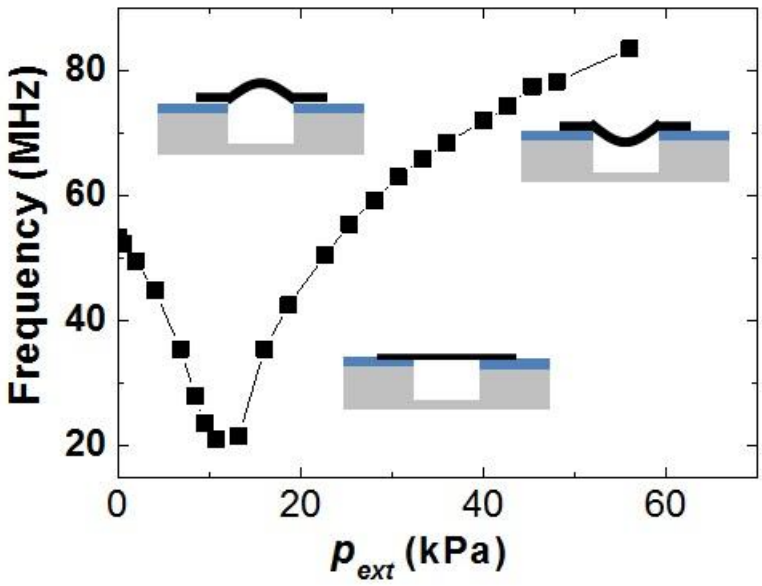

Fig. 5.8 Mechanical resonant frequency vs. p_{ext} for a graphene /ALD composite film with 5 cycles of alumina ALD. (insets) Schematic of the film at different Δp.

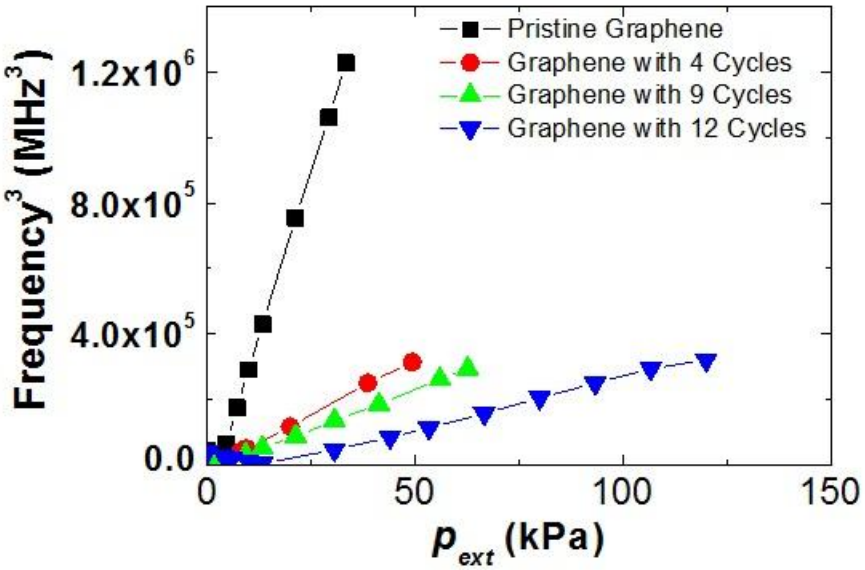

Fig. 5.9 Frequency^3 vs. p_{ext} for a single graphene/ALD composite film with 0, 4, 9, 12 cycles of alumina ALD.

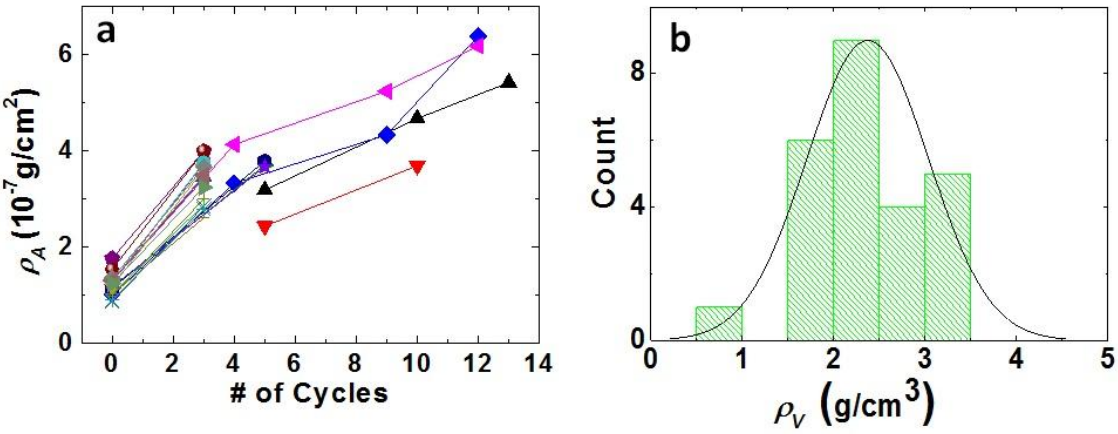

Fig. 5.10 (a) Areal mass density ρ_A vs. number of cycles for all the graphene/ALD composites measured. (b) Histogram of volume mass density ρ_V for the alumina ALD films. The black line is a Gaussian fit to the data.

5.5 Initial Tension in Graphene and Graphene/ALD Composite Films

Even with no applied pressure difference across the films, the frequency of these nanomechanical resonators still behave as stretched membranes.[79] This is illustrated by the high resonant frequencies exhibited by the membranes even when no pressure difference exists across

the membranes or $p_{int} = p_{ext}$. Neglecting the bending rigidity, the fundamental frequency of a clamped circular membrane under uniform tension, S_0, is given by:

$$f_0 = \frac{2.404}{2\pi} \cdot \sqrt{\frac{S_0}{ma^2}} \tag{5-3}$$

The initial surface tension in the membranes can be deduced by measuring the resonant frequency of the membranes when no pressure difference exists across the membrane. For the graphene membrane resonator before ALD deposition, this corresponds to a uniform tension of $S_0 = 0.073 \pm 0.041$ N/m (Fig. 5.11a). After ALD film deposition, the uniform tension is $S_0 = 0.21 \pm 0.13$ N/m (Fig. 5.11b). This increase in uniform tension indicates that there is a significant increase in the intrinsic stress in the membranes. Future work will seek to understand the origin of this increased tension in the composite membranes to determine whether this intrinsic stress is a result of stress in the pure ALD films or arises from the composite nature of the films.

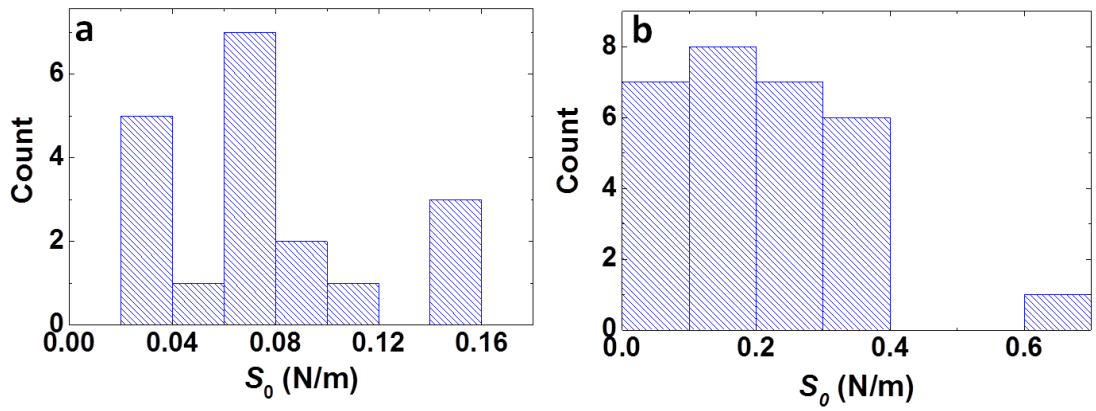

Fig. 5.11 Histogram of initial tension in (a) pristine graphene membranes and (b) graphene/ALD composite membranes.

5.6 Pure ALD Films from the Nucleation Treatment

The thinnest suspended pure alumina ALD film fabricated is shown in Fig. 5.12. This film had only 4 cycles of the NO_2/TMA nucleation treatment applied to the graphene. Subsequent etching of the graphene support leaves a continuous and smooth film. The film has a few small voids visible by AFM. Fig. 5.13 shows optical and AFM images for a film made from only 5 cycles of the NO_2/TMA nucleation treatment. This film is also continuous and smooth and there are no pinholes or small voids visible by AFM.

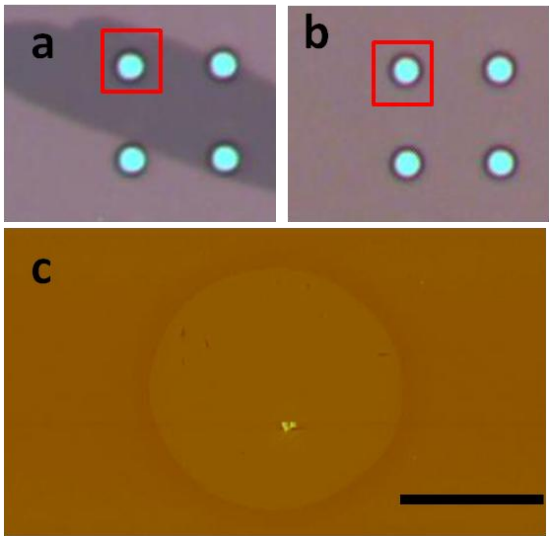

Fig. 5.12 (a) Optical image of a graphene flake with 4 cycles of NO_2/TMA. (b) Optical image after etching away the graphene (c) Atomic force microscope image corresponding to the red box in (b) of the pure alumina ALD film (scale bar = 2.5 μm).

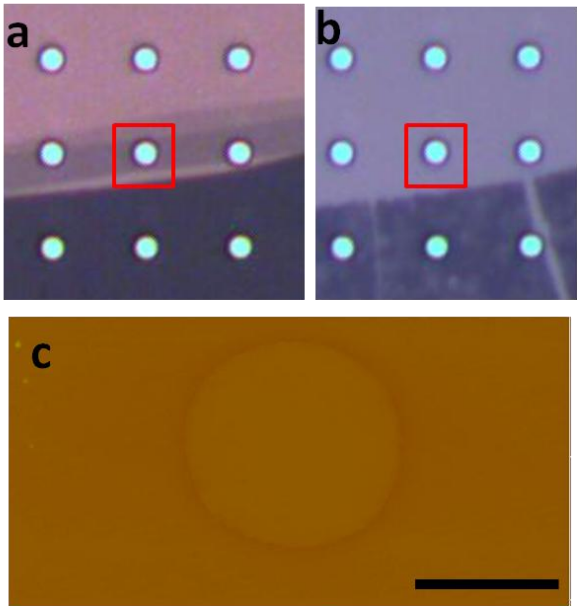

Fig. 5.13 (a) Optical image of a graphene flake with 5 cycles of NO_2/TMA. (b) Optical image after etching away the graphene (c) Atomic force microscope image corresponding to the red box in (b) of the pure alumina ALD film (scale bar = 2.5 μm).

5.7 Yield Rate

None of the 178 samples fabricated with less than 4 alumina ALD cycles were impermeable to N_2 gas after removal of the graphene as shown in Fig. 5.14a. However, the yield of impermeable films increased with number of ALD cycles and reached 85% for 15 ALD cycles as displayed in Fig. 5.14b. This behavior indicates that increasing the number of ALD cycles reduces pinholes or gas diffusion through the film (The cycles here is the coating after pretreatment).

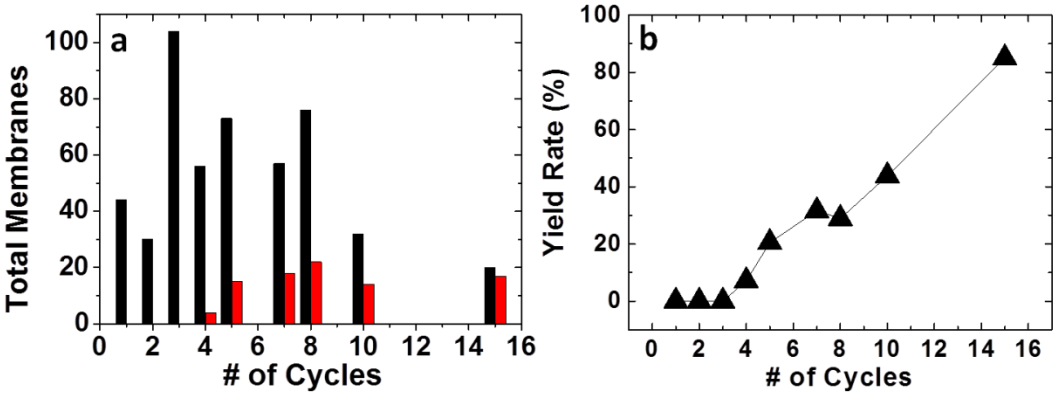

Fig. 5.14 (a) (black) Number of all pure ALD films fabricated in this study vs. number of ALD coating cycles. (red) Number of pure ALD films that hold N_2 gas from that sample batch (b) Percentage yield vs. # of cycles for all the pure ALD films fabricated.

For freely suspended films formed using only 5 cycles of the TMA/NO_2 nucleation treatment, AFM images of the films do not show voids (Fig. 5.13). This corroborates our measurements of a contribution from the adhesion layer to E and ρ_{A_funct} in Fig. 5.7 and Fig. 5.10a. Future work will examine the dependence of the adhesion layer and its role in nucleating continuous pinhole-free ALD alumina thin film growth on graphene.

5.8 Conclusions

In conclusion, a new class of ultrathin films has been created based on aluminum oxide ALD on graphene. These films are mechanically robust, pinhole-free, and have ~nm thicknesses while still maintaining a Young's modulus comparable to their much thicker counterparts. The manufacturability, thickness control, and versatility of the ALD process means that materials and processing can be tailored to suit many applications where traditional silicon or graphene-based thin film mechanical devices fail to offer the needed functionality.[184,185] Furthermore, these films can be integrated with graphene or other nanomechanical structures to create multifunctional quasi-2D electromechanical structures.

Chapter 6 Summary and Suggestions for Future Work

6.1 Summary

This thesis summarized a careful study for the gas transport mechanisms of graphene membrane, which can be used in gas separation. What's more, it looked into details of mechanical properties of ultrathin suspended ALD films, which may be used for gas separation. Chapter 1-3 overviewed the basic concepts and background, which underlie my research; chapter 4-5 provided the results and discussion of the key findings.

Chapter 1 began with fundamentals of graphnene. Then nanopores on graphene was introduced in detail. Chapter 2 focused on nanomechanics, which started from the solid state mechanics and dynamics for NEMS. Then it introduced the mechanical properties of graphene in detail. Chapter 3 gave the basics of ALD and the mechanical properties of Al_2O_3 ALD.

We created single pore valves from porous graphene membrane to control gas flux in Chapter 4. In this part, sub-nm pores were introduced to the pristine graphene with UV exposure. A blister test was used to check the leak rate. Controlling the pore opening and closing using AuNC dramatically changed gas permeance. We detected the stochastic switching of permeance on single layer graphene membrane, which is believed to arise from the minor atomic rearrangements around the pore mouth. The permeance of polar gas molecules were observed to be much higher than the kinetic theory's prediction.

Chapter 5 provided a method to fabricate ~nm thin suspended pure ALD Al_2O_3 films. ALD Al_2O_3 was deposited on graphene membranes; then graphene was etched away by oxidation in furnace at 600 ℃. No visible voids can be found on ALD films even with just with 5

cycles of pretreatment. As the cycles of coating increase, the percentage of membranes, which can hold gas, increases. From the blister test, we found that the Young's modulus for ALD Al_2O_3 is around 154GPa, which is comparable to previous measurements on much thicker alumina ALD films. From the resonance test, we calculated the mass density is ~2.4 g/cm^3, which is comparable to previous densities measured on thicker alumina ALD thin films.

6.2 Suggestions for Future Work

The preliminary study of single pore on graphene membrane opens a door to a new field. We can tune the temperature to see the response of the quantized switching. Different functionalized methods can be tried to modify the permeance switching. Different kinds of nano blockers can be used on 2D porous materials to create controllable switching. These experiments can be extended to ion separation, and water desalination too. Besides the experimental work, systematic analysis may be needed from theorists.

Some in-depth study of ALD ultrathin films is also interesting. AFM nanoindentation can be used to check its breaking strength. NEMS resonators can be created from pure ALD films. Blister test or other methods can be used to check its permeance. Since it is easy to scale up with the uniform coated ALD technique, ALD ultrathin film for gas or ion separation is also attractive. Moreover, ALD healed porous graphene may lead to some promising results. Recently, extremely high flux is achieved from porous graphene with high density pore arrays (7.6-nm pore diameter with 4.0% porosity), but the selectivity is less than 10 for H_2/CO_2.[186] If we can use

ALD technique to heal the 7.6nm pore to sub-nm, molecular sieving may be achieved. In this case, both large flux and high selectivity may be accomplished at the same time.

Reference

1 Landau, L. D. Theorie der phasenumwandlungen II. *Phys. Z. Sowjetunion* **11**, 26-35 (1937).

2 Landau, L. D. & Lifshitz, E. M. *Statistical Physics, Part I*. (1980).

3 Mermin, N. D. Crystalline order in two dimensions. *Phys. Rev.* **176**, 250-254 (1968).

4 Peierls, R. E. Quelques proprietes typiques des corpses solides. *Ann. I. H. Poincare* **5**, 177-222 (1935).

5 Venables, J. A., Spiller, G. D. T. & Hanbucken, M. Nucleation and Growth of Thin-Films. *Rep Prog Phys* **47**, 399-459, doi:Doi 10.1088/0034-4885/47/4/002 (1984).

6 Novoselov, K. S. *et al.* Electric field effect in atomically thin carbon films. *Science* **306**, 666-669, doi:DOI 10.1126/science.1102896 (2004).

7 Lee, C., Wei, X. D., Kysar, J. W. & Hone, J. Measurement of the elastic properties and intrinsic strength of monolayer graphene. *Science* **321**, 385-388, doi:DOI 10.1126/science.1157996 (2008).

8 Bunch, J. S. *et al.* Impermeable Atomic Membranes from Graphene Sheets. *Nano Letters* **8**, 2458-2462, doi:10.1021/nl801457b (2008).

9 Jiang, D. E., Cooper, V. R. & Dai, S. Porous Graphene as the Ultimate Membrane for Gas Separation. *Nano Lett* **9**, 4019-4024, doi:Doi 10.1021/Nl9021946 (2009).

10 Stolyarova, E. *et al.* High-resolution scanning tunneling microscopy imaging of mesoscopic graphene sheets on an insulating surface. *Proceedings of the National Academy of Sciences* **104**, 9209-9212, doi:10.1073/pnas.0703337104 (2007).

11 Novoselov, K. S. Beyond the wonder material. *Physics World* **22**, 27-30 (2009).

12 Geim, A. K. Graphene: Status and Prospects. *Science* **324**, 1530-1534 (2009).

13 Koenig, S. P., Boddeti, N. G., Dunn, M. L. & Bunch, J. S. Ultrastrong adhesion of graphene membranes. *Nat Nano* **6**, 543-546 (2011).

14 Balandin, A. A. *et al.* Superior thermal conductivity of single-layer graphene. *Nano Letters* **8**, 902-907 (2008).

15 Yoon, D., Son, Y. W. & Cheong, H. Negative Thermal Expansion Coefficient of Graphene Measured by Raman Spectroscopy. *Nano Letters* **11**, 3227-3231, doi:Doi 10.1021/Nl201488g (2011).

16 Novoselov, K. S. *et al.* Room-temperature quantum hall effect in graphene. *Science* **315**, 1379-1379, doi:DOI 10.1126/science.1137201 (2007).

17 Novoselov, K. S. *et al.* Two-dimensional gas of massless Dirac fermions in graphene. *Nature* **438**, 197-200, doi:Doi 10.1038/Nature04233 (2005).

18 Zhang, Y., Tan, Y.-W., Stormer, H. L. & Kim, P. Experimental observation of the quantum Hall effect and Berry's phase in graphene. *Nature* **438**, 201-204 (2005).

19 Nair, R. R. *et al.* Fine structure constant defines visual transparency of graphene. *Science* **320**, 1308-1308, doi:DOI 10.1126/science.1156965 (2008).

20 Riedl, C., Coletti, C., Iwasaki, T., Zakharov, A. A. & Starke, U. Quasi-Free-Standing Epitaxial Graphene on SiC Obtained by Hydrogen Intercalation. *Phys Rev Lett* **103** (2009).

21 Berger, C. *et al.* Electronic confinement and coherence in patterned epitaxial graphene. *Science* **312**, 1191-1196, doi:DOI 10.1126/science.1125925 (2006).
22 Kim, K. S. *et al.* Large-scale pattern growth of graphene films for stretchable transparent electrodes. *Nature* **457**, 706-710, doi:Doi 10.1038/Nature07719 (2009).
23 Li, X. S. *et al.* Large-Area Synthesis of High-Quality and Uniform Graphene Films on Copper Foils. *Science* **324**, 1312-1314, doi:DOI 10.1126/science.1171245 (2009).
24 Li, X. S. *et al.* Large-Area Graphene Single Crystals Grown by Low-Pressure Chemical Vapor Deposition of Methane on Copper. *Journal of the American Chemical Society* **133**, 2816-2819 (2011).
25 Geim, A. K. & Grigorieva, I. V. Van der Waals heterostructures. *Nature* **499**, 419-425, doi:Doi 10.1038/Nature12385 (2013).
26 Wilson, J. A. & Yoffe, A. D. The transition metal dichalcogenides discussion and interpretation of the observed optical, electrical and structural properties. *Advances in Physics* **18**, 193-335, doi:10.1080/00018736900101307 (1969).
27 Splendiani, A. *et al.* Emerging Photoluminescence in Monolayer MoS2. *Nano Letters* **10**, 1271-1275, doi:Doi 10.1021/Nl903868w (2010).
28 Mak, K. F., Lee, C., Hone, J., Shan, J. & Heinz, T. F. Atomically Thin MoS2: A New Direct-Gap Semiconductor. *Phys Rev Lett* **105**, doi:Doi 10.1103/Physrevlett.105.136805 (2010).
29 Novoselov, K. S. *et al.* Two-dimensional atomic crystals. *Proceedings of the National Academy of Sciences of the United States of America* **102**, 10451-10453, doi:DOI 10.1073/pnas.0502848102 (2005).
30 Castellanos-Gomez, A. *et al.* Laser-Thinning of MoS2: On Demand Generation of a Single-Layer Semiconductor. *Nano Letters* **12**, 3187-3192, doi:Doi 10.1021/Nl301164v (2012).
31 Coleman, J. N. *et al.* Two-Dimensional Nanosheets Produced by Liquid Exfoliation of Layered Materials. *Science* **331**, 568-571 (2011).
32 Nagashima, A., Tejima, N., Gamou, Y., Kawai, T. & Oshima, C. Electronic Dispersion-Relations of Monolayer Hexagonal Boron-Nitride Formed on the Ni(111) Surface. *Phys Rev B* **51**, 4606-4613, doi:DOI 10.1103/PhysRevB.51.4606 (1995).
33 Novoselov, K. S. & Neto, A. H. C. Two-dimensional crystals-based heterostructures: materials with tailored properties. *Phys Scripta* **T146**, doi:Doi 10.1088/0031-8949/2012/T146/014006 (2012).
34 Bonaccorso, F. *et al.* Production and processing of graphene and 2d crystals. *Mater Today* **15**, 564-589 (2012).
35 Venkatesan, B. M. & Bashir, R. Nanopore sensors for nucleic acid analysis. *Nat Nanotechnol* **6**, 615-624, doi:Doi 10.1038/Nnano.2011.129 (2011).
36 Miles, B. N. *et al.* Single molecule sensing with solid-state nanopores: novel materials, methods, and applications. *Chem Soc Rev* **42**, 15-28, doi:Doi 10.1039/C2cs35286a (2013).
37 Wanunu, M. *et al.* Rapid electronic detection of probe-specific microRNAs using thin nanopore sensors. *Nat Nanotechnol* **5**, 807-814, doi:Doi 10.1038/Nnano.2010.202 (2010).
38 Dekker, C. Solid-state nanopores. *Nat Nanotechnol* **2**, 209-215, doi:DOI 10.1038/nnano.2007.27 (2007).
39 Faller, M., Niederweis, M. & Schulz, G. E. The structure of a mycobacterial outer-membrane channel. *Science* **303**, 1189-1192, doi:DOI 10.1126/science.1094114 (2004).
40 Garaj, S. *et al.* Graphene as a subnanometre trans-electrode membrane. *Nature* **467**, 190-U173, doi:Doi 10.1038/Nature09379 (2010).
41 Hall, J. E. Access Resistance of a Small Circular Pore. *J Gen Physiol* **66**, 531-532, doi:Doi 10.1085/Jgp.66.4.531 (1975).

42 Li, J. *et al.* Ion-beam sculpting at nanometre length scales. *Nature* **412**, 166-169, doi:Doi 10.1038/35084037 (2001).
43 Storm, A. J., Chen, J. H., Ling, X. S., Zandbergen, H. W. & Dekker, C. Fabrication of solid-state nanopores with single-nanometre precision. *Nat Mater* **2**, 537-540, doi:Doi 10.1038/Nmat941 (2003).
44 Merchant, C. A. *et al.* DNA Translocation through Graphene Nanopores. *Nano Lett* **10**, 2915-2921, doi:Doi 10.1021/Nl101046t (2010).
45 Gierak, J. *et al.* Sub-5 nm FIB direct patterning of nanodevices. *Microelectron Eng* **84**, 779-783, doi:DOI 10.1016/j.mee.2007.01.059 (2007).
46 Yang, J. J. *et al.* Rapid and precise scanning helium ion microscope milling of solid-state nanopores for biomolecule detection. *Nanotechnology* **22**, doi:Doi 10.1088/0957-4484/22/28/285310 (2011).
47 Ayub, M. *et al.* Precise electrochemical fabrication of sub-20 nm solid-state nanopores for single-molecule biosensing. *J Phys-Condens Mat* **22**, doi:Doi 10.1088/0953-8984/22/45/454128 (2010).
48 Nilsson, J., Lee, J. R. I., Ratto, T. V. & Letant, S. E. Localized functionalization of single nanopores. *Adv Mater* **18**, 427-+, doi:DOI 10.1002/adma.200501991 (2006).
49 Danelon, C., Santschi, C., Brugger, J. & Vogel, H. Fabrication and functionalization of nanochannels by electron-beam-induced silicon oxide deposition. *Langmuir* **22**, 10711-10715, doi:Doi 10.1021/La061321c (2006).
50 Koenig, S. P., Wang, L. D., Pellegrino, J. & Bunch, J. S. Selective molecular sieving through porous graphene. *Nat Nanotechnol* **7**, 728-732, doi:Doi 10.1038/Nnano.2012.162 (2012).
51 *Maxwell–Boltzmann distribution*, <http://en.wikipedia.org/wiki/Maxwell%E2%80%93Boltzmann_distribution> (
52 Reif, F. *Fundamentals of Statistical and Thermal Physics*. (McGraw-Hill Inc., 1965).
53 Gombosi, T. I. *Gaskinetic theory*. (Cambridge Unversity Press, 1994).
54 Baker, R. W. *Membrane Technology and Applications*. (John Wiley & Sons Ltd, 2004).
55 Behling, R. D., Ohlrogge, K., Peinemann, K.-V. & Kyburz, E. The Separation of Hydrocarbons from Waste Vapor Streams. (1989).
56 Pandey, P. & Chauhan, R. S. Membranes for gas separation. *Prog Polym Sci* **26**, 853-893, doi:Doi 10.1016/S0079-6700(01)00009-0 (2001).
57 Barrer, R. M. Diffusion in Porous Media. *Appl. Mater. Res.* **2** (1963).
58 Hassan, M. H., Way, J. D., Thoen, P. M. & Dillon, A. C. Single-Component and Mixed-Gas Transport in a Silica Hollow-Fiber Membrane. *J Membrane Sci* **104**, 27-42, doi:Doi 10.1016/0376-7388(95)00009-2 (1995).
59 Keizer, K., Burggraaf, A. J., Vroon, Z. A. E. P. & Verweij, H. Two component permeation through thin zeolite MFI membranes. *J Membrane Sci* **147**, 159-172, doi:Doi 10.1016/S0376-7388(98)00133-1 (1998).
60 Ash, R., Barrer, R. M. & Pope, C. G. Flow of Adsorbable Gases and Vapours in a Microporous Medium .2. Binary Mixtures. *Proc R Soc Lon Ser-A* **271**, 19-+, doi:DOI 10.1098/rspa.1963.0002 (1963).
61 Drahushuk, L. W. & Strano, M. S. Mechanisms of Gas Permeation through Single Layer Graphene Membranes. *Langmuir* **28**, 16671-16678, doi:Doi 10.1021/La303468r (2012).
62 Liu, H., Chen, Z., Dai, S. & Jiang, D.-e. Selectivity trend of gas separation through nanoporous graphene. *Journal of Solid State Chemistry*, doi:http://dx.doi.org/10.1016/j.jssc.2014.01.030 (2014).
63 Sun, C. *et al.* Mechanisms of Molecular Permeation through Nanoporous Graphene Membranes. *Langmuir* **30**, 675-682, doi:10.1021/la403969g (2013).

64 Plimpton, S. Fast Parallel Algorithms for Short-Range Molecular-Dynamics. *J Comput Phys* **117**, 1-19, doi:DOI 10.1006/jcph.1995.1039 (1995).
65 Bonomi, M. *et al.* PLUMED: A portable plugin for free-energy calculations with molecular dynamics. *Comput Phys Commun* **180**, 1961-1972, doi:DOI 10.1016/j.cpc.2009.05.011 (2009).
66 Girit, C. O. *et al.* Graphene at the Edge: Stability and Dynamics. *Science* **323**, 1705-1708, doi:DOI 10.1126/science.1166999 (2009).
67 Zan, R., Bangert, U., Ramasse, Q. & Novoselov, K. S. Metal-Graphene Interaction Studied via Atomic Resolution Scanning Transmission Electron Microscopy. *Nano Lett* **11**, 1087-1092, doi:Doi 10.1021/Nl103980h (2011).
68 Amft, M., Sanyal, B., Eriksson, O. & Skorodumova, N. V. Small gold clusters on graphene, their mobility and clustering: a DFT study. *J Phys-Condens Mat* **23**, doi:Doi 10.1088/0953-8984/23/20/205301 (2011).
69 Hardcastle, T. P. *et al.* Mobile metal adatoms on single layer, bilayer, and trilayer graphene: An ab initio DFT study with van der Waals corrections correlated with electron microscopy data. *Phys Rev B* **87**, doi:Doi 10.1103/Physrevb.87.195430 (2013).
70 Liu, L. *et al.* Slow Gold Adatom Diffusion on Graphene: Effect of Silicon Dioxide and Hexagonal Boron Nitride Substrates. *J Phys Chem B* **117**, 4305-4312, doi:Doi 10.1021/Jp305521g (2013).
71 Wang, H. T. *et al.* Interaction between single gold atom and the graphene edge: A study via aberration-corrected transmission electron microscopy. *Nanoscale* **4**, 2920-2925, doi:Doi 10.1039/C2nr00059h (2012).
72 Roukes, M. Nanoelectromechanical systems face the future. *Physics World* **14**, 25-31 (2001).
73 Naik, A. K., Hanay, M. S., Hiebert, W. K., Feng, X. L. & Roukes, M. L. Towards single-molecule nanomechanical mass spectrometry. *Nat Nanotechnol* **4**, 445-450, doi:Doi 10.1038/Nnano.2009.152 (2009).
74 Yang, Y. T., Callegari, C., Feng, X. L. & Roukes, M. L. Surface Adsorbate Fluctuations and Noise in Nanoelectromechanical Systems. *Nano Letters* **11**, 1753-1759, doi:Doi 10.1021/Nl2003158 (2011).
75 Jensen, K., Kim, K. & Zettl, A. An atomic-resolution nanomechanical mass sensor. *Nat Nanotechnol* **3**, 533-537, doi:DOI 10.1038/nnano.2008.200 (2008).
76 Fung, Y. C. & Tong, P. *Classical and Computational Solid Mechanics*. (World Scientific Publishing Co. Pte. Ltd., 2001).
77 Nix, W. D. *Lecture Notes for "Mechanical Properties of Thin Films"*. (2005).
78 Hencky, H. Uber den spannungzustand in kreisrunden platten mit verschwindender biegungssteiflgeit. *Z. fur Mathematik und Physik* **63**, 311-317 (1915).
79 Koenig, S. P., Boddeti, N. G., Dunn, M. L. & Bunch, J. S. Ultrastrong adhesion of graphene membranes. *Nat Nanotechnol* **6**, 543-546 (2011).
80 King, G. C. *Vibrations and Waves*. (John Wiley & Sons Ltd, 2009).
81 Huang, X. M. H., Feng, X. L., Zorman, C. A., Mehregany, M. & Roukes, M. L. VHF, UHF and microwave frequency nanomechanical resonators. *New J Phys* **7** (2005).
82 Timoshenko, S., Young, D. H. & Weaver, W. *Vibration Problems in Engineering*. (John Wiley & Sons, Inc., 1974).
83 Chiu, H. Y., Hung, P., Postma, H. W. C. & Bockrath, M. Atomic-Scale Mass Sensing Using Carbon Nanotube Resonators. *Nano Letters* **8**, 4342-4346, doi:Doi 10.1021/Nl802181c (2008).
84 Hagedorn, P. & DasGupta, A. *Vibrations and Waves in Continuous Mechanical Systems*. (John Wiley & Sons Ltd, 2007).
85 Arlett, J. L., Myers, E. B. & Roukes, M. L. Comparative advantages of mechanical biosensors. *Nat Nanotechnol* **6**, 203-215, doi:DOI 10.1038/nnano.2011.44 (2011).

86 Barton, R. A. *et al.* High, Size-Dependent Quality Factor in an Array of Graphene Mechanical Resonators. *Nano Lett* **11**, 1232-1236, doi:Doi 10.1021/Nl1042227 (2011).
87 Bunch, J. S. *et al.* Electromechanical resonators from graphene sheets. *Science* **315**, 490-493, doi:DOI 10.1126/science.1136836 (2007).
88 van der Zande, A. M. *et al.* Large-Scale Arrays of Single-Layer Graphene Resonators. *Nano Lett* **10**, 4869-4873, doi:Doi 10.1021/Nl102713c (2010).
89 Saleh, B. E. A. & Teich, M. C. *Fundamentals of Photonics*. (John Wiley & Sons, Inc., 2007).
90 Bunch, J. S. *Mechanical and Electrical Properties of Graphene Sheets* ph. D. thesis, Cornell University, (2008).
91 Bunch, J. S. *Mechanical and electrical properties of graphene sheets* Ph.D thesis, Cornell University, (2008).
92 Ritala, M. *et al.* Perfectly conformal TiN and Al2O3 films deposited by atomic layer deposition. *Chem Vapor Depos* **5**, 7-9, doi:Doi 10.1002/(Sici)1521-3862(199901)5:1<7::Aid-Cvde7>3.0.Co;2-J (1999).
93 Paranjpe, A., Gopinath, S., Omstead, T. & Bubber, R. Atomic layer deposition of AlOx for thin film head gap applications. *Journal of the Electrochemical Society* **148**, G465-G471, doi:Doi 10.1149/1.1385822 (2001).
94 Chatham, H. Oxygen diffusion barrier properties of transparent oxide coatings on polymeric substrates. *Surf Coat Tech* **78**, 1-9 (1996).
95 George, S. M. Atomic Layer Deposition: An Overview. *Chem Rev* **110**, 111-131, doi:Doi 10.1021/Cr900056b (2010).
96 Miikkulainen, V., Leskela, M., Ritala, M. & Puurunen, R. L. Crystallinity of inorganic films grown by atomic layer deposition: Overview and general trends. *J Appl Phys* **113**, doi:Doi 10.1063/1.4757907 (2013).
97 Puurunen, R. L. Surface chemistry of atomic layer deposition: A case study for the trimethylaluminum/water process. *J Appl Phys* **97**, doi:Doi 10.1063/1.1940727 (2005).
98 Puurunen, R. L. Growth per cycle in atomic layer deposition: A theoretical model. *Chem Vapor Depos* **9**, 249-257, doi:DOI 10.1002/cvde.200306265 (2003).
99 Higashi, G. S. & Fleming, C. G. Sequential Surface Chemical-Reaction Limited Growth of High-Quality Al2o3 Dielectrics. *Appl Phys Lett* **55**, 1963-1965, doi:Doi 10.1063/1.102337 (1989).
100 Soto, C. & Tysoe, W. T. The Reaction Pathway for the Growth of Alumina on High Surface-Area Alumina and in Ultrahigh-Vacuum by a Reaction between Trimethyl Aluminum and Water. *J Vac Sci Technol A* **9**, 2686-2695 (1991).
101 Goldstein, D. N., McCormick, J. A. & George, S. M. Al(2)O(3) Atomic Layer Deposition with Trimethylaluminum and Ozone Studied by in Situ Transmission FTIR Spectroscopy and Quadrupole Mass Spectrometry. *J Phys Chem C* **112**, 19530-19539, doi:Doi 10.1021/Jp804296a (2008).
102 Kim, J. B. *et al.* Improvement in Al2O3 dielectric behavior by using ozone as an oxidant for the atomic layer deposition technique. *Journal of Applied Physics* **92**, 6739-6742 (2002).
103 Ott, A. W., Klaus, J. W., Johnson, J. M. & George, S. M. Al3O3 thin film growth on Si(100) using binary reaction sequence chemistry. *Thin Solid Films* **292**, 135-144, doi:Doi 10.1016/S0040-6090(96)08934-1 (1997).
104 Elam, J. W., Groner, M. D. & George, S. M. Viscous flow reactor with quartz crystal microbalance for thin film growth by atomic layer deposition. *Review of Scientific Instruments* **73**, 2981-2987 (2002).
105 Groner, M. D., Fabreguette, F. H., Elam, J. W. & George, S. M. Low-temperature Al2O3 atomic layer deposition. *Chemistry of Materials* **16**, 639-645 (2004).

106 Ott, A. W., McCarley, K. C., Klaus, J. W., Way, J. D. & George, S. M. Atomic layer controlled deposition of Al2O3 films using binary reaction sequence chemistry. *Appl Surf Sci* **107**, 128-136, doi:Doi 10.1016/S0169-4332(96)00503-X (1996).
107 Groner, M. D., Elam, J. W., Fabreguette, F. H. & George, S. M. Electrical characterization of thin Al2O3 films grown by atomic layer deposition on silicon and various metal substrates. *Thin Solid Films* **413**, 186-197, doi:Doi 10.1016/S0040-6090(02)00438-8 (2002).
108 Jensen, J. M. *et al.* X-ray reflectivity characterization of ZnO/Al2O3 multilayers prepared by atomic layer deposition. *Chem Mater* **14**, 2276-2282, doi:Doi 10.1021/Cm011587z (2002).
109 Kuse, R., Kundu, M., Yasuda, T., Miyata, N. & Toriumi, A. Effect of precursor concentration in atomic layer deposition of Al2O3. *J Appl Phys* **94**, 6411-6416, doi:Doi 10.1063/1.1618918 (2003).
110 Matero, R., Rahtu, A., Ritala, M., Leskela, M. & Sajavaara, T. Effect of water dose on the atomic layer deposition rate of oxide thin films. *Thin Solid Films* **368**, 1-7, doi:Doi 10.1016/S0040-6090(00)00890-7 (2000).
111 Puurunen, R. L. *et al.* Island growth in the atomic layer deposition of zirconium oxide and aluminum oxide on hydrogen-terminated silicon: Growth mode modeling and transmission electron microscopy. *J Appl Phys* **96**, 4878-4889, doi:Doi 10.1063/1.1787624 (2004).
112 Sneh, O., Clark-Phelps, R. B., Londergan, A. R., Winkler, J. & Seidel, T. E. Thin film atomic layer deposition equipment for semiconductor processing. *Thin Solid Films* **402**, 248-261, doi:Doi 10.1016/S0040-6090(01)01678-9 (2002).
113 Yun, S. J., Lee, K. H., Skarp, J., Kim, H. R. & Nam, K. S. Dependence of atomic layer-deposited Al2O3 films characteristics on growth temperature and Al precursors of Al(CH3)(3) and AlCl3. *J Vac Sci Technol A* **15**, 2993-2997, doi:Doi 10.1116/1.580895 (1997).
114 Nishizawa, J., Abe, H. & Kurabayashi, T. Molecular Layer Epitaxy. *Journal of the Electrochemical Society* **132**, 1197-1200, doi:Doi 10.1149/1.2114058 (1985).
115 Sneh, O., Wise, M. L., Ott, A. W., Okada, L. A. & George, S. M. Atomic Layer Growth of Sio2 on Si(100) Using Sicl4 and H2o in a Binary Reaction Sequence. *Surface Science* **334**, 135-152 (1995).
116 Skarp, J. I., Soininen, P. J. & Soininen, P. T. ALE-reactor for large area depositions. *Applied Surface Science* **112**, 251-254, doi:Doi 10.1016/S0169-4332(96)01000-8 (1997).
117 Robertson, J. High dielectric constant oxides. *Eur Phys J-Appl Phys* **28**, 265-291, doi:DOI 10.1051/epjap:2004206 (2004).
118 Kong, J. *et al.* Nanotube molecular wires as chemical sensors. *Science* **287**, 622-625, doi:DOI 10.1126/science.287.5453.622 (2000).
119 Martel, R., Schmidt, T., Shea, H. R., Hertel, T. & Avouris, P. Single- and multi-wall carbon nanotube field-effect transistors. *Appl Phys Lett* **73**, 2447-2449, doi:Doi 10.1063/1.122477 (1998).
120 Garces, N. Y. *et al.* Epitaxial graphene surface preparation for atomic layer deposition of Al2O3. *J Appl Phys* **109**, doi:Doi 10.1063/1.3596761 (2011).
121 Ng, H. T. *et al.* Single crystal nanowire vertical surround-gate field-effect transistor. *Nano Lett* **4**, 1247-1252, doi:Doi 10.1021/Nl049461z (2004).
122 Peng, H. B. & Golovchenko, J. A. Coulomb blockade in suspended Si3N4-coated single-walledcarbon nanotubes. *Appl Phys Lett* **84**, 5428-5430, doi:doi:http://dx.doi.org/10.1063/1.1765733 (2004).
123 Deheer, W. A., Chatelain, A. & Ugarte, D. A Carbon Nanotube Field-Emission Electron Source. *Science* **270**, 1179-1180, doi:DOI 10.1126/science.270.5239.1179 (1995).
124 Dai, H. J., Hafner, J. H., Rinzler, A. G., Colbert, D. T. & Smalley, R. E. Nanotubes as nanoprobes in scanning probe microscopy. *Nature* **384**, 147-150, doi:Doi 10.1038/384147a0 (1996).

125 Cavanagh, A. S., Wilson, C. A., Weimer, A. W. & George, S. M. Atomic layer deposition on gram quantities of multi-walled carbon nanotubes. *Nanotechnology* **20**, doi:Doi 10.1088/0957-4484/20/25/255602 (2009).
126 Farmer, D. B. & Gordon, R. G. ALD of high-kappa dielectrics on suspended functionalized SWNTs. *Electrochem Solid St* **8**, G89-G91, doi:Doi 10.1149/1.1862474 (2005).
127 Xuan, Y. *et al.* Atomic-layer-deposited nanostructures for graphene-based nanoelectronics. *Appl Phys Lett* **92** (2008).
128 Fallahazad, B., Kim, S., Colombo, L. & Tutuc, E. Dielectric thickness dependence of carrier mobility in graphene with HfO2 top dielectric. *Appl Phys Lett* **97**, doi:Doi 10.1063/1.3492843 (2010).
129 Farmer, D. B. *et al.* Utilization of a Buffered Dielectric to Achieve High Field-Effect Carrier Mobility in Graphene Transistors. *Nano Lett* **9**, 4474-4478, doi:Doi 10.1021/Nl902788u (2009).
130 Kim, S. *et al.* Realization of a high mobility dual-gated graphene field-effect transistor with Al2O3 dielectric. *Appl Phys Lett* **94**, doi:Doi 10.1063/1.3077021 (2009).
131 Meric, I. *et al.* Channel Length Scaling in Graphene Field-Effect Transistors Studied with Pulsed Current-Voltage Measurements. *Nano Lett* **11**, 1093-1097, doi:Doi 10.1021/Nl103993z (2011).
132 Pirkle, A., Wallace, R. M. & Colombo, L. In situ studies of Al2O3 and HfO2 dielectrics on graphite. *Appl Phys Lett* **95**, doi:Doi 10.1063/1.3238560 (2009).
133 Robinson, J. A. *et al.* Epitaxial Graphene Materials Integration: Effects of Dielectric Overlayers on Structural and Electronic Properties. *Acs Nano* **4**, 2667-2672, doi:Doi 10.1021/Nn1003138 (2010).
134 Wang, X. R., Tabakman, S. M. & Dai, H. J. Atomic layer deposition of metal oxides on pristine and functionalized graphene. *J Am Chem Soc* **130**, 8152-+, doi:Doi 10.1021/Ja8023059 (2008).
135 Yamaguchi, T., Masubuchi, S., Iguchi, K., Moriya, R. & Machida, T. Tunnel spin injection into graphene using Al2O3 barrier grown by atomic layer deposition on functionalized graphene surface. *J Magn Magn Mater* **324**, 849-852, doi:DOI 10.1016/j.jmmm.2011.09.031 (2012).
136 Lee, B. K. *et al.* Conformal Al2O3 dielectric layer deposited by atomic layer deposition for graphene-based nanoelectronics. *Appl Phys Lett* **92**, doi:Doi 10.1063/1.2928228 (2008).
137 Shin, Y. J. *et al.* Surface-Energy Engineering of Graphene. *Langmuir* **26**, 3798-3802, doi:Doi 10.1021/La100231u (2010).
138 Dlubak, B., Kidambi, P. R., Weatherup, R. S., Hofmann, S. & Robertson, J. Substrate-assisted nucleation of ultra-thin dielectric layers on graphene by atomic layer deposition. *Appl Phys Lett* **100**, doi:Doi 10.1063/1.4707376 (2012).
139 Farmer, D. B. & Gordon, R. G. Atomic layer deposition on suspended single-walled carbon nanotubes via gas-phase noncovalent functionalization. *Nano Lett* **6**, 699-703, doi:Doi 10.1021/Nl052453d (2006).
140 Williams, J. R., DiCarlo, L. & Marcus, C. M. Quantum hall effect in a gate-controlled p-n junction of graphene. *Science* **317**, 638-641, doi:DOI 10.1126/science.1144657 (2007).
141 Miller, D. C. *et al.* Thermo-mechanical properties of alumina films created using the atomic layer deposition technique. *Sensors and Actuators a-Physical* **164**, 58-67 (2010).
142 Small, M. K. & Nix, W. D. Analysis of the Accuracy of the Bulge Test in Determining the Mechanical-Properties of Thin-Films. *J Mater Res* **7**, 1553-1563, doi:Doi 10.1557/Jmr.1992.1553 (1992).
143 Tripp, M. K. *et al.* The mechanical properties of atomic layer deposited alumina for use in micro- and nano-electromechanical systems. *Sensor Actuat a-Phys* **130**, 419-429, doi:DOI 10.1016/j.sna.2006.01.029 (2006).
144 Cleland, A. N. *Foundations of Nanomechanics*. (Springer, 2003).
145 Ilic, B., Krylov, S. & Craighead, H. G. Young's modulus and density measurements of thin atomic layer deposited films using resonant nanomechanics. *Journal of Applied Physics* **108** (2010).

146 Ahn, J. Y., Chung, W. J., Pinnau, I. & Guiver, M. D. Poly sulfone/silica nanoparticle mixed-matrix membranes for gas separation. *J Membrane Sci* **314**, 123-133, doi:DOI 10.1016/j.memsci.2008.01.031 (2008).

147 de Vos, R. M. & Verweij, H. High-selectivity, high-flux silica membranes for gas separation. *Science* **279**, 1710-1711, doi:DOI 10.1126/science.279.5357.1710 (1998).

148 Fuertes, A. B. & Centeno, T. A. Carbon molecular sieve membranes from polyetherimide. *Micropor Mesopor Mat* **26**, 23-26, doi:Doi 10.1016/S1387-1811(98)00204-2 (1998).

149 Jiang, L. Y., Chung, T. S., Cao, C., Huang, Z. & Kulprathipanja, S. Fundamental understanding of nano-sized zeolite distribution in the formation of the mixed matrix single- and dual-layer asymmetric hollow fiber membranes. *J Membrane Sci* **252**, 89-100, doi:DOI 10.1016/j.memsci.2004.12.004 (2005).

150 Kim, Y. K., Park, H. B. & Lee, Y. M. Carbon molecular sieve membranes derived from thermally labile polymer containing blend polymers and their gas separation properties. *J Membrane Sci* **243**, 9-17, doi:DOI 10.1016/j.memsci.2004.05.001 (2004).

151 Lai, Z. P. *et al.* Microstructural optimization of a zeolite membrane for organic vapor separation. *Science* **300**, 456-460, doi:DOI 10.1126/science.1082169 (2003).

152 Liu, S. M. & Gavalas, G. R. Oxygen selective ceramic hollow fiber membranes. *J Membrane Sci* **246**, 103-108, doi:DOI 10.1016/j.memsci.2004.09.028 (2005).

153 Park, H. B. *et al.* Polymers with cavities tuned for fast selective transport of small molecules and ions. *Science* **318**, 254-258, doi:DOI 10.1126/science.1146744 (2007).

154 Shiflett, M. B. & Foley, H. C. Ultrasonic deposition of high-selectivity nanoporous carbon membranes. *Science* **285**, 1902-1905, doi:DOI 10.1126/science.285.5435.1902 (1999).

155 Strathmann, H. Membrane separation processes: Current relevance and future opportunities. *Aiche J* **47**, 1077-1087, doi:DOI 10.1002/aic.690470514 (2001).

156 Hinds, B. J. *et al.* Aligned multiwalled carbon nanotube membranes. *Science* **303**, 62-65, doi:DOI 10.1126/science.1092048 (2004).

157 Boutilier, M. S. H. *et al.* Implications of Permeation through Intrinsic Defects in Graphene on the Design of Defect-Tolerant Membranes for Gas Separation. *Acs Nano* **8**, 841-849, doi:10.1021/nn405537u (2014).

158 Joshi, R. K. *et al.* Precise and ultrafast molecular sieving through graphene oxide membranes. *arXiv:1401.3134* (2014).

159 Kim, H. W. *et al.* Selective Gas Transport Through Few-Layered Graphene and Graphene Oxide Membranes. *Science* **342**, 91-95, doi:DOI 10.1126/science.1236098 (2013).

160 Li, H. *et al.* Ultrathin, Molecular-Sieving Graphene Oxide Membranes for Selective Hydrogen Separation. *Science* **342**, 95-98, doi:DOI 10.1126/science.1236686 (2013).

161 Liu, H., Dai, S. & Jiang, D.-e. Insights into CO2/N2 separation through nanoporous graphene from molecular dynamics. *Nanoscale* **5**, 9984-9987, doi:10.1039/c3nr02852f (2013).

162 Mehio, N., Dai, S. & Jiang, D.-e. Quantum Mechanical Basis for Kinetic Diameters of Small Gaseous Molecules. *The Journal of Physical Chemistry A*, doi:10.1021/jp412588f (2014).

163 Shan, M. *et al.* Influence of chemical functionalization on the CO2/N2 separation performance of porous graphene membranes. *Nanoscale* **4**, 5477-5482, doi:10.1039/c2nr31402a (2012).

164 Nair, R. R., Wu, H. A., Jayaram, P. N., Grigorieva, I. V. & Geim, A. K. Unimpeded Permeation of Water Through Helium-Leak-Tight Graphene-Based Membranes. *Science* **335**, 442-444, doi:DOI 10.1126/science.1211694 (2012).

165 Wang, L. D. *et al.* Ultrathin Oxide Films by Atomic Layer Deposition on Graphene. *Nano Letters* **12**, 3706-3710, doi:Doi 10.1021/Nl3014956 (2012).

166 Jin, H., Heller, D. A., Kim, J. H. & Strano, M. S. Stochastic Analysis of Stepwise Fluorescence Quenching Reactions on Single-Walled Carbon Nanotubes: Single Molecule Sensors. *Nano Lett* **8**, 4299-4304, doi:Doi 10.1021/Nl802010z (2008).
167 McKinney, S. A., Joo, C. & Ha, T. Analysis of single-molecule FRET trajectories using hidden Markov modeling. *Biophys J* **91**, 1941-1951 (2006).
168 Cembran, A., Bernardi, F., Garavelli, M., Gagliardi, L. & Orlandi, G. On the Mechanism of the cis−trans Isomerization in the Lowest Electronic States of Azobenzene: S0, S1, and T1. *J Am Chem Soc* **126**, 3234-3243, doi:10.1021/ja038327y (2004).
169 Jin, H., Heller, D. A., Kim, J.-H. & Strano, M. S. Stochastic Analysis of Stepwise Fluorescence Quenching Reactions on Single-Walled Carbon Nanotubes: Single Molecule Sensors. *Nano letters* **8**, 4299-4304, doi:10.1021/nl802010z (2008).
170 Kolasinki, K. W. *Surface Science: Foundations of Catalysis and Nanoscience*. (Wiley, 2008).
171 Steele, W. A. *The Interaction of Gases with Solid Surfaces*. (Pergamon Press, 1974).
172 Reid, R. C., Prausnitz, J. M. & Poling, B. E. *The Properties of Gases and Liquids*. (McGraw-Hill, 1987).
173 Dean, C. R. *et al.* Boron nitride substrates for high-quality graphene electronics. *Nat Nano* **5**, 722-726 (2010).
174 Huang, P. Y. *et al.* Direct Imaging of a Two-Dimensional Silica Glass on Graphene. *Nano Letters* **12**, 1081-1086 (2012).
175 Jen, S. H., Bertrand, J. A. & George, S. M. Critical tensile and compressive strains for cracking of Al(2)O(3) films grown by atomic layer deposition. *Journal of Applied Physics* **109** (2011).
176 Rogers, J. A., Lagally, M. G. & Nuzzo, R. G. Synthesis, assembly and applications of semiconductor nanomembranes. *Nature* **477**, 45-53 (2011).
177 Suk, J. W., Murali, S., An, J. & Ruoff, R. S. Mechanical measurements of ultra-thin amorphous carbon membranes using scanning atomic force microscopy. *Carbon* **50**, 2220-2225 (2012).
178 Zhan, Y., Liu, Z., Najmaei, S., Ajayan, P. M. & Lou, J. Large-Area Vapor-Phase Growth and Characterization of MoS2 Atomic Layers on a SiO2 Substrate. *Small* **8**, 966-971.
179 Leskela, M. & Ritala, M. Atomic layer deposition (ALD): from precursors to thin film structures. *Thin Solid Films* **409**, 138-146 (2002).
180 Leskela, M. & Ritala, M. Atomic layer deposition chemistry: Recent developments and future challenges. *Angewandte Chemie-International Edition* **42**, 5548-5554 (2003).
181 Dillon, A. C., Ott, A. W., Way, J. D. & George, S. M. Surface-Chemistry of Al2O3 Deposition Using Al(Ch3)(3) and H2O in a Binary Reaction Sequence. *Surface Science* **322**, 230-242 (1995).
182 Hencky, H. Uber den spannungszustand in kreisrunden platten mit verschwindender biegungssteiflgkeit. *Zeitschrift fur Mathematik und Physik* **63**, 311-317 (1915).
183 Tapily, K. *et al.* Nanoindentation investigation of HfO(2) and Al(2)O(3) films grown by atomic layer deposition. *Journal of the Electrochemical Society* **155**, H545-H551 (2008).
184 Davidson, B. D., Seghete, D., George, S. M. & Bright, V. M. ALD tungsten NEMS switches and tunneling devices. *Sensors and Actuators a-Physical* **166**, 269-276 (2011).
185 Yoneoka, S. *et al.* Electrical and Thermal Conduction in Atomic Layer Deposition Nanobridges Down to 7 nm Thickness. *Nano Letters* **12**, 683-686, doi:10.1021/nl203548w (2012).
186 Celebi, K. *et al.* Ultimate Permeation Across Atomically Thin Porous Graphene. *Science* **344**, 289-292, doi:DOI 10.1126/science.1249097 (2014).